

**Tissue- and cell-based breast cancer diagnostics  
with iSERS microscopy**

**Dissertation**

zur Erlangung des akademischen Grades eines  
Doktors der Naturwissenschaften

– Dr. rer. nat. –

vorgelegt von

Xinping Wang

geboren in Hubei, China

Fakultät für Chemie

der

Universität Duisburg-Essen

2018



Die vorliegende Arbeit wurde im Zeitraum von Dezember 2014 bis Dezember 2017 im Arbeitskreis von Prof. Dr. Sebastian Schlücker, Lehrstuhl Physikalische Chemie I, Fakultät für Chemie der Universität Duisburg-Essen, durchgeführt.

Tag der Disputation: 12.09.2018

Gutachter: Prof. Dr. Sebastian Schlücker  
Prof. Dr. Sabine Kasimir-Bauer

Vorsitzender: Prof. Dr. Oliver J. Schmitz



## **Erklärung**

Hiermit versichere ich, dass ich die vorliegende Arbeit mit dem Titel:

Tissue- and cell-based breast cancer diagnostics with iSERS microscopy

selbst verfasst und keine außer den angegebenen Hilfsmitteln und Quellen benutzt habe.

Die Arbeit wurde in dieser oder ähnlicher Form bei keiner anderen Universität eingereicht.

Essen, im Mai 2018

Xinping Wang

# Table of Contents

<b>1 INTRODUCTION .....</b>	<b>1</b>
<b>2 THEORETICAL BACKGROUND .....</b>	<b>3</b>
2.1 SURFACE-ENHANCED RAMAN SPECTROSCOPY .....	3
2.2 iSERS MICROSCOPY .....	15
<b>3 MOTIVATION AND AIMS .....</b>	<b>27</b>
<b>4 MATERIALS AND METHODS .....</b>	<b>29</b>
4.1 CHEMICALS AND MATERIALS .....	29
4.2 METAL NP SYNTHESIS AND FUNCTIONALIZATION .....	34
4.2.1 AuNS .....	34
4.2.2 Electrostatic assembly of Au/Au core-satellites .....	35
4.2.3 Bioconjugation with antibodies .....	38
4.3 TISSUE/CELL PREPARATION AND TREATMENT .....	41
4.3.1 Tissue and cell slide preparation, fixation and blocking .....	41
4.3.2 Deparaffinization of FFPE breast tissue sections .....	44
4.3.3 Antigen retrieval .....	45
4.4 IHC .....	46
4.5 IF .....	47
4.6 iSERS .....	49
4.7 INSTRUMENTATION .....	52
<b>5 RESULTS AND DISCUSSION .....</b>	<b>56</b>
5.1 ANALYSIS OF HER2 EXPRESSION ON NORMAL AND BREAST CANCER FFPE TISSUE ....	56
5.1.1 Motivation and background .....	56
5.1.2 Characterization of SERS-active AuNS and antibody conjugates .....	58
5.1.3 IHC and IF .....	61
5.1.4 PIER and HIER .....	63
5.1.5 IF and iSERS microscopy .....	65
5.1.6 Negative control .....	67
5.1.7 Long-term iSERS study .....	69
5.1.8 Conclusions and outlook .....	70

5.2	iSERS MICROSCOPY OF SINGLE HER2-POSITIVE BREAST CANCER CELLS .....	73
5.2.1	Motivation and background .....	73
5.2.2	Optimization of the cell number on the slide .....	74
5.2.3	IF and iSERS on single breast cancer cells .....	75
5.2.4	Reproducibility of iSERS microscopy on single cells .....	77
5.2.5	Conclusions and outlook .....	84
5.3	MULTI-COLOUR iSERS MICROSCOPY ON SINGLE BREAST CANCER CELLS .....	86
5.3.1	Motivation and background .....	86
5.3.2	Characterization of SERS-labelled antibodies .....	87
5.3.3	Single-colour iSERS imaging .....	101
5.3.4	Negative control experiments .....	103
5.3.5	Multi-colour iSERS imaging.....	105
5.3.6	Conclusions and outlook .....	107
5.4	IDENTIFICATION OF SINGLE BREAST CANCER CELLS AMONG CELL MIXTURE .....	110
5.4.1	Motivation and background .....	110
5.4.2	IF staining.....	112
5.4.3	SERS intensity characterization.....	114
5.4.4	Single-colour iSERS imaging of HER2, EGFR and CD45 .....	115
5.4.5	Multi-colour iSERS imaging.....	118
5.4.6	Conclusions and outlook .....	124
<b>6</b>	<b>SUMMARY .....</b>	<b>127</b>
<b>7</b>	<b>ZUSAMMENFASSUNG .....</b>	<b>129</b>
<b>8</b>	<b>REFERENCES.....</b>	<b>131</b>
<b>9</b>	<b>APPENDIX.....</b>	<b>146</b>

## 1 Introduction

Life expectancy has been extended by overcoming various of toughing miscellaneous diseases as a result of the rapid development of technologies. Even though, cancer is still the remaining problem which is difficult to handle due to multifactorial causes as well as the neoplastic mutation and transformation. Therefore, cancer diagnosis plays pivotal role in medical treatments for patients.

Generally, cancer screening involves blood and urine tests, genetic, ultrasound tests and imaging of visceral organs by proton nuclear magnetic resonance or computed tomography. Traditional diagnostic methods often require the complex instrumentation, long-time interpretation and lack the sufficient sensitivity. Thus, novel detection strategies are still urgently needed to conquer these drawbacks.

In recent years, substantial endeavour has been exploited to devise new methods for the cancer diagnosis covering various subjects ranging from biology, electrochemistry, physical chemistry and material science (Feng et al., 2011; Sha et al., 2008; Thakur et al., 2014; Wang et al., 2014a; Wu et al., 2003). Specifically, many of these studies were mainly focused on the detection of certain biomarkers which are symbols of the cancer generation (Hori and Gambhir, 2011; Laxman et al., 2008; Mitchell et al., 2008; Zhang et al., 2004).

Surface-enhanced Raman scattering (SERS) as one of the newly developed techniques has shown its outstanding performance in *in-vitro/vivo* diagnostics (Qian et al., 2008a; Wang et al., 2017b; Zhang et al., 2015; Zong et al., 2016). The high sensitivity (Kneipp et al., 2008) and multiplexing capability (Cheng et al., 2017; Dinish et al., 2014; Gellner et al., 2009) allow the trace and high throughput analysis overcoming some of bottlenecks of traditional analytical techniques. Immuno-SERS (iSERS) microscopy

## INTRODUCTION

---

with the combination of SERS microscopy and the immuno activity of antibodies can target and image the antigen expression level on tissue sections (Lutz et al., 2008; Salehi et al., 2014; Schlücker et al., 2006) and cell slides (Lee et al., 2012; Wang et al., 2014a) for imaging-guided cancer treatments.

In this section, the theoretical part of Raman effect will be firstly introduced. Since metallic nanoparticles (NPs) are the original amplifier of Raman signal, a basic overview of various types of NPs applied in former studies will be presented. Then, the encapsulation of synthesized NPs with a layer of silica/BSA/polymer to obtain the stability and biocompatibility will be discussed. Moreover, different conjugation methods of antibodies onto NPs will be summarized in the last part.

## 2 Theoretical background

### 2.1 Surface-enhanced Raman spectroscopy

In 1930, Nobel prize of physics was awarded to Chandrasekhara Venkata Raman for his discovery of Raman effect in 1928 (Raman and Krishnan, 1928). In 1923, Adolf Smekal predicted the theoretical part of the phenomenon of Raman effect. However, until 1928 Raman and his coworkers have observed that the frequency of the incident light was changed when it passed through the liquid, known as Raman effect or Raman scattering. Since then, Raman spectroscopy, a measurement of the resulting signal from Raman effect has been applied in various fields (Alvarez-Puebla and Liz-Marzan, 2012; Li et al., 2011; Lin et al., 2013; Zhou et al., 2014).

When an electromagnetic (EM) wave (light) is irradiated onto a molecule, a change of the wavelength of the incident light can be observed due to a vibrational transition of the molecule which is called Raman effect shown in **Figure 2.1**. The quantum description of the Raman effect is when an incident photon with energy  $h\nu_0$  ( $\nu_0$  is the frequency of the incident light) excites a molecule situated in a certain vibrational state to a higher or lower vibrational level, emitting a photon with energy  $h\nu_0 \pm h\nu_v$ .

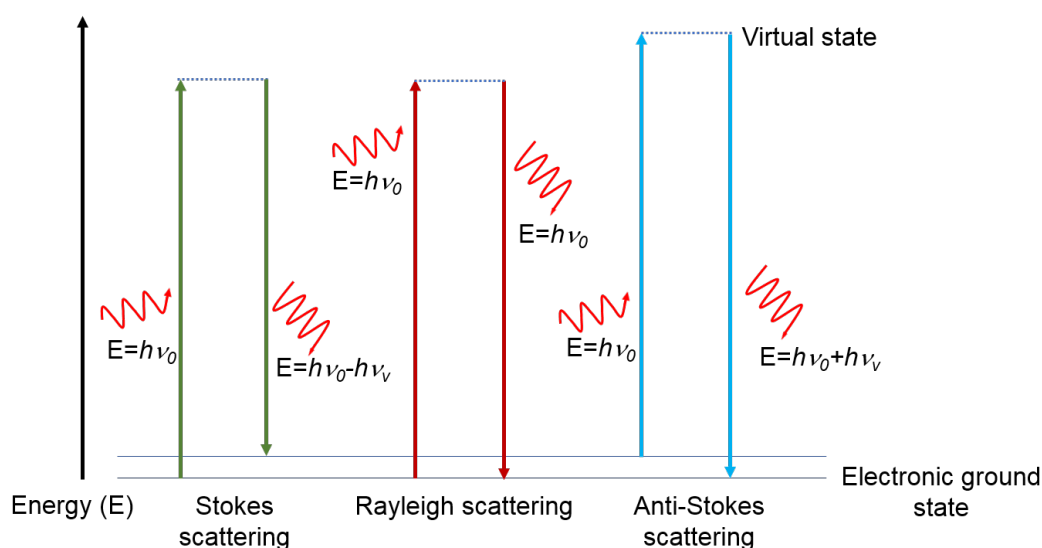


**Figure 2.1 | Illustration of Raman scattering by Jablonski diagram.**

## THEORETICAL BACKGROUND

---

Scattering of the light can be further classified into two parts which are elastic scattering and inelastic scattering. A molecule located in the ground state is excited to a virtual state by an incident photon. When it returns to the original state, a photon with the same energy as the incident photon is scattered. This process is called elastic scattering, also known as Rayleigh scattering. The scattered photon is irradiated statistically in all directions in space. This happens when the radius of a molecule is much smaller than the wavelength of the incident light. The intensity  $I$  of the scattered light could be defined as follows.

$$I = I_0 \frac{1 + \cos^2 \theta}{2R^2} \left(\frac{2\pi}{\lambda}\right)^4 \left(\frac{n^2 - 1}{n^2 + 2}\right)^2 \left(\frac{d}{2}\right)^6 \quad (2.1)$$

Herein,  $I_0$  is the intensity of the incident light,  $\lambda$  is the wavelength of the incident light,  $\theta$  is the scattering angle,  $n$  is the refractive index of the particle,  $d$  is the radius of the scattering sphere and  $R$  is the distance between the detecting point and the scattered sphere. Since Rayleigh scattering is a wavelength-dependent phenomenon and inversely proportional to the fourth power of the wavelength of the incident light, the sky is rendered as blue and turns red during the sunrise and sunset.

The emitted inelastic scattered light quantum is with a lower or higher energy compared to the incident light. Here, the scattered energy is  $h\nu_s$  ( $\nu_s$  is the frequency of the scattered light) which is the incident photon energy plus or minus also called vibrational energy. The difference between the incident light and the inelastic scattered light is called Raman shift and can be monitored in the Raman spectrum.

As depicted in **Figure 2.1**, the inelastic scattering can be further divided into Stokes scattering and anti-Stokes scattering. Stokes scattering happens when a molecule in the ground state is excited to a virtual state by an incident photon and a scattered photon is radiated with less energy compared to the incident photon. In comparison, if a molecule in the first excited state goes back to the ground state, one observes anti-Stokes

## THEORETICAL BACKGROUND

---

scattering. The interaction between the molecule and the incident photon gives rise to the scattered photon with a higher energy obtained from the molecule.

Given the Boltzmann distribution, vibrational ground states of molecules are largely occupied at room temperature (RT). Thus, Stokes scattering is more efficient than anti-Stokes scattering. Furthermore, Raman activity of a molecule is depending on its polarizability. When a molecule is exposed to an external electric field, electrons and nuclei with different charges are forced to move in various directions resulting in a dipole moment. The induced dipole moment is in proportion to the molecular polarizability.

The selection rule of Raman scattering is generalized as the change of the polarizability for a molecule while crossing the equilibrium point. Only Rayleigh scattering happens when the polarizability of atoms is isotropic radiating with the same frequency of the incident light. Raman scattering can be obtained when the polarizability of molecules is anisotropic depending on the vibrational and rotational coordinates.

Raman spectroscopy has shown the irreplaceable status as an analytical vibrational tool for solid, liquid, gas and compounds (Katayanagi et al., 2004; Keiner et al., 2014; Li et al., 2014). However, the extremely low occurrence rate of Raman scattering i.e.  $10^{-6}$  to  $10^{-8}$  for an incident photon has limited its further applications. In 1974, Fleischmann et al. reported the Raman intensity of pyridine was enhanced when it was adsorbed on a roughened silver electrode (Fleischmann et al., 1974). Jeanmaire et al. in 1977 also observed the intensified Raman signal of pyridine and other amines adsorbed on a silver electrode in a thorough electrochemical study and attributed this phenomenon to a certain surface-enhanced effect on metallic interfaces (Jeanmaire and Vanduyne, 1977). Nowadays, this effect is well known and termed as SERS. In comparison with conventional Raman spectroscopy, the enhancement factor of SERS can be up to ca.

$10^{11}$ . In addition, SERS is also found on the surface of other metals such as gold and copper.

As shown in former studies, a metallic surface is an essential element when probing the enhanced Raman signal (Lee and Meisel, 1982, Ko et al., 2008). Initial SERS studies were carried out on roughened metal surfaces. Later, given the massive explorations on nano-sized particles, nanotechnology was extensively applied in SERS for enhancing the Raman signal. The large surface to volume ratio and unique optical properties of noble metal NPs have enabled them superior to the planar metal surface as substrates for the enhancement of Raman signal. Early in the fourth century NPs have been employed in paintings and glassware. **Figure 2.2** shows an example of the well-known Lycurgus cup (Barber and Freestone, 1990) using the optical property of gold nanoparticles (AuNPs) to exhibit the vivid colour.

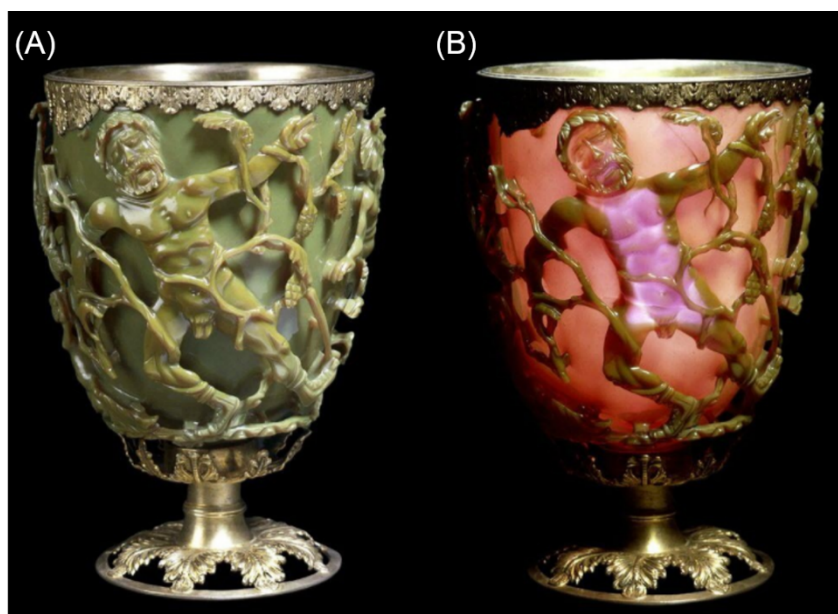


**Figure 2.2** | Pictures recorded from Lycurgus cup exhibited as different colours when illuminating externally (A) or internally (B). This figure originates from © Trustees of the British Museum with adaptations.

To fully understand the principle of NPs-based SERS, it is essential to know the concept of surface plasmon resonance (SPR) and localized surface plasmon resonance (LSPR).

## THEORETICAL BACKGROUND

---

In 1902 Wood initially observed the phenomenon of SPR through the notice of unequally distributed light bands existed in the reflected light after shining the polarized light onto a mirror (Wood, 1902). The theoretical concept was then defined by Lord Rayleigh in 1907 (Rayleigh, 1907). Pines and Bohm in 1952 attributed an energy loss to the excitation of free electrons in the metal inducing plasma oscillations when fast electrons transmitted through the metallic surface (Pines and Bohm, 1952). This excitation is termed as plasmon. Later in 1957 Ritchie formally introduced the expression of surface plasmon to explain the energy loss found by Pines and Bohm (Ritchie, 1957).

Surface plasmon is defined as collective oscillations of the conduction electrons at the interface of two materials which own the positive and negative permittivity, respectively. It can be classified into a surface plasmon which is a propagating wave travelling at a planar metal surface shown in **Figure 2.3 (A)** and localized surface plasmon confined in the case of metal nanoparticle (NP) shown in **Figure 2.3 (B)**.

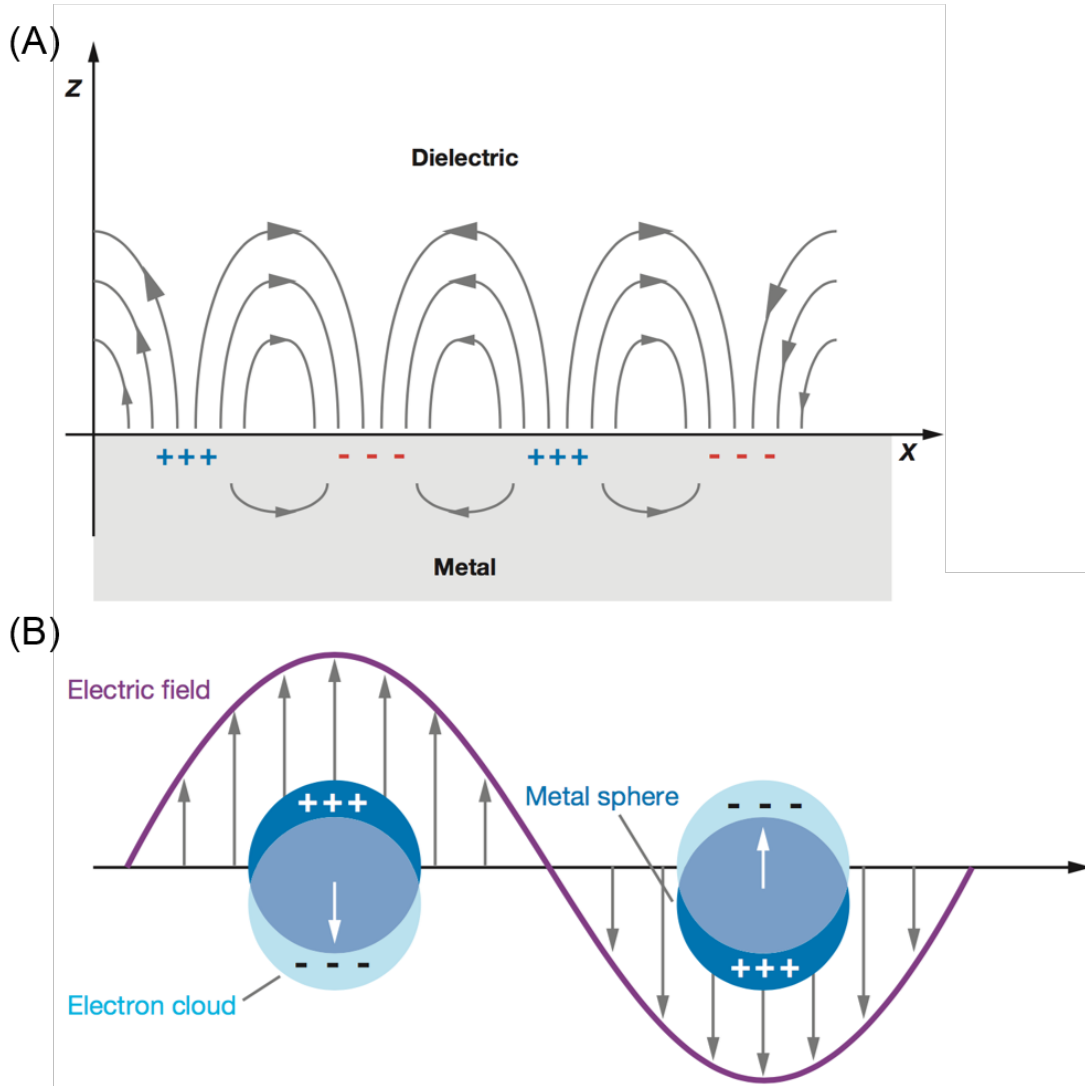


**Figure 2.3** | Schematic representation of (A) a propagating surface plasmon at the interface of a metal surface and (B) a localized surface plasmon which the oscillating electrons in the metal sphere move together with the external electric field. This figure originates from Willets and Van Duyne, 2007 with adaptations.

The LSPR excitation involves the induction of a dipole moment ( $\mu_{\text{ind}}$ ) in the metal:

$$\mu_{\text{ind}} = \alpha E_0(\omega_0) \quad (2.2)$$

The dipole moment is determined by the above equation where  $\alpha$  stands for the polarizability of the metal and  $E_0(\omega_0)$  is the incoming EM field. The scattered light oscillates with the same frequency as the frequency of the induced dipolar oscillation.

Generally,  $\alpha$  depends on the type, size and morphology of metals. The above-

## THEORETICAL BACKGROUND

mentioned surface plasmon, SPR along with LSPR constitute the theoretical basis of the mechanism of SERS. Two main contributing factors for Raman enhancement of molecules adsorbed on or in adjacent to the metal surface are EM enhancement and chemical enhancement (CE). EM enhancement accounts for the major percentage in the overall enhancement of Raman signal which was found by Otto et al. in 1992 (Otto et al., 1992) and Weitz et al. in 1982 (Weitz et al., 1982). CE refers to the chemical transfer mechanism which has been demonstrated experimentally by Campion et al. in 1995 contributing an enhancement of  $10^2$  to Raman intensity (Campion et al., 1995).

As shown in **Figure 2.4**, when the incident light excites metal NPs, the electric field is accumulated around NPs by the localized surface plasmon and consequently induces the dipole moment of the metal leading to the magnified EM field of the incident light as well as the localized EM field in the vicinity of the metal surface (hotspot). The interaction between the enhanced EM field of the incident light and the dipolar field of NPs leads to the amplified Raman signal of molecules located close to the metallic surface.

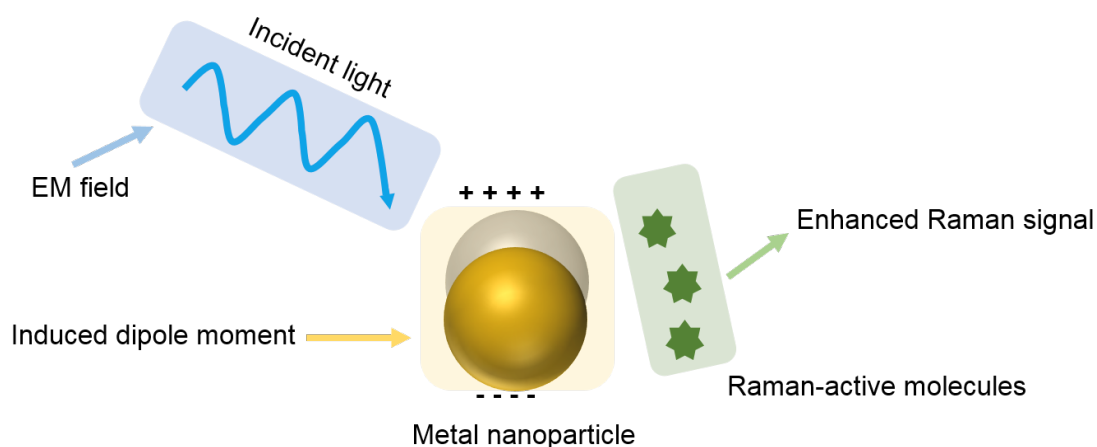


**Figure 2.4 | Schematic illustration of the mechanism of EM enhancement.**

The fourth power law (Gersten and Nitzan, 1980, Schatz and Van Duyne, 2002) can be applied for the explanation of EM enhancement factor  $G_{\text{SERS}}$ .

## THEORETICAL BACKGROUND

---

$$G_{\text{SERS}} = \left| \frac{E_{\text{loc}}}{E_0} \right|^4 = \left| \frac{\varepsilon_m - \varepsilon_s}{\varepsilon_m + 2\varepsilon_s} \right|^4 \left( \frac{R}{R+d} \right)^{12} \quad (2.3)$$

From the expression, EM enhancement factor is in direct proportion to the fourth power of the local electric field  $E_{\text{loc}}$  relative to the incident field  $E_0$ .  $\varepsilon_m$  and  $\varepsilon_s$  are the dielectric constants of NPs and external medium, respectively. The distance between the adsorbed molecule and the surface of metallic NPs is denominated as  $d$  in this equation and  $R$  is the radius of NPs. Note that if the denominator approaches to zero and  $G_{\text{SERS}}$  will be maximized where  $\varepsilon_m$  equals to  $-2\varepsilon_s$ . Then intense enhancement factor could also be generated when adsorbed molecules are close to or on the surface of NPs. The increased size of NPs will lead to an increase of EM enhancement factor. In addition,  $\left| \frac{\varepsilon_m - \varepsilon_s}{\varepsilon_m + 2\varepsilon_s} \right|$  is described as the non-dimensional polarizability of metallic NPs.

Another contributing factor in SERS enhancement is generally accepted as chemical enhancement first proposed by Albrecht and Creighton in 1977 (Albrecht and Creighton, 1977). However, the detailed mechanism is still in dispute. A generally accepted statement is the coupled charge-transfer reaction between electrons from the adsorbed molecule and the metal nanostructure. The polarizability of the molecule is hence changed causing the resonance Raman scattering and the intensified Raman signal is then generated. Generally, CE is comparatively much weaker than EM enhancement.

Given induced effects of CE and EM enhancements, the power of the Stokes signal in SERS ( $p^{\text{SERS}}(\nu_S)$ ) could be described as:

$$p^{\text{SERS}}(\nu_S) = N\sigma_{\text{ads}}^R |A(\nu_L)|^2 |A(\nu_S)|^2 I(\nu_L) \quad (2.4)$$

The above summarized equation (Kneipp et al., 2008) presents the SERS Stokes signal induced by nanostructures and gives the guidance for the design of novel SERS nanotags.  $A(\nu_S)$  and  $A(\nu_L)$  are enhancement factors of the Raman-scattered field and

## THEORETICAL BACKGROUND

---

the incident radiation, respectively.  $N$  and  $\sigma_{ads}^R$  are the number and the cross section of adsorbed molecules involved in the process of scattering, respectively.  $I(\nu_L)$  is the intensity of the excitation laser. According to the equation, the overall SERS signal can be adjusted by selectively changing the type of nanostructures, adsorbed molecules or the intensity of the laser.

Metal NPs are of extraordinary importance in SERS-based assays. The size, morphology, composition as well as the dielectric property of NPs is directly associated with the amplified strength of the Raman signal. In the early beginning, planary roughened silver electrodes were used to enhance the SERS intensity (Fleischmann et al., 1974). After that, more efforts were attempted to develop new fabrication methods for various nanostructures to achieve higher SERS sensitivity, stability and reproducibility which can be applied in analytical chemistry, life science, catalysis and food safety test (Chen et al., 2007; Lu et al., 2004; Shanmukh et al., 2006; Wen et al., 2013).

Due to the facile synthesis, low cost and flexible modification of the surface layer, colloidal NPs have attracted enormous interests. AuNP and silver nanoparticle (AgNP) with the absorption in the visible or near infrared range shown in **Figure 2.5 (A)** and **(B)** are extensively applied substrates in applications of SERS (Dasary et al., 2009; Joo et al., 2002). Traditional synthesis of spherical and monodispersed AuNP is according to the method developed by Frens et al. in 1973 (Frens, 1973) via the reduction of  $\text{HAuCl}_4$  solution with sodium citrate. This is based on Turkevich's method (Turkevich et al., 1951). For spherical AgNPs, the Lee-Meisel method (Lee and Meisel, 1982) is employed through the reduction of silver nitrate ( $\text{AgNO}_3$ ) by sodium citrate. Recently, the seed-mediated growth strategy has been demonstrated to have the capability for synthesizing NPs with more controllable morphology and size distribution (Bastus et al., 2011; Liu et al., 2012; Ruan et al., 2014).

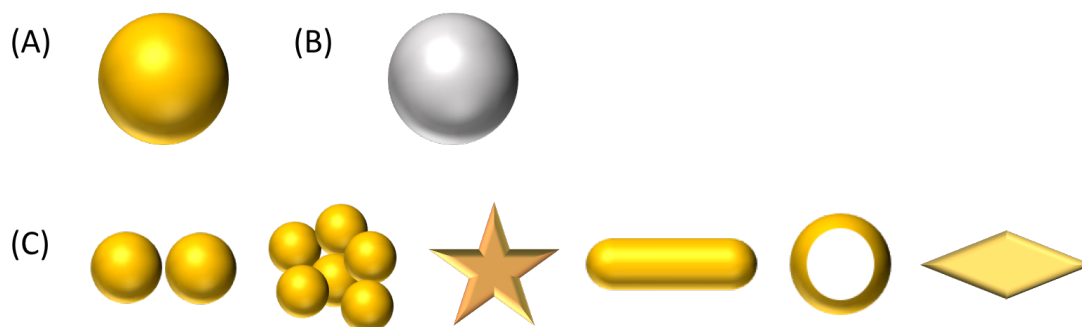


**Figure 2.5 | Schematic overview of SERS substrates composed of pure metal. (A)** Au nanosphere **(B)** Ag nanosphere **(C)** AuNPs with different morphologies: Au dimer, aggregated Au nanospheres, Au nanostar, Au nanorods, hollow gold nanospheres and gold bipyramids, respectively. (From left to right)

To meet the demand of improved SERS intensity for trace detection, a wide variety of nanostructures in terms of geometry are designed. Herein, we just take nanostructures composed of pure Au metal ions shown in **Figure 2.5 (C)** as an example.

Hot spots are the positions where higher SERS intensity is achieved. Au dimer formed by two single spherical NPs with close spacing around 1-5 nm is able to generate dramatically enhanced SERS intensity which enables the bridged Au dimer an extremely efficient SERS substrate (McMahon et al., 2009; Talley et al., 2005; Thacker et al., 2014). Another easier way to produce hotspots is the formation of Au aggregates (Schwartzberg et al., 2004) where multiple Au spherical NPs are involved as a whole for the improvement of the signal brightness. Anisotropic Au nanorods (Lohse and Murphy, 2013) with longitude and transverse plasmon frequencies can be excited in the near infra-red region, showing the great potential for *in vivo* applications. Au nanorod with strong capacity for converting the radiated photon energy to heat has shown its promising applications in nanomedicine and photo-thermal therapy (Dickerson et al., 2008; von Maltzahn et al., 2009). Au nanostars (AuNS) (Hao et al., 2007; Nehl et al., 2006) with inherent hotspots located in sharp tips are frequently treated as SERS substrates. AuNS with high sensitivity even down to a single particle are broadly

## THEORETICAL BACKGROUND

---

employed for detection of heavy metal ions/protein, drug delivery and bioimaging (Jana et al., 2015; Li et al., 2016; Ndokoye et al., 2014; Wang et al., 2014b).

Hollow gold nanospheres are internally filled with solvent and externally surrounded with a gold shell. They have been employed as SERS substrates in biosensors, photo-thermal ablation therapy and bioimaging due to the outstanding SERS enhancement via built-in pinholes and tunable plasmon resonance adsorption by changing the shell thickness (Chon et al., 2010; Lee et al., 2009; Schwartzberg et al., 2006; Zhang, 2010). Meanwhile, the emergence of numerous novel nanostructures such as bipyramids shown in **Figure 2.5 (C)** provides the versatility for the selection of SERS substrates (Zheng et al., 2012).

As shown in **Figure 2.6**, various bimetallic noble nanostructures are fabricated with different compositions and shapes. The structure of core-satellites (Ma et al., 2014; Rong et al., 2015; Zhao et al., 2017; Zheng et al., 2013) is popularly adopted as the substrate with considerable SERS signal due to the EM enhancement via the plasmonic coupling between the core and satellites such as Au/Ag core-satellites in **Figure 2.6 (A)**. A number of novel methods have been designed for the construction of such nanocomposites via electrostatic adsorption, linker molecules, deoxyribonucleic acid (DNA)-mediated hybridization and *in situ* deposition.

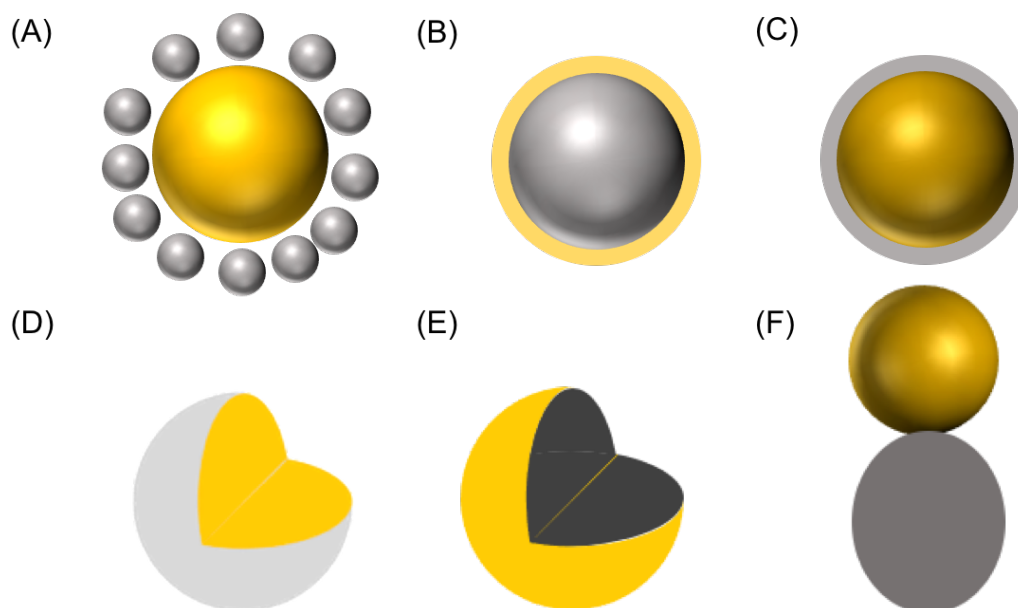


**Figure 2.6** | Schematic illustration of bimetallic SERS substrates with different configurations: (A) Au/Ag core-satellites (B) Ag core and Au shell (C) Au core and Ag shell (D) Au core and Pt shell (E) Magnetic  $\text{Fe}_3\text{O}_4$  core and Au shell (F) Au/Ag nano-snowman.

Anisotropic core-shell NPs with variable composition and shell thickness have been broadly explored due to their high SERS sensitivity. Core-shell NPs comprising silver and gold are shown in **Figure 2.6 (B)** and **(C)** (Kumar et al., 2007; Samal et al., 2013; Yang et al., 2008). **Figure 2.6 (D)** depicts nanocomposites comprised by the Au core and Pt shell showing SERS and catalytic activities (Li et al., 2006; Lu et al., 2004). Furthermore, both the inner core and the outer shell can be flexibly tuned to other materials, which offers new functionalities for NPs. For instance, as shown in **Figure 2.6 (E)**, the  $\text{Fe}_3\text{O}_4$  core gives the nanostructure magnetic property while the covered Au shell affords the enhanced SERS signal when probe molecules with Raman activity are attached on the surface (Lim et al., 2008; Yazgan et al., 2012; Zhai et al., 2009). The synthesized particles with interior  $\text{Fe}_3\text{O}_4$  core can be easily enriched and separated by applying an external magnetic field.

In addition, a number of anisotropic nanostructures with close junction have been studied to a large extent. The heterometallic nanosnowman (Lee et al., 2014) shown in **Figure 2.6 (F)** is with a Au head and Ag body with a narrow plasmonic neck which can induce higher SERS signal compared to the monometallic nanostructure. This is realized by the deposition of AgNP onto DNA-capped AuNP and the morphology of the neck is controlled by the salt concentration.

### 2.2 iSERS microscopy

iSERS combines the immuno-activity of the antibody and the noble metal NPs which contribute the enhancement of Raman signal. The fabrication processes of SERS probe are presented in **Figure 2.7**. In general, Raman reporter molecules with characteristic vibrational modes are attached on the surface of metal NPs to form the SERS tag. Subsequently, the stabilizing reagent is incubated with SERS nanotag to provide the physio-chemical stability during washing or functionalization steps. Then, the specific binding activity against the corresponding antigen is induced by modifying SERS nanotag with antibodies to form the SERS probe. Therefore, it enables the identification of a single target within a complex (Wang et al., 2017b). After the addition of the SERS probe onto the clinic samples such as tissue or cell sides, a microscopic imaging measurement is carried out on a selected region to produce the Raman image showing the distribution of the targeted protein. The pixel in the image is generally referred to the SERS intensity of a specified peak area in the spectrum of a certain Raman reporter. The method for such imaging is called iSERS microscopy.

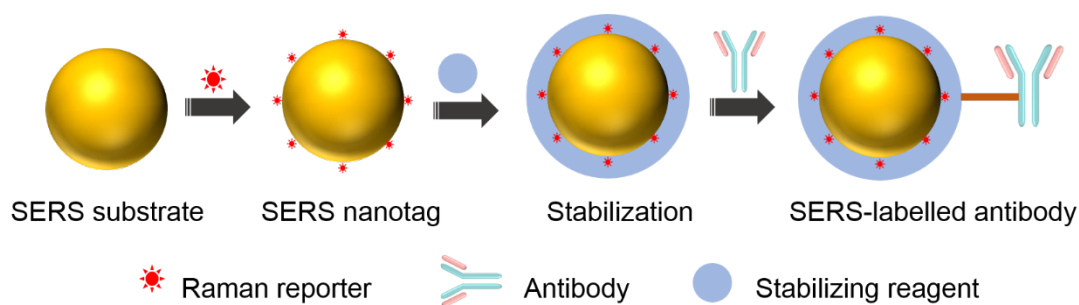


**Figure 2.7 | Synthesis route from SERS substrate to SERS-labelled antibody.**

In following sections, we will briefly introduce the basic structure of the antibody, stabilizing methods for the SERS tag and a variety of methods for antibody conjugation onto NPs.

Antibody is the class of protein produced as the immune response for the self-protection when exogenous substances called antigens attack the body. Basically, antibodies can be divided into 5 types, namely, immunoglobulin G (IgG), immunoglobulin M, A, D and E. IgG is the mostly studied antibody and constitutes predominantly 75%-80% of overall antibodies in the serum.

As shown in **Figure 2.8 (A)**, IgG consisted of two heavy chains and two light chains is folded as ‘Y’ shape. The average weight of IgG is around 150 kD with a length of 10 to 15 nm. The heavy and light chain both contain a variable region for specific recognition of the antigen and a constant region. The arm of the antibody is called Fab region while the tail region is named Fc region possessing numerous N-glycosylation sites.

**Figure 2.8 (B)** presents the structure of anti-human epidermal growth factor receptor 2 (anti-HER2) antibody determined by X-ray crystallography (Wu et al., 2013). The –SH groups of the cysteine and primary –NH<sub>2</sub> groups of lysine residues located in the side chain are highlighted. These functional groups can be utilized for the conjugation of

## THEORETICAL BACKGROUND

antibodies onto various substances such as the planar metal support or NPs (Cho et al., 2015; Ni et al., 1999).

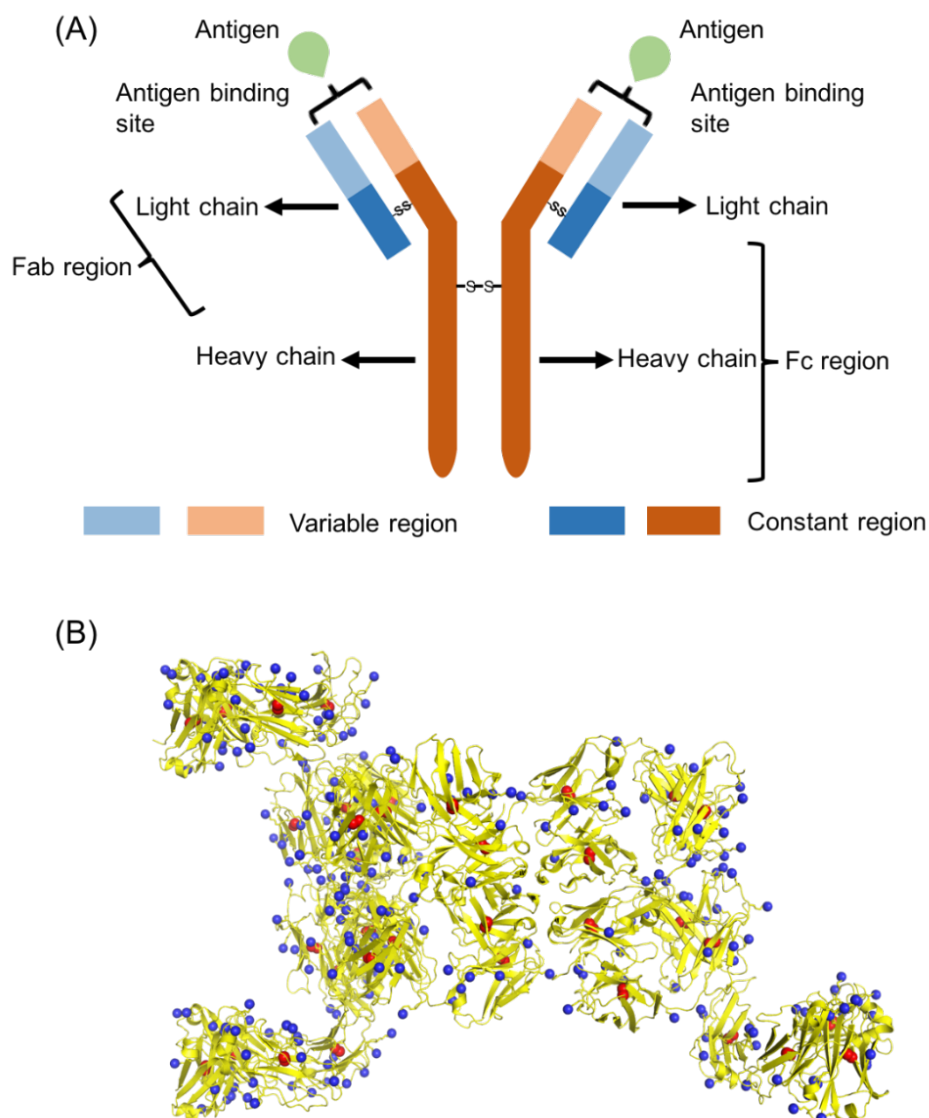


**Figure 2.8** | (A) Structure of Y shaped antibody (B) The crystal structure of IgG dimer is shown as cartoon and colored as yellow. The sulfur and nitrogen atoms of side chains of cysteine (-SH) and lysine residues (-NH<sub>2</sub>) are highlighted and shown as red and blue spheres. The structure is acquired from the protein data bank (PDB, 4NHG).

For bio-applications, it demands multiple steps for the modification of various recognition elements onto NPs or for the purpose of purification. Therefore, how to sustain the stability to prevent the aggregation of NPs or provide the biocompatibility

is crucially important for the use of labelled NPs. Among various encapsulating approaches, herein we will emphasize on the brief introduction of the following four frequently applied strategies which are presented in **Figure 2.9**.

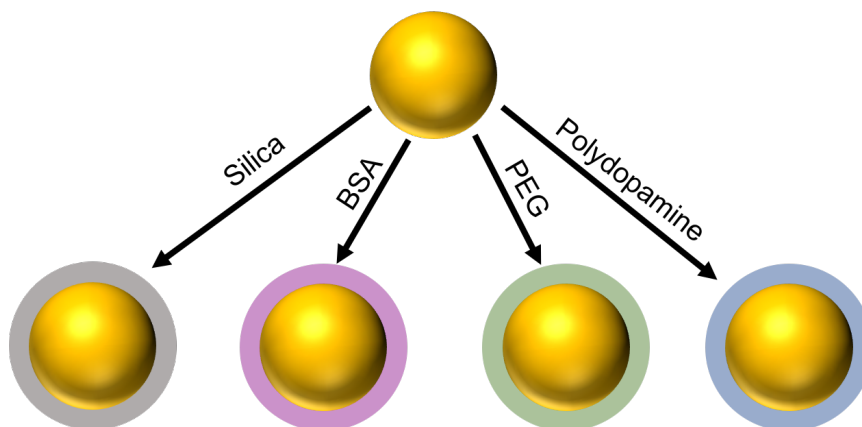


**Figure 2.9** | Four typical ways for the stabilization of metal NPs.

First, silica is a popular material to provide the mono-dispersity and various ways have been developed by forming a shell with inert chemical dielectric property around NPs, shown in **Figure 2.10**.

The encapsulation strategy for NPs with silica shown in **Figure 2.10 (A)** was obtained by first adding Raman reporters and then (3-mercaptopropyl) trimethoxysilane (MPTMS) as the silane coupling reagent (Mulvaney et al., 2003; Doering and Nie, 2003). Subsequently, sodium silicate was added to generate a condensed silica shell. SERS tags with high SERS signal and remarkable stability can be synthesized in this way by adjusting the concentration ratio of Raman reporters to the coupling reagent. In addition, our group has also reported a strategy for the synthesis of silica-encapsulated SAMs on NPs, shown in **Figure 2.10 (B)** (Küstner et al., 2009). In comparison with other reported studies, a full coverage of Raman reporters and a silica shell on NPs can be simultaneously obtained. Multiple steps were needed to obtain the silica shell through the sequential addition of poly (allylamine hydrochloride) (PAH), polyvinylpyrrolidone (PVP) and tetraethyl orthosilicate (TEOS). Later, as shown in

## THEORETICAL BACKGROUND

**Figure 2.10 (C)**, a rapid method for the construction of Au-core silica-shell particles was developed (Liu et al., 2010). Only a sol-gel procedure was required to form the silica layer around Raman reporters-labelled AuNPs via adding TEOS and ammonia. A broad spectrum of Raman reporters could be employed using this encapsulating approach.

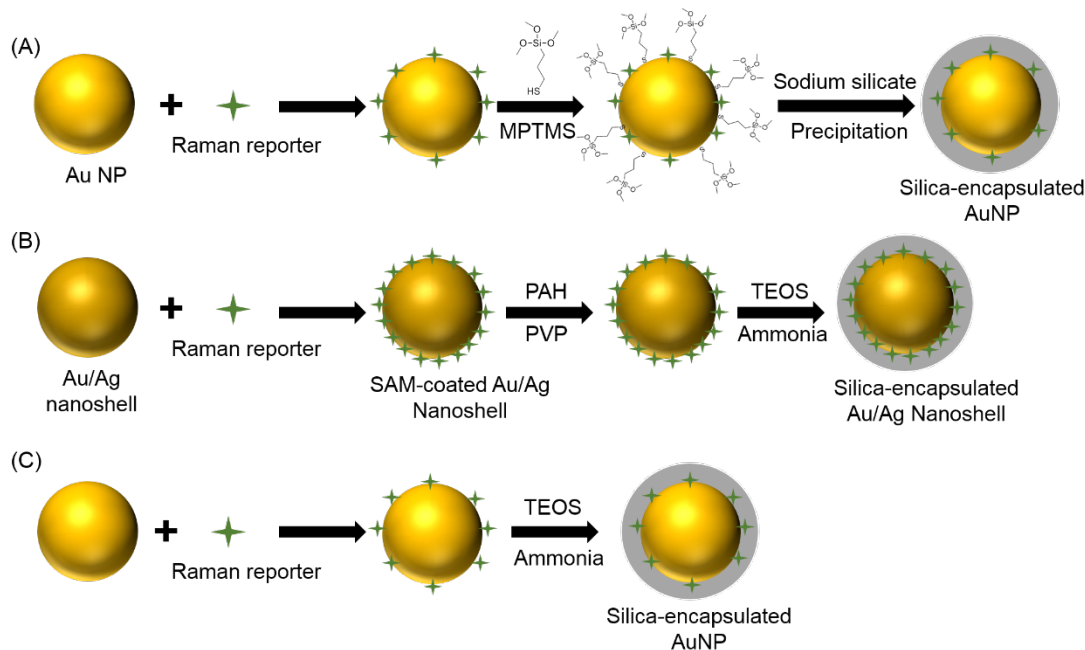


**Figure 2.10** | (A) to (C) AuNP encapsulated with silica shell in various ways. This figure originates from Wang et al., 2013 with adaptations.

Second, bovine serum albumin (BSA) with high water solubility is another type of molecule widely used for surface coating (Samanta et al., 2011; Zheng et al., 2014). The presence of a diversity of functional groups such as amine, disulfide, and carboxylate makes BSA suitable for bio-conjugation. The disulfide groups provide BSA the highly robust binding activity towards gold metallic NPs via the Au-S reaction. Besides, BSA with an average molecular weight of 60 kD formed as the protective layer around NPs can reduce the unspecific binding of other molecules due to the steric hindrance and prevent the aggregation. For intracellular studies, the cytotoxicity can be decreased to a large extent when NPs are capped with a layer of BSA.

## THEORETICAL BACKGROUND

Third, polyethylene glycol (PEG) with repeated ethylene glycol units has been used in an enormous scope of biomedical and pharmaceutical applications as a capping or coupling reagent for NPs (Chen et al., 2016; Jokerst et al., 2011; Liu et al., 2016; Qian et al., 2008a). **Figure 2.11** shows PEGylated NP and the summary of its imaging and therapeutic applications. After the modification with a PEG layer, the resulting interface between the solvent and NPs renders NPs hydrophilic and biocompatible. More importantly, via the increased steric distance, NPs with a PEG layer show reduced interaction with other proteins. In addition, the availability of hetero-PEG molecules provides various linking possibilities between NPs and molecules which are needed to be conjugated onto the surface of NPs for specific recognition.

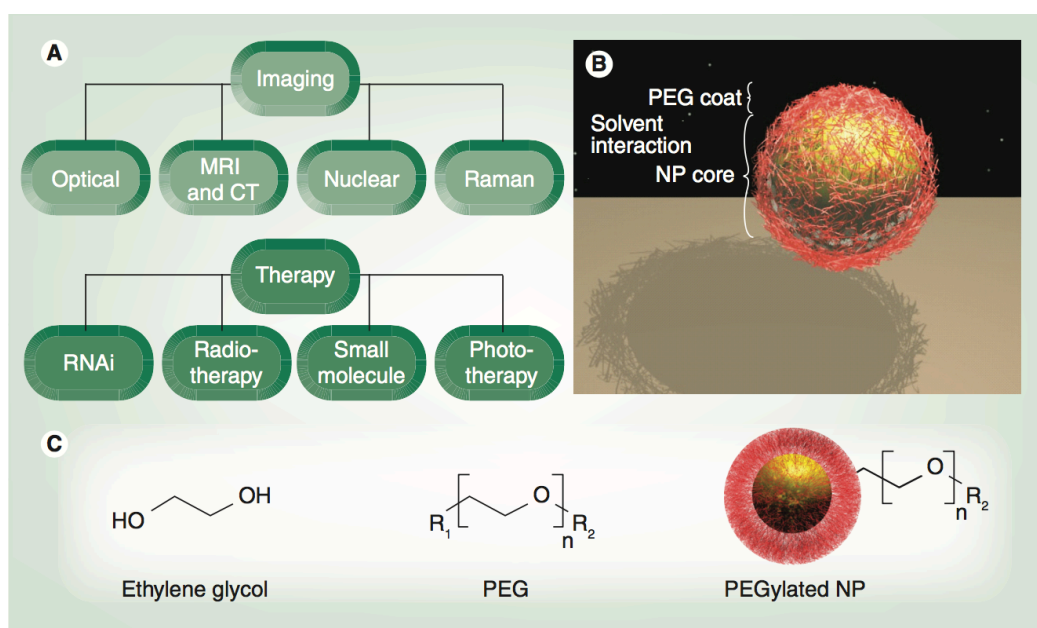


**Figure 2.11 | PEGylated NPs and their applications for imaging and therapy studies.** This figure originates from Jokerst et al., 2011.

Last, the alternative coating strategy is the utility of a mussel-inspired biopolymer called polydopamine (PDA) which is extensively employed in NPs encapsulation (Black et al., 2013; Shi et al., 2015; Zhou et al., 2016). The conformal deposition of a PDA layer for the full coverage of NPs can be achieved shortly by the self-polymerization of dopamine (**Figure 2.12**) in alkaline solution. The abundant catechol

## THEORETICAL BACKGROUND

---

and primary amine groups existed in PDA provide functional anchor sites for metal ions or other substances. Zhou et al. have successfully synthesized a novel nanostructure consisting of a Au core and multiple Au shells spaced by the formation of PDA (Zhou et al., 2016). This approach provides the flexible platform for the construction of composite metal NPs with new plasmonic or optical properties which can be broadly applied as the nano carrier for nanodiagnostics, catalysis and environmental detection.

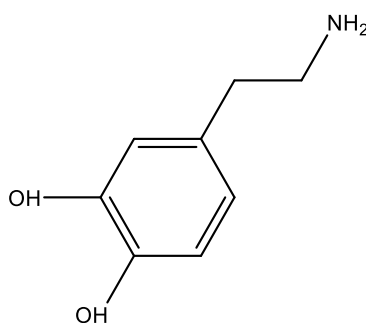


**Figure 2.12 | Chemical structure of dopamine.**

Antibody labelling is a key process to achieve the specific recognition against protein biomarkers in iSERS. A number of various protocols have been developed for antibody conjugation either by covalent or non-covalent binding. Herein, we will first focus on the summarized brief introduction for three dominating covalent labelling approaches which are involved in versatile techniques shown in **Figure 2.13**.

The most comprehensively applied immobilization method is based on the carbodiimide assisted reaction as shown in **Figure 2.13 (A)** (Cheng et al., 2017; Yang et al., 2012; Yang and Jiang, 2016). A multitude of free primary amino groups in lysine residues on the antibody can be coupled to NPs pre-functionalized with carboxylate groups. The commonly employed carbodiimide reagents are 1-ethyl-3-(3-dimethylaminopropyl) carbodiimide (EDC) along with N-hydroxysulfosuccin-imide sodium salt (sulfo-NHS) in aqueous solution for the formation of the amide bond between carboxylic and amine groups. The combination of sulfo-NHS as the coupling

## THEORETICAL BACKGROUND

reagent can substantially increase the linking efficiency compared to the reaction which only uses carbodiimide EDC. This covalent method is easy to perform and requires no further modification for the antibody to preserve its intact structure. However, the orientation of antibodies on the NP surface is random due to randomly orientated primary amines in the antibody. Hence, the modification site on the antigen binding part (Fab region) would block the recognition of the targeted protein and hence reduce the targeting efficiency.

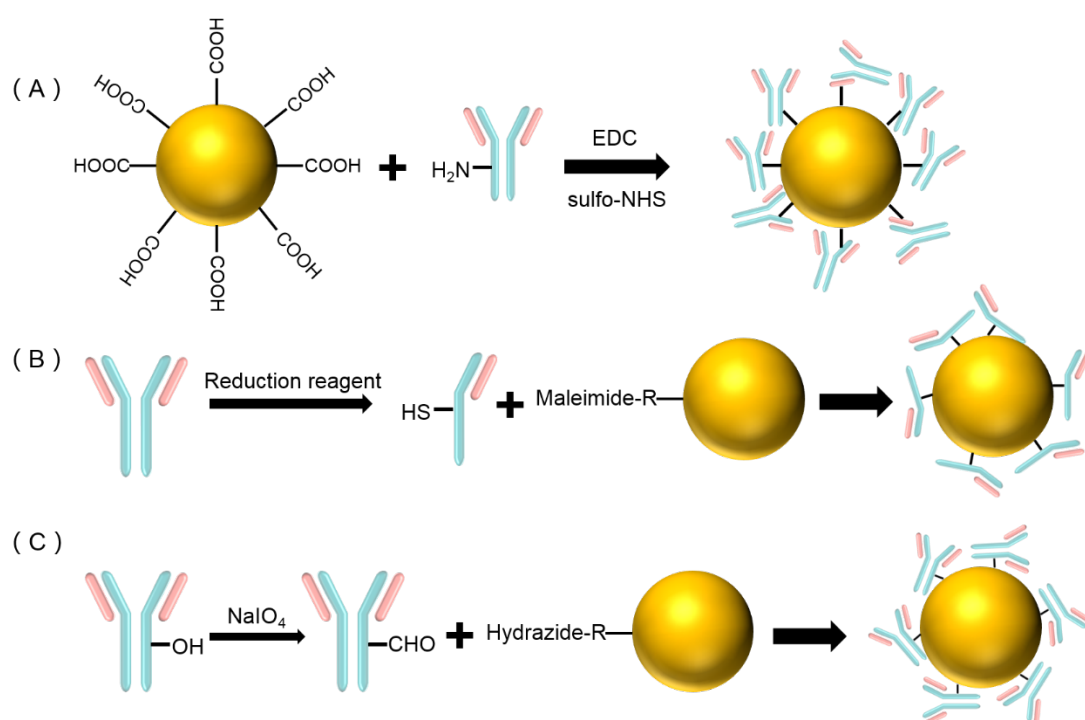


**Figure 2.13 | Three commonly used methods for covalent conjugation of antibodies onto AuNP. (A)** EDC/sulfo-NHS coupling strategy for linking antibodies onto NP via the amide reaction. **(B)** Antibody conjugation strategy dependent on the functional group of sulfhydryl. **(C)** Antibody conjugation via the aldehyde/hydrazine reaction.

Another covalent method depicted in **Figure 2.13 (B)** is based on the immobilization of sulfhydryl groups in the antibody which are generated via the cleavage of the disulfide bond in the hinge region of two heavy chains by 1,4-dithiothreitol and tris(2-carboxyethyl) phosphine (Sharma and Mutharasan, 2013; Zhang et al., 2016). Hence, the attachment of antibodies onto NPs can be obtained by the alkylation reaction

## THEORETICAL BACKGROUND

---

between the sulfhydryl group and maleimide-functionalized NPs. The resulting thioether bond is stable and the formation is irreversible. In addition, the selective modification of sulfhydryl groups leads to the directional orientation of the antibody on the surface of NPs and could increase the immuno-recognition efficiency.

**Figure 2.13 (C)** shows the directional way to conjugate antibodies onto NPs (Kumar et al., 2008). The first step requires the cleavage of polysaccharide residues in the antibody by sodium periodate to produce the aldehyde group. Then, yielded aldehyde groups can be coupled to the hydrazide-modified NPs via the covalent reaction. Polysaccharide is mainly located in the Fc region of the antibody. Modification of generated aldehyde groups will keep the activated Fab region exposed to the antigen and give rise to the antibody-antigen binding. Moreover, it is worth noting that not every type of antibody is glycosylated. Therefore, this conjugation strategy is not universal and needs to be paid attention prior to use.

Besides the covalent conjugation methods described above, strategies of non-covalent conjugation are also widely used in many iSERS studies, shown in **Figure 2.14**.

Protein A (PrA) originating from *Staphylococcus aureus* and Protein G (PrG) from *Staphylococcus* are both cell wall receptors with strong affinity for the Fc region especially in IgG antibody. They are used to purify antibodies. Nowadays, great attention has been paid to explore their function to link antibodies onto NPs shown in **Figure 2.14 (A)** or metal films (Lee et al., 2007; Salehi et al., 2014; Wu et al., 2012). Prior to the attachment of antibodies, PrA/G are previously bound to NPs with carboxylic functional groups through the carbodiimide crosslinker chemistry. In the presence of PrA/G, antibodies can be directionally modified onto the surface of NPs automatically without additional chemical reagents. The well-orientated antibody

conjugation approach has shown excellent labelling performance in our previous work (Salehi et al., 2014).

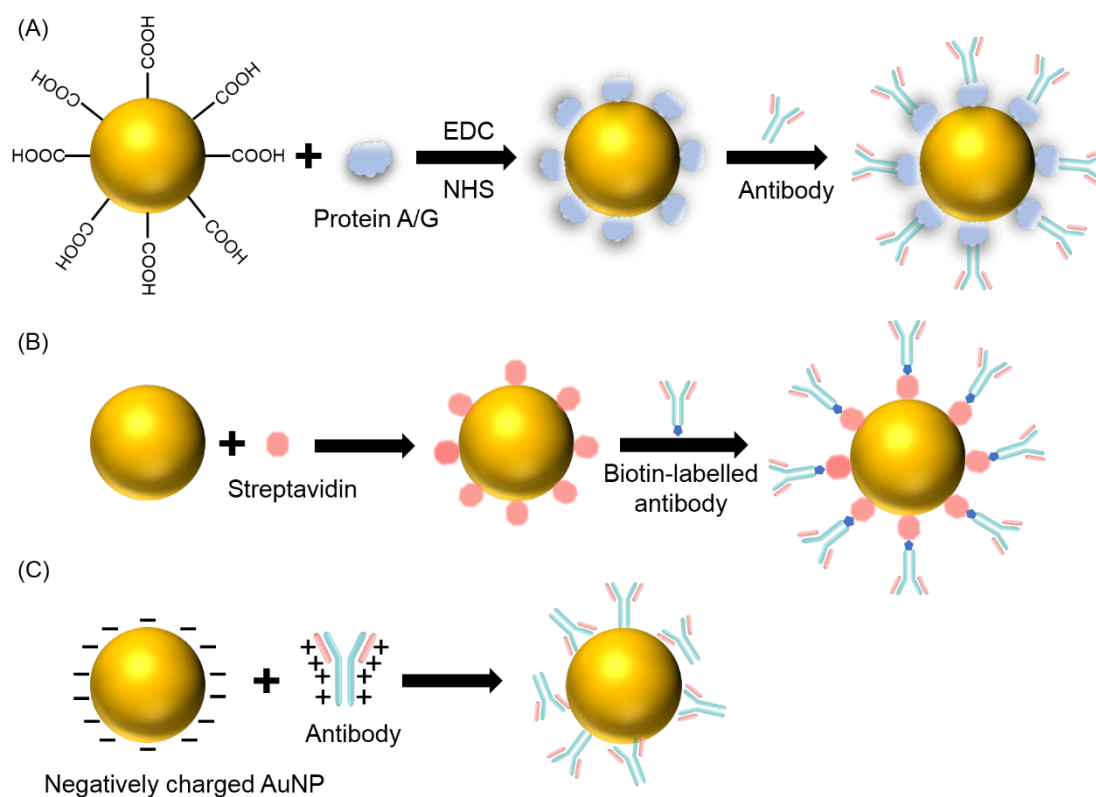


**Figure 2.14** | Three commonly used non-covalent strategies for conjugation of antibodies onto AuNP. **(A)** PrA/G-assisted binding of antibodies onto NP. **(B)** Antibody conjugation depending on the streptavidin/biotin interaction. **(C)** Antibodies assembled to the surface of negatively charged AuNP via electrostatic interactions.

The alternative way is to make use of the robust interaction between streptavidin and biotin. Streptavidin extracted from *Streptomyces avidinii* is the protein with around 50 KD molecular weight containing four binding sites for biotin. As depicted in **Figure 2.14 (B)**, biotinylated antibodies can be conjugated non-covalently to NPs which are pre-coated with streptavidin (Huhtinen et al., 2004; Lai et al., 2011). In addition, avidin plays the same role as streptavidin but shows more unspecific binding, leading to the less utilization for biomedical application (Jones et al., 1987; Bayer and Wilchek, 1990).

## THEORETICAL BACKGROUND

---

The resultant biotin/streptavidin complex is highly stable and will not be affected by the ambient environment.

Another non-covalent way of conjugating antibodies onto NPs surface is through the electrostatic interactions (Park et al., 2009; Sokolov et al., 2003). As shown in **Figure 2.14 (C)**, antibodies with positively charged residues can be linked to the surface of citrate stabilized and negatively charged AuNPs. This process is spontaneously occurred without further modifications of antibodies. Herein, compared to covalent conjugation strategies, more concentrated antibodies are required to ensure the sufficient adsorption of antibodies onto NPs surface. Furthermore, conjugated antibodies are randomly oriented resulting in a decreased recognition efficiency against the corresponding antigen.

Recently, the reliable conjugation method using click chemistry is increasingly used in the linkage of antibodies and NPs in cancer cell imaging, cell enrichment and drug discovery (Haun et al., 2010; Liu et al., 2017b; Peterson et al., 2012; Xiong et al., 2016). Generally, the quick cycloaddition reaction initiated by the presence of azide and alkyne functional groups is termed as click chemistry. It can be divided into two categories depending on whether the copper ion is involved in the reaction. Herein, two main copper-free reactions are shown below as an example to introduce the general reaction mechanism.

## THEORETICAL BACKGROUND

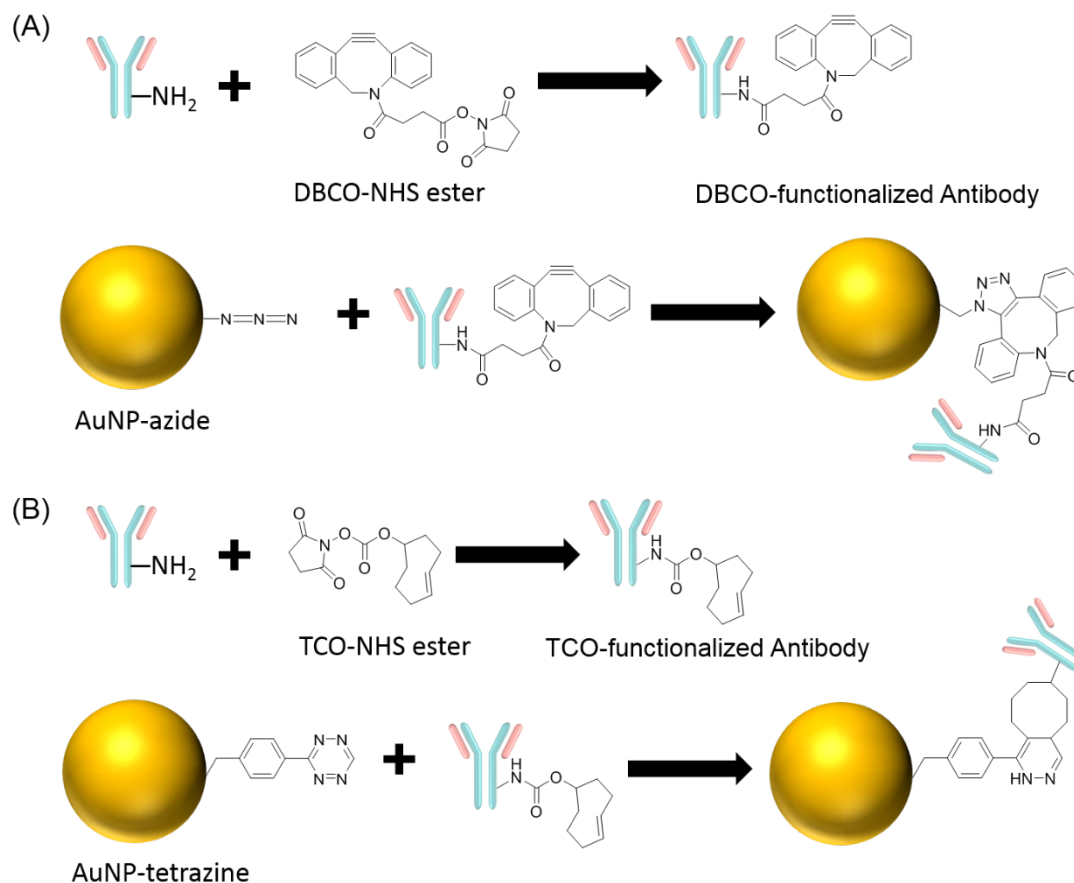


**Figure 2.15 | Conjugation of antibodies onto AuNP by click chemistry.**

**Figure 2.15 (A)** presents the dibenzylcyclooctyne (DBCO)-azide reaction (Xiong et al., 2016) and **Figure 2.15 (B)** shows the reaction of tetrazine-alkene ligation (Haun et al., 2010) for antibody conjugation, respectively. Herein, antibodies need to be modified with DBCO and trans-cyclooctene (TCO) groups via the amide reaction between DBCO-NHS ester (**Figure 2.15 (A)**)/TCO-NHS ester (**Figure 2.15 (B)**) and primary amines in the antibody. Antibody labeling with low interference of the background signal can be obtained due to the absence of functional groups of neither azide nor alkyne in native biomolecules such as DNA or protein. Moreover, the click reaction can be performed in aqueous solution within a wide range of pH.

### 3 Motivation and aims

Cancer diagnosis with high accuracy and sensitivity is still challenging. Generally, cancer is a disease induced by multi-factorial reasons. Biomarkers such as gene or proteins are a class of molecules used to indicate the presence of cancer (Gutman and Kessler, 2006; Petricoin et al., 2006; Rakha et al., 2007). Currently, many developed analytical methods detect one biomarker, which is not sufficient for screening out the tumourigenesis efficiently in biomedical applications. False-positive results could be generated leading to a wrong chemotherapy or surgery. Thus, it is imperative to develop multiplexing diagnostic methods to guide proper treatments for patients.

iSERS microscopy, a combination of the antibody for specific antigen recognition, plasmonic metal NPs as the SERS substrate and Raman microscopy, provides the specific recognition against the corresponding antigen in cancer diagnosis (Schlücker et al., 2006, Schlücker, 2009, Abramczyk and Brozek-Pluska, 2013; de Aberasturi et al., 2016; Qian et al., 2008b). The narrow band-width of the vibrational Raman signal compared to fluorescence enables iSERS microscopy to become an alternative important analytical approach for bio-imaging *in vivo* or *in vitro* (Bodelon et al., 2015; MacLaughlin et al., 2013; Webb et al., 2017).

Until now, the second leading cause of cancer death among women all over the world is breast cancer (Siegel et al., 2016). The breast carcinomas for this heterogeneous disease could be divided into three therapeutic groups: HER2 positive, estrogen receptor (ER)/ progesterone receptors (PR)-positive and triple-negative. Triple-negative breast cancer refers to breast cancer cells which have been tested for HER2, PR and ER negative. In 1989, Slamon et al. firstly reported that HER2 is a very important biomarker for breast cancer and have performed a number of studies on the HER2 status (Slamon et al., 1989).

HER2 is part of transmembrane receptor tyrosine kinases involved in the cellular growth, differentiation and development (Yarden and Sliwkowski, 2001). Overexpression of HER2 was found in 20-30% of breast cancers (Slamon et al., 1987; Slamon et al., 1989). Therefore, HER2 is regarded as a key biomarker for breast cancer prognosis. Since then, the investigation of HER2 status has been extensively applied for breast cancer detection and drug treatments (Bang et al., 2010; Piccart-Gebhart et al., 2005; Rubin and Yarden, 2001).

In this work, we first aim at the imaging of HER2 expression level on breast tissue sections by iSERS microscopy. Then, to obtain the reproducible imaging, optimization of experimental conditions will be conducted on single breast cancer cells. Furthermore, multiplexing capabilities of iSERS microscopy are investigated using newly developed SERS substrate on single breast cancer cells. Recent study has found that tumour cells could transfer to other organs of the body via the blood circulation (Chambers et al., 2002; Tarin, 2006). The examination of the original tissue for the disease is not sufficient to provide abundant information for precise diagnosis. Thus, the identification of breast cancer cells among cell mixture as a mimicking sample for cancer transfer is carried out in the last part via different SERS-labelled antibodies.

### 4 Materials and Methods

#### 4.1 Chemicals and materials

Acetonitrile	Fisher Scientific
Ascorbic acid	AppliChem
Biphenyl-4-thiol (4BPT)	Sigma Aldrich
Bovine serum albumin (BSA)	Sigma Aldrich
Biphenyl-4,4'-dithiol (BPDT)	Sigma Aldrich
Cetyltrimethylammonium bromide (CTAB)	Fluka
Cetyltrimethylammonium chloride (CTAC)	TCI
Citric buffer (pH=6.0)	Sigma Aldrich
4',6-Diamidino-2-phenylindole (DAPI)	Southernbiotech
Ethylenediaminetetraacetic acid (EDTA)	Sigma Aldrich
Ethanol (HPLC grade)	Fisher Scientific
Ethanolamine	Sigma Aldrich
Fast enzyme	Zytomed
Fetal calf serum	Gibco™
Fluor G	Southernbiotech
Hydrochloric acid (HCl)	Bernd Kraft
Insulin	Gibco™
L-Glutamine	Gibco™

## MATERIALS AND METHODS

---

McCoy's 5a medium	Fisher Scientific
Minimal essential medium	MEM, Gibco™
N-hydroxysulfosuccinimide sodium salt (sulfo-NHS)	Sigma Aldrich
Paraformaldehyde (PFA) solution	Affymetrix
1% Penicillin-streptomycin	Sigma Aldrich
Phosphate buffered saline (PBS) powder	Biochrom GmbH
Poly(ethylene glycol) 2-mercaptoethyl ether acetic acid (HS-PEG-COOH)	
	Sigma Aldrich
Poly(sodium 4-styrenesulfonate) (PSS)	Sigma Aldrich
Polyvinylpyrrolidon (PVP)	AppliChem
Sodium dodecyl sulfate (SDS)	Sigma Aldrich
Silver nitrate (AgNO <sub>3</sub> )	Sigma Aldrich
Sodium borohydride (NaBH <sub>4</sub> )	Sigma Aldrich
7.5% (v/v) Sodium bicarbonate	Gibco™
Sodium bromide (NaBr)	Sigma Aldrich
Sodium chloride (NaCl)	Bernd Kraft
Sodium pyruvate	Gibco™
Tetrachloroauric acid (HAuCl <sub>4</sub> )	Sigma Aldrich
Thio-2-naphthol (TN)	Sigma Aldrich
Trypsin-EDTA solution	Sigma Aldrich

## MATERIALS AND METHODS

---

Zyto Chem Plus HRP polymer system kit	Zytomed
1-Ethyl-3-(3- dimethylaminopropyl) carbodiimide (EDC)	Sigma Aldrich
4-Mercaptobenzoic acid (MBA)	TCI Chemicals
4-Methylbenzene thiol (4MBT)	Sigma Aldrich
4-Nitrothiophenol (NTP)	Fluorochem
4-(2-Hydroxyethyl)-1-piperazine ethane sulfonic acid (HEPES)	Sigma Aldrich
5,5'-Dithiolbis (2-nitrobenzoic acid) (DTNB)	Sigma Aldrich
7-Mercapto-4-methylcoumarin (MMC)	Sigma Aldrich
11-Mercaptoundecyltrimethylammonium bromide (MUTAB)	Sigma Aldrich
Confocal Raman microscope	WITec Alpha 300R
Dynamic light scattering (DLS)	Wyatt
Fluorescence microscope	Leica DMI6000
Hybridizer	Abbott
Mercury lamp	Leica
Milli-Q water system	Merck Milli-pore
Nanosight (NP tracking analysis)	LM-20 RAM-Germany
Poly-L-lysine slides	R. Langenbrink
Protein G strip	Biomol

## MATERIALS AND METHODS

---

Protein Lo-Bind tubes	Eppendorf
Superfrost <sup>TM</sup> glass slides	Fisher Scientific
Transmission electron microscopy (TEM)	Zeiss
Ultra-sonic bath	Elma
Ultraviolet-visible (UV-vis) absorption spectrometer	Jasco
Water bath	Carl Roth

## MATERIALS AND METHODS

Below is the detailed information about all antibodies used throughout the work. All purchased antibodies were directly used in this work without further modification or purification.

**Table 4.1 | A list of antibodies used in this work.**

Name	Species	Clone number	Concentration	Constituents	Company
Anti-HER2	Mouse	TAB250	0.47 $\mu\text{g mL}^{-1}$	unknown	Zytemed
Anti-HER2	Mouse	9G6	1 mg/mL	0.1% sodium azide, 0.2% gelatin, 50 mM sodium phosphate buffer	Abcam (ab16899)
Anti-EGFR	Rat	ICR10	1 mg/mL	0.09% sodium azide, PBS buffer	Abcam (ab231)
Anti-CD45	Rabbit	EP322Y	1.08 mg/mL	BSA and azide free	Abcam (ab214437)
Goat anti-mouse (Alexa647-labelled)	Goat	none	2 mg/mL	5 mM sodium azide	Thermofisher
Goat anti-sheep (Alexa647-labelled)	Goat	none	2 mg/mL	5 mM sodium azide	Thermofisher
Donkey anti-rat (Alexa488-labelled)	Donkey	none	2 mg/mL	5 mM sodium azide	Thermofisher

### 4.2 Metal NP synthesis and functionalization

#### 4.2.1 AuNS

AuNS were synthesized by the seed-mediated (Turkevich et al., 1951) method. In brief, 20 nm Au seeds were first prepared by citrate reduction. After that, 400  $\mu\text{L}$  of 20 nm Au seed NPs were added into a 15 ml Falcon tube. Then, 300  $\mu\text{L}$  of 2 mM  $\text{AgNO}_3$ , 150  $\mu\text{L}$  of 100 mM L (+)-ascorbic acid, 100  $\mu\text{L}$  of 2% w/v SDS, and 30  $\mu\text{L}$  of hydrochloric acid (HCl) solutions were added sequentially into the resultant solution. Afterwards, 10 mL of 750  $\mu\text{M}$   $\text{HAuCl}_4$  solution was added into the above mixed solution. Due to the instant formation of AuNS, the colour of the suspension turned from red to dark blue as displayed in **Figure 4.1**. The resulting solution was then maintained still for 15 min at RT. Subsequently, the mixture was washed twice by the centrifugation at 2200 rpm for 20 min and resuspended in Milli-Q water. Finally, UV-vis absorption spectroscopy and TEM were used for the characterization of LSPR and average size distribution. Meanwhile, a light scattering based single-particle tracking system (Nanosight) was applied for the determination of the concentration of synthesized AuNS ( $8 \times 10^{10}$  particles/mL).



**Figure 4.1 | Image of the synthesized AuNS.**

### 4.2.2 Electrostatic assembly of Au/Au core-satellites

Overall, the fabrication of Au/Au core-satellites was comprised of the synthesis of the super-spherical Au core and citrate-capped Au satellites.

First, Au nanospheres with an average diameter of 50 nm were prepared by a seed-mediated growth method in conjunction with the gentle oxidation. In brief, small Au nanospheres were prepared initially via the reduction of  $\text{Au}^{3+}$  in the solution of CTAB using  $\text{NaBH}_4$ . 0.25 mL of 0.01 M  $\text{HAuCl}_4$  solution was added into 9.75 mL of 0.1 M CTAB solution. Then, a freshly prepared ice-cooled  $\text{NaBH}_4$  solution (0.01 M, 0.6 mL) was immediately injected into the resultant mixture. The solution was then remained still for 3 h at 30 °C.

Next, small seeds of Au nanospheres were synthesized by the further addition of  $\text{Au}^{3+}$  together with the ascorbic acid in CTAB solution. 0.06 mL of small Au nanospheres were added to a growth solution containing CTAB solution (0.1 M, 4.88 mL), D.I. water (95 mL),  $\text{HAuCl}_4$  solution (0.01 M, 2 mL), and ascorbic acid solution (0.1 M, 7.5 mL) under gentle shaking. Afterwards, the mixed solution was kept still for 3 h at 30 °C. The resultant was washed by the centrifugation and redispersed in 25 mL of Milli-Q water.

To grow the above synthesized small Au seed in the solution of CTAC,  $\text{Au}^{3+}$  ions and ascorbic acid were added to form the larger nanopolyhedra. Here,  $\text{HAuCl}_4$  was used to oxidize Au polyhedron. 9 mL of the prepared seed solution was added into 180 mL of 0.025 M CTAC solution. Then, 4.5 mL of 0.1 M ascorbic acid and 9.0 mL of 0.01 M  $\text{HAuCl}_4$  solutions were added sequentially into the above mixture and the resulting solution was remained undisturbed for 3 h at 30 °C. The mixed solution was washed by centrifugation and redispersed in 30 mL of 0.02 M CTAB solution.

## MATERIALS AND METHODS

---

Last, with the further addition of  $\text{Au}^{3+}$ , the surface of the nanopolyhedra was etched to be smooth. 300 mL of 0.02 M CTAB solution and 1.08 mL of 0.01 M  $\text{HAuCl}_4$  solution were first added to 30 mL of the nanopolyhedron solution. The mixed solution was kept stirring for 2 h at 45 °C and then washed by centrifugation for two times. The precipitate was redispersed in 1.6 mL of Milli-Q water. Last, the synthesized super spherical Au nanospheres were characterized by TEM and UV-vis absorption spectroscopy.

The second part was to prepare citrate-capped Au nanospheres with a diameter of 30 nm by a kinetically-controlled seeded growth method (Turkevich et al., 1951). Primarily, seed particles were synthesized according to the classical Turkevich method. 317.5  $\mu\text{L}$  of 0.2 M  $\text{HAuCl}_4$  solution was added to 248.7 mL of water and then the resulting solution was boiled at 100 °C. Then, 1 mL of 0.425 M citrate solution was rapidly injected into the diluted  $\text{HAuCl}_4$  solution. The reaction was continued for 30 min under stirring and then the colour of the solution turned from colourless to red. The extinction spectrum of synthesized seeded solution was characterized with a LSPR band at 519 nm by UV-vis absorption spectroscopy. The mean size of AuNPs was  $16.8 \pm 1.3$  nm determined by TEM. The mixture was then cooled down to 90 °C. 1 mL of 60 mM sodium citrate and 1 mL of 25 mM  $\text{HAuCl}_4$  solution were sequentially added. After the incubation for 30 min, 2 mL of the colloid was taken out for the characterization of the size distribution and LSPR peak. By repeatedly adding 1 mL of 60 mM sodium citrate and 1 mL of 25 mM  $\text{HAuCl}_4$  solution, Au particles were grown larger every 30 min. The reaction was terminated when the size of resulting colloids reached to 30 nm.

Since Au core and satellites were prepared, a method of electrostatic assembly of Au/Au core-satellites was then developed by Matthias König. Briefly, 1000  $\mu\text{L}$  of pure ethanol (Analytical grade) was added first into the 1.5 mL protein Lo-Bind tube. Then, 120  $\mu\text{L}$  of 1.1 mM MUTAB dissolved in acetonitrile solution was added. After that,

## MATERIALS AND METHODS

---

18.3  $\mu\text{L}$  of 50 nm super-spherical AuNPs and 7.7  $\mu\text{L}$  of 250 mM NaBr solutions were added onto the cap of the Lo-Bind tube sequentially followed by vortexing for 30 seconds to ensure the homogeneity. Next, the mixture was kept overnight under shaking at RT. After the overnight incubation, AuNPs were adsorbed onto the wall of the tube and then 1 mL of ethanol was removed followed by adding 1 mL of Milli-Q water.

For the fabrication of six different SERS nanotags, a stock solution of Raman reporters in ethanol with the concentration of 5 mM was prepared firstly. For Raman reporter MMC, the solution needs to be prepared freshly to prevent the formation of precipitants. For Raman reporters 4BPT, 4MBT, MBA, NTP and TN, the stock solution could be stored for long-term use after preparation.

Then, 500  $\mu\text{L}$  of the resulting solution was then mixed with 5  $\mu\text{L}$  of 5 mM Raman reporter and incubated for 5 min (NTP) or 30 min (4BPT, TN, MMC, 4MBT, MBA). The mixed solution was then washed by two times of centrifugation with Milli-Q water and redispersed in 500  $\mu\text{L}$  of Milli-Q water shown in **Figure 4.2 (A)**.

For the assembly of satellites onto Au core, 100  $\mu\text{L}$  of Raman reporter-labelled Au core and 100  $\mu\text{L}$  of 0.6% PSS water solution were mixed with 700  $\mu\text{L}$  of 30 nm citrate-capped AuNPs. The colour of the solution as shown in **Figure 4.2 (B)** turned immediately from red to purple, indicating the successful assembly of satellites onto Au core. Last, the resultant was washed twice to remove the excess of reagents and redispersed in 700  $\mu\text{L}$  of Milli-Q water.

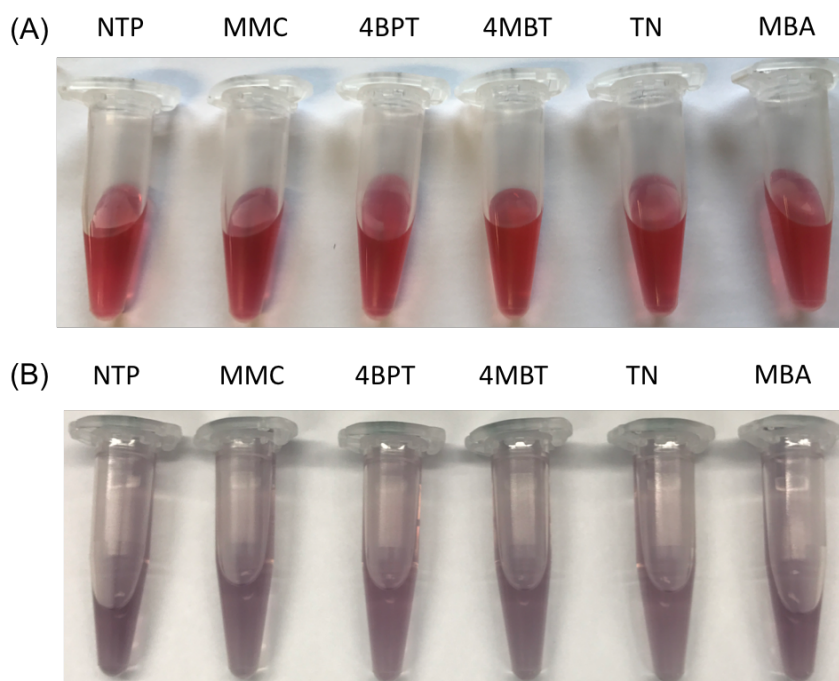


**Figure 4.2 | Pictures of the colloid solution. (A)** 50 nm spherical AuNPs incubated with six different Raman reporters. **(B)** Six different Raman reporter-labelled 50 nm AuNPs assembled with 30 nm Au satellites.

#### 4.2.3 Bioconjugation with antibodies

In section 5.1, the secondary antibody was conjugated onto SERS-labelled AuNS by the covalent conjugation via the dual self-assembled monolayer (SAM). This was achieved by the amide reaction between primary amines of the secondary antibody and carboxylic acid moieties of Raman reporter 2-nitro-5-thiobenzoate-triethylene glycol-carboxy (4-NTB-TEG-COOH). 5  $\mu$ L of 10 mM solution of hydrophilically stabilized molecules 4-NTB-MEG-OH (2-nitro-5-thiobenzoate-monoethylene glycol-hydroxy) and 4-NTB-TEG-COOH in ethanol were added into 1 mL of AuNS to offer the water solubility, bioconjugating capability and Raman activity for NPs. 4-NTB-MEG-OH and 4-NTB-TEG-COOH were synthesized using DTNB as a precursor according to a former reported method (Jehn et al., 2009). The mixed solution was then incubated overnight at RT under shaking to cover the whole surface of NPs with the dual SAM.

## MATERIALS AND METHODS

---

After the overnight incubation, the hydrophilically stabilized AuNS with Raman reporters were centrifuged once and redispersed in HEPES buffer. Then, freshly prepared 0.1 mM EDC and 0.25 mM sulfo-NHS were added for the activation of terminal carboxyl groups in Raman reporter 4-NTB-TEG-COOH for 25 min at RT. After the reaction, the remaining unreacted EDC and sulfo-NHS were removed by centrifugation and then NPs were suspended in HEPES buffer. Then, 8.1  $\mu\text{g}$  of Alexa647-labelled goat anti mouse secondary antibody was reacted with the mixture and incubated in the dark for 2.5 hours at RT. 10% of ethanolamine was added to the solution to deactivate unreacted carboxylic acid sites for 30 min at RT in the dark while shaking. Subsequently, AuNS-labelled secondary antibodies were washed with 2% BSA-PBS buffer solution for 4 times to remove free secondary antibodies and dispersed in 2% BSA-PBS buffer solution. The mixture was diluted to optical density (OD) of 1.0 for the following staining of tissue sections.

The covalent conjugation of antibodies onto AuNS by the dual SAM was also applied in the following reproducibility study in section 5.2. After the activation of EDC and sulfo-NHS, the primary anti-HER2 antibody was added to react with activated carboxyl groups for 2 hours at RT. Subsequently, the colloid solution was reacted with the ethanolamine for half an hour to block activated sites for reducing the unspecific adsorption. Finally, the mixture was washed with 2% BSA-PBS buffer solution three times and re-suspended in 2% BSA-PBS buffer solution and stored in the fridge at 4  $^{\circ}\text{C}$  for the following cellular staining.

In section 5.3, for the multi-colour localization of SERS probes onto the membrane of a single cell, a covalent conjugation method was used for attaching the antibody onto PEGylated Au/Au core-satellites. This method was also applied for the identification of breast cancer cells among the cell mixture by labelling anti-epidermal growth factor receptor (anti-EGFR), anti-cluster of differentiation 45 (anti-CD45) and anti-HER2

## MATERIALS AND METHODS

---

onto the surface of Au/Au core-satellites. Specifically, 500  $\mu\text{L}$  of 50  $\mu\text{M}$  HS-PEG-COOH (5 kD) was added into freshly assembled Au/Au core-satellites (700  $\mu\text{L}$ ) and incubated under shaking for 1 hour at RT. Then, the resultant was washed by the centrifugation to remove the excess of PEG molecules and redispersed in 500  $\mu\text{L}$  of HEPES buffer solution. The mixture was then immediately activated by adding 84  $\mu\text{L}$  of 4.9 mM EDC and 12.3 mM sulfo-NHS for 25 min at RT. After the centrifugation, the colloids were resuspended in 500  $\mu\text{L}$  of HEPES buffer solution. Then, in section 5.3, 2.5  $\mu\text{L}$  of 1 mg/mL anti-HER2 antibodies were added into six different PEGylated SERS nanotags, respectively. In section 5.4, 2.5  $\mu\text{L}$  of 1 mg/mL anti-HER2, anti-EGFR and anti-CD45 antibodies were added into three different PEGylated SERS nanotags, respectively. The above solution was reacted for 2 hours at RT, respectively. Afterwards, the mixture was maintained at 4  $^{\circ}\text{C}$  for the overnight incubation to ensure the sufficient reaction. Then, 50  $\mu\text{L}$  of 10% of ethanolamine was added into the resulting solution to block the excess of carboxylic acid sites for 30 min at RT in the dark. 2% BSA-PBS buffer solution was subsequently applied for the mixed solution to remove unbound antibodies by centrifugation for three times. Finally, SERS conjugates were suspended in 2% BSA-PBS buffer solution for the following iSERS staining.

In section 5.3, a PrG-coated strip was used to check whether the antibody was attached to the surface of NPs. Initially, Au/Au core-satellites-labelled with Raman reporters (NTP, TN, MMC, 4BPT, 4MBT or MBA) and anti-HER2 antibodies were prepared. Then, a PrG strip was immersed into the Eppendorf tube containing 40  $\mu\text{L}$  of PEGylated Au/Au core-satellites-labelled antibodies (six different SERS nanotags), IgG bound AuNPs and pure PEGylated Au/Au core-satellites, respectively. After the incubation for 10 min at RT, the PrG strip was taken out of each tube to check the appearance of the new band.

### 4.3 Tissue/cell preparation and treatment

#### 4.3.1 Tissue and cell slide preparation, fixation and blocking

The formalin-fixed paraffin-embedded (FFPE) breast tissue blocks were sectioned into slides with 1.5  $\mu\text{m}$  thickness for each slide using a microtom.

The human breast cancer cell line SkBr-3 and MCF-7 were supplied from American Type Culture Collection. MCF-7 cells were cultured in Minimal Essential Medium (MEM) supplemented with 10% (v/v) fetal calf serum, 1% (v/v) penicillin–streptomycin, 1% (v/v) MEM non-essential amino acids, 100 mM sodium pyruvate, 7.5% sodium-bicarbonate, 200 mM L-glutamine as well as 27 U  $\text{mg}^{-1}$  insulin. SkBr-3 cells were cultured in McCoy's 5a Medium supplemented with 10% (v/v) fetal calf serum, 1% (v/v) penicillin–streptomycin, 7.5% (v/v) sodium bicarbonate and 200 mM L-glutamine. The SkBr-3 and MCF-7 cells were grown in a humidified incubator containing 5% of  $\text{CO}_2$  at 37 °C. The trypsin–EDTA solution (0.05% trypsin, 0.02% EDTA) was used for the sub-cultivation. IHC was applied for the characterization of the cell line SkBr-3 as HER2 (3+) while the cell line MCF-7 was characterized as HER2 (0-1).

Mononuclear (MNC) cells (all CD45 positive) were isolated from the healthy donor EDTA blood by Ficoll-Hypaque density gradient centrifugation (density 1.077 g/mol; Pharmacia, Freiburg, Germany) at 400 g for 30 min. Cells from the interface were washed (400 g for 15 min) and resuspended in phosphate buffered saline.

An optimized number of  $0.1 \times 10^6$  cells (MCF-7, SkBr-3 or MNC) per area of 240  $\text{mm}^2$  were cytopinned on Poly-L slides at 1000 g for 6 min and air-dried overnight at RT. For spiking experiments, 50 SkBr-3 or MCF-7 cells were spiked into  $0.1 \times 10^6$  MNC cells. All the cell slides placed into the slide box are stored at 4 °C for long-term use.

## MATERIALS AND METHODS

---

For immunofluorescence (IF) or iSERS staining, cytopinned cell slides were primarily washed with PBS buffer solution in the slide rack (**Figure 4.3**) for three times to remove the remaining culture medium.

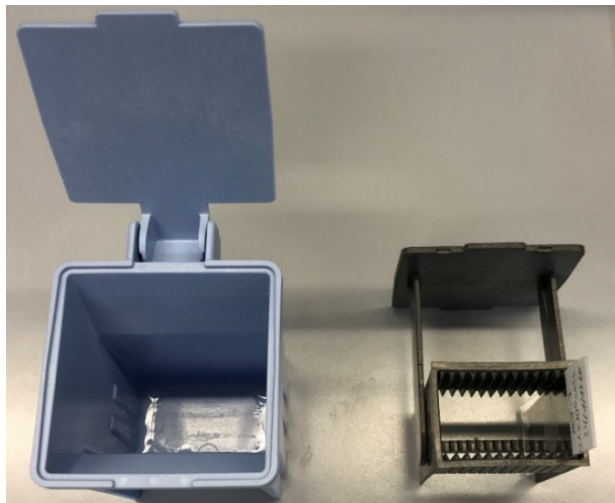


**Figure 4.3** | Picture of the slide rack for washing of the slides.

Then, the cell area on the slide was marked with PAP pen to form a hydrophobic barrier around the cell area in order to prevent the flowing of the solution (**Figure 4.4**). Next, 4% PFA solution was added onto cell slides to fully cover the cell region and were incubated for 15 min at RT for fixation. After the incubation, cell slides were washed with PBS buffer solution for three times to remove an excess of 4% PFA.



**Figure 4.4** | Image of the PAP pen used to draw a hydrophobic layer on the cell slide.

## MATERIALS AND METHODS

---

Generally, after the fixation while prior to adding the primary antibody, the slide needed to be incubated with the blocking reagent to reduce any unspecific binding as well as the noise of the background signal. The blocking step in either immunohistochemistry (IHC) or immunocytochemistry is an indispensable procedure. This is due to the unspecific binding between the antibody and surface proteins through electrostatic interaction, hydrophobic adsorption or other reactions. During the whole work, 2% BSA-PBS solution was added to slides and incubated for 2 h at RT to block reactive sites for avoiding the unspecific binding of the antibody or SERS probes. After the incubation with BSA, tissue sections or cell slides were directly replaced with primary antibody (tissue sections) or SERS-labelled antibodies (cell slides) without further washing. All incubation steps with slides were performed in a humidified chamber shown below (**Figure 4.5**).



**Figure 4.5** | Picture of the humidified slide box which was used for blocking and incubating antibodies and SERS probes with cell slides.

### 4.3.2 Deparaffinization of FFPE breast tissue sections

To meet the long-term storage along with the maintaining of the intact morphology of tissue sections, they are usually embedded with the paraffin after the formalin fixation. Paraffin, a solid at RT, is generally composed of a mixture of hydrocarbons. The melting point of paraffin used in histology is in the range of 56 °C to 58 °C. Therefore, tissue sections were firstly placed on the plate in the hybridizer with a capacity of 12 slides to let the paraffin melted at 60 °C for overnight.

Due to the immiscibility with water, paraffin needs to be removed by more concentrated ethanol baths. Xylol, a clearing reagent, was used to remove the paraffin. Then, tissue sections were rehydrated as follows (**Figure 4.6**):

1. The slides were immersed in xylol for 20 min.
2. The slides were immersed in ethanol (100%) for 1 min.
3. The slides were immersed in ethanol (96%)/water for 1 min.
4. The slides were immersed in ethanol (70%)/water for 1 min.

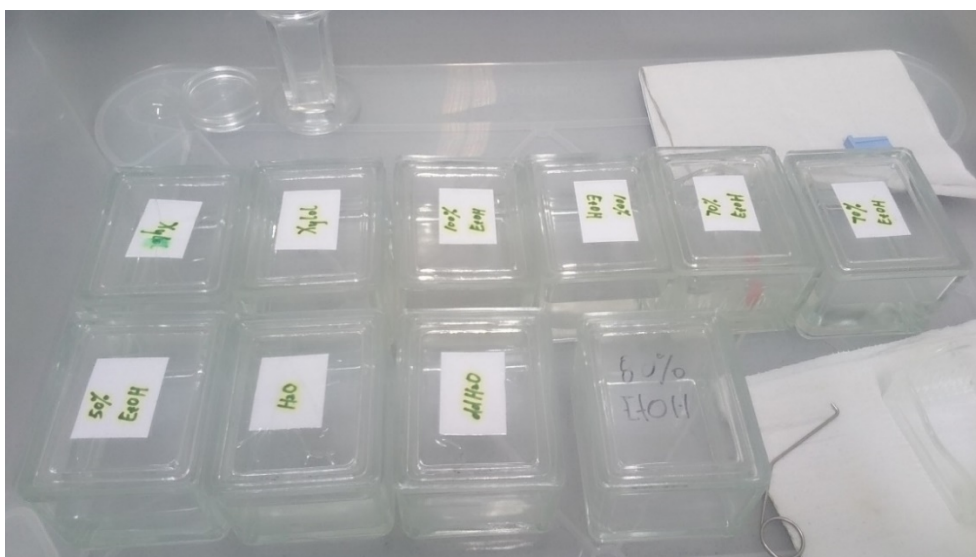


**Figure 4.6** | Picture of glass containers with various reagents for the tissue deparaffinization.

## MATERIALS AND METHODS

---

Finally, slides were rinsed with deionized water and then with PBS buffer. After above pretreatments, an antigen retrieval method was employed to expose epitopes of antigens on tissue sections.

### 4.3.3 Antigen retrieval

A protease-induced antigen retrieval (PIER) method was used for the wide-field fluorescence-guided iSERS imaging on breast tissue sections in section 5.1. Briefly, several drops of the fast enzyme were added onto tissue areas as presented in **Figure 4.7** and incubated for 5 min at RT. After that, slides were washed with PBS buffer solution for three times and then incubated with 2% BSA-PBS buffer solution for protein blocking.



**Figure 4.7 | Image with the reagents for enzymatic antigen retrieval of the breast tissue slide.**

For the investigation of the effect of antigen retrieval methods on the unspecific adsorption of SERS-labelled antibodies, a heat-induced epitope retrieval (HIER) was also performed on breast cancer tissue sections in parallel.

## MATERIALS AND METHODS

---

Tissue sections were heated in citrate buffer (pH=6.0) for 20 min at 96 °C in a water bath, then cooled in the same buffer for another 20 min. After that, tissue slides were washed with PBS buffer solution for removing the remaining citrate buffer.

### 4.4 IHC

The chromogenic IHC was first conducted to examine the preservation status of the HER2 structure on tissue sections using a Zyto Chem Plus horseradish peroxidase (HRP) polymer system kit. The breast cancer tissue slides were first placed in the hybridizer at 60 °C overnight. Then, the slides were treated with the deparaffinization, rehydration and enzymatic antigen retrieval sequentially. After that, 3% of H<sub>2</sub>O<sub>2</sub> solution was added onto tissue slides to block endogenous peroxidase activity. This is because the inherent peroxidases on tissue sections can be involved in the reaction of the substrate such as hydrogen peroxide and chromogen, generating a false positive signal. By applying the hydrogen peroxide previously, it could decrease the non-specific signal significantly.

Subsequently, PBS buffer solution was applied onto breast tissue slides to remove the excess of hydrogen peroxide for 10 min. Then, the slides were incubated with 2% BSA-PBS buffer solution to block for 10 min. After washing the slides, the primary anti-HER2 antibody with a dilution of 1:150 was added and incubated for 1 h at RT. The solution of HRP polymer was added onto the slide after the removal of unbound primary antibodies and incubated for 20 min. Herein, diaminobenzidine was added as a chromogen to incubate with the tissue slide for 10 min. Hematoxylin employed as the nuclear counterstaining agent was then added after washing slides with water. The mixed ethanol/water (70%, 96%, 100%, 1 min for each) was then applied to dehydrate tissue sections. Last, the mounting medium was added onto tissue slides.

### 4.5 IF

IF was performed to confirm the binding specificity of the antibodies as well as staining protocols used in this study. 2% BSA-PBS buffer solution was added onto tissue slides for blocking after the deparaffinization, rehydration and enzymatic antigen retrieval in section 5.1. Then, the primary mouse anti-HER2 antibody (1:150 dilution) was incubated with tissue slides for 1 h at RT under shaking. Subsequently, slides were immersed into and out of PBS buffer solution to remove unbound anti-HER2 antibodies for three times. Finally, Alexa647-labelled goat anti mouse secondary antibody (1: 300 dilution) was added onto tissue sections and incubated for 30 min at RT. After washing with PBS buffer solution for three times, tissue sections were dried for a short while and mounted with a mounting medium containing DAPI as a nuclear counterstain (**Figure 4.8**).

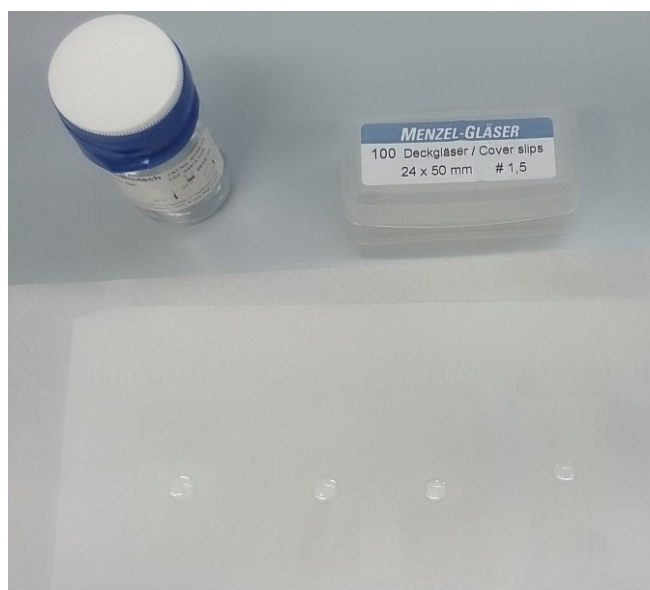


**Figure 4.8** | Mounting medium (DAPI) was added onto the coverslip for the counterstaining of the nucleus.

After adding the mounting medium, the stained slides were kept in the coloured slide box for subsequent imaging measurements (**Figure 4.9**).



**Figure 4.9 | The slide box for the storage of stained tissue or cell slides.**

For single colour (HER2) IF staining in section 5.2, after the fixation and blocking, the primary anti-HER2 (1  $\mu$ L) antibodies with a dilution of 300 times using 2% BSA-PBS buffer solution (300  $\mu$ L) were added onto cell slides and incubated for one hour at RT. After the incubation, the slides were washed with PBS buffer solution for three times and then incubated with Alexa647-labelled goat anti-mouse antibodies for half an hour. Alexa647-labelled goat anti-mouse antibodies were prepared with 300 times dilution. Finally, the slides were washed with PBS buffer solution and mounted with DPAI mounting medium for long time storage.

For the multiplex IF staining performed in section 5.4, a mixture of 1  $\mu$ L mouse anti-HER2 and 1  $\mu$ L rat anti-EGFR antibodies diluted with 300  $\mu$ L 2% BSA-PBS buffer solution was added onto SkBr-3, MCF-7 and MNC cell slides, respectively. Then, a mixture of Alexa647-labelled goat anti-mouse and Alexa488-labelled donkey anti-rat antibodies with 300 times dilution was added onto SkBr-3, MCF-7 and MNC cell slides after removing the excess of primary antibody. Then, the mounting medium containing DAPI was added onto slides for following microscopic interpretation.

## MATERIALS AND METHODS

---

For the single colour IF staining of CD45, primary rabbit anti-CD45 antibodies with a dilution of 1:300 were added onto MNC, SkBr-3 and MCF-7 cell slides respectively and incubated for 1 h after blocking. Then, Alexa647-labelled goat anti-rabbit secondary antibodies were added onto the above cell slides for 30 min after washing the slides with PBS buffer solution. After that, slides were washed with PBS buffer solution and mounted with DAPI mounting medium.

### 4.6 iSERS

For the tissue staining in section 5.1, primary anti-HER2 antibody was added onto slides for 1 h at RT after pretreatments. Then, the tissue slide was washed by PBS buffer solution to remove free primary antibodies and followed by the incubation with AuNS-labelled secondary antibodies ( $OD=1.0$  at  $\lambda_{max}=684$  nm) for 40 min at RT. After rinsing the slides with PBS buffer solution, unbound SERS conjugates were removed. The slides were covered with the mounting medium by the coverslip and stored in the fridge for further use.

For reproducible iSERS investigations in section 5.2, AuNS-labelled with dual SAM and anti-HER2 antibodies were applied onto cell slides after the blocking for one hour at RT under shaking. After removing unbound SERS probes with PBS buffer solution, Alexa647-labelled goat anti-mouse secondary antibodies with a dilution of 1:300 were added onto the slides to specifically bind the primary anti-HER2 antibody. Eventually, cell slides were rinsed with PBS buffer solution and covered by the mounting medium with the coverslip.

For six single-colour imaging experiments in section 5.3, 100  $\mu$ L of six different SERS nanotags (TN, NTP, MMC, 4BPT, 4MBT, MBA)-labelled anti-HER2 antibodies were added onto six various SkBr-3 cell slides respectively to fully cover the cell area and incubated for 80 minutes at RT under shaking. Then, slides were washed with PBS

## MATERIALS AND METHODS

---

buffer solution for three times to remove unbound NPs and then mounted with DAPI mounting medium. Same experiments were performed on the MCF-7 cell slide as negative controls.

For the multi-colour colocalization experiment in section 5.3, first two-, then three-, four-, five- and finally six-colour imaging experiments targeting HER2 localization were conducted sequentially. Firstly, SERS nanotag (MMC or 4BPT)-labelled anti-HER2 antibodies were prepared and resuspended in 50  $\mu\text{L}$  2% BSA-PBS buffer. Then, two-colour staining was carried out by adding the mixture of two SERS-labelled antibodies onto SkBr-3 cell slide followed by the incubation for 80 min at RT under shaking. Similarly, 33.3  $\mu\text{L}$  of SERS nanotag (MMC, 4BPT or TN)-labelled anti-HER2 antibodies was mixed and added onto SkBr-3 cell slide under same conditions for the three-colour experiment. Ultimately, four (MMC, 4BPT, TN, NTP), five (MMC, 4BPT, TN, NTP, 4MBT) and six-colour (MMC, 4BPT, TN, NTP, 4MBT, MBA) imaging of HER2 experiments were performed respectively only by varying the volume of corresponding SERS nanotag-labelled anti-HER2 antibodies to 25  $\mu\text{L}$ , 20  $\mu\text{L}$  and 16.7  $\mu\text{L}$ . All slides were mounted with DAPI mounting medium for the long-term storage with a coverslip after washing unbound Au/Au core-satellites conjugates.

The conventional IF imaging experiment was initially performed for demonstrating the overexpression of HER2 and EGFR on SkBr-3 slides and CD45 on MNC cell slides in section 5.4. Then, subsequent iSERS imaging experiments were performed on SkBr-3, MCF-7, MNC cell slides and the MNC cell slide spiked with 50 SkBr-3 cells respectively to validate the feasibility of the designed assay.

For the single colour imaging experiment in section 5.4, Raman reporters of BPDT, TN and MMC-labelled Au/Au core-satellites were used for coding CD45, HER2 and EGFR on MNC, SkBr-3 and MCF-7 slides, respectively. Au/Au core-satellites-labelled anti-

## MATERIALS AND METHODS

---

HER2 antibodies were prepared according to the above-mentioned method in section 4.2.3. Then, 100  $\mu\text{L}$  of each conjugate was added onto the corresponding cell slide after BSA blocking for 80 min at RT under shaking. Then, slides were mounted with DAPI mounting medium after the removal of unbound NPs by thoroughly washing with PBS buffer solution.

For the multi-colour imaging experiment in section 5.4, three different SERS nanotags (BPDT, TN and MMC) were prepared and then conjugated with anti-HER2, anti-EGFR and anti-CD45 antibodies, respectively. Then, a mixture of above Au/Au core-satellites-labelled antibodies (anti-HER2/anti-EGFR/anti-CD45) (33.3  $\mu\text{L}$  for each) was added onto the cell slides of SkBr-3, MCF-7 and MNC cell slide spiked with SkBr-3 cells, respectively. Finally, slides were washed with PBS buffer solution and mounted with DAPI mounting medium.

### 4.7 Instrumentation

UV-vis absorption spectroscopy is mainly used for the characterization of LSPR peak position as well as the concentration of the self-fabricated noble metal NPs. When a monochromatic light in the UV-vis spectral range irradiates the sample solution, the transmitted light with an intensity loss is due to the light absorption by a given chemical substance in a fixed container. For NPs, light scattering also contributes greatly to the intensity loss and thus extinction as the sum of absorption and scattering is important for NPs. The absorbance is calculated according to the Beer-Lambert law shown below:

$$A = \varepsilon c L. \quad (4.1)$$

Here,  $A$  is the measured absorbance, the constant  $\varepsilon$  is the molar extinction coefficient,  $c$  is the concentration of the tested solution and  $L$  is the light path length. It presents a linear proportional relationship between the concentration of the tested solution and obtained absorbance.

In this work, the base line correction is performed by measuring the blank sample solely containing the solvent suspension medium. A 1 mm quartz cuvette is used. All the extinction spectra were recorded with a Jasco V600 UV/vis absorption spectrometer.

All the TEM measurements in sections 5.1 and 5.3 were carried out using a Zeiss EM910 transmission electron microscope operating at 100 kV. The suspension of NPs for TEM measurements were generally prepared in ethanol. 2  $\mu$ L of the colloid solution was added onto the copper grid and dried for a while. Then, the grid was carefully put onto the sample holder in TEM for characterization.

All fluorescence and SERS mapping images for tissue sections and cell slides in this work were obtained by a home-modified confocal Raman microscope (WITec Alpha 300 R, 30 cm focal length and 600 grooves per mm grating spectrometer) installed with

## MATERIALS AND METHODS

---

an electron multiplying charge-coupled device (EMCCD) (Andor Newton DU970N-BV-353).

For the wide-field IF images, a high-pressure mercury lamp (LEJ LQ-HXP 120 VIS) was applied for the fluorescence excitation and a liquid waveguide was coupled to the illumination port of the microscope. In the path of excitation and emission, two bandpass filters centered at 628 nm and 692 nm with a bandwidth of 40 nm (Semrock Bright Line 628/40 HC and 692/40 HC) were placed, respectively. A T-coupler (Zeiss) with a transfer optic was installed to replace the fiber coupler to the grating spectrometer in the original Raman setup. At the end of the T-coupler, two ports were applied to be coupled with the grating spectrometer for Raman microscopy and a CCD (Zeiss AxioCam ICm1) respectively for fluorescence microscopy.

For all Raman mapping measurements, the 632.8 nm radiation from a HeNe laser was focused onto the sample using a 40× objective (Olympus) with a numerical aperture of 0.6. An integration time per pixel of 50 ms was used (sections 5.1, 5.3 and 5.4).

Prior to the Raman imaging measurement, a calibration for all spectroscopy components is performed to optimize the whole set-up which is an essential step for performing any Raman mapping experiment. In most cases, silicon is the best material for the purpose of calibration owing to no fluorescence or photo-bleaching. Therefore, a home designed silicon wafer on the glass slide with a coverslip was used for the calibration. As shown in **Figure 4.10**, a bright field image of the silicon wafer was first taken to adjust the focus of the glass slide. This was conducted by the coarse focus with a 10× objective and followed by the fine focus with a 40× objective. A sharp peak at 520  $\text{cm}^{-1}$  shown in **Figure 4.10 (C)** should be observed and subsequently the signal intensity was tuned to be the maximum. Then, a randomly selected region marked as a rectangular red box in **Figure 4.10 (A)** was used for the Raman imaging by the line

scan in the mapping mode. A false colour Raman imaging was acquired shown in **Figure 4.10 (B)**. The calibration for the Raman imaging was carried out until the image **(B)** matched the selected rectangular region in image **(A)**. Or else, a repeated Raman imaging measurement was conducted.

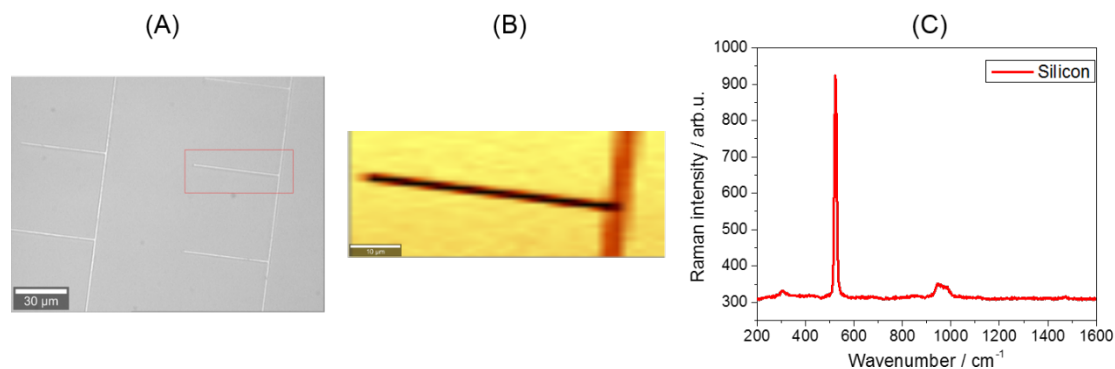


**Figure 4.10** | **(A)** The bright field image of the silicon wafer. **(B)** The false-colour Raman image for the selected rectangular region in image **(A)**. **(C)** Representative Raman spectrum of silicon.

DLS is extensively applied to measure the size distribution of NPs. The obtained variation of scattered light intensity is attributed to the Brownian motion of NPs suspended in solution illuminated by the incident laser light. The hydrodynamic radius of NPs can be then determined via the equation below:

$$D = \frac{k_B T}{6\pi\eta r} \quad (4.2)$$

where the translational diffusion coefficient  $D$  is obtained by the DLS,  $k_B$  is the Boltzman constant,  $T$  is the absolute temperature,  $\eta$  is the dynamic viscosity and  $r$  is the radius of particles.

Herein, a plastic cuvette containing 100 μL of NPs suspended in water was placed in the instrument of Wyatt for the measurement of size distribution via DLS.

## MATERIALS AND METHODS

---

Hybridizer shown in **Figure 4.11** is used to pre-heat tissue sections for melting the embedded paraffin in this work. It is commonly employed for the denaturation and hybridization of probes in fluorescence in situ hybridization or chromogenic in situ hybridization. The temperature can be set ranging from 30 °C to 99 °C. Different programs with a gradient change of temperature can be defined by the user. Meanwhile, the humidity in the incubator can be adjusted by placing the water- immersed tissue strips besides the heating plate.



**Figure 4.11 | Hybridizer used for the pre-heating of tissue sections.**

### **5 Results and Discussion**

#### **5.1 Analysis of HER2 expression on normal and breast cancer FFPE tissue**

##### **5.1.1 Motivation and background**

IHC, a traditional imaging technique, generally is applied for the global and fast diagnosis of the antigen expression profile on tissue sections. It requires multiple complicated staining procedures and results are read out usually by enzyme-linked colour reactions. The operation of all the procedures and interpretation of the results demand a well-trained expert and professional expertise. Furthermore, the false-positive results can also be attained. Thus, it could not meet the requirement of fast screening and precise diagnosis. On the other hand, IF is a widely applied method for the detection of the antigen (protein) on cells and tissue sections. However, many concerns have been raised in terms of the staining accuracy due to the inevitable auto fluorescence and photo-bleaching.

iSERS can solve the issue of autofluorescence, which is a main problem in IF for tissue analysis, by using the red to near-infrared laser excitation. The acquisition time in the iSERS imaging measurement is the key factor for the fast analysis. In 2006, our group performed the first iSERS experiment with the acquisition time of 1 s on the prostate tissue sections (Schlücker et al., 2006). Then, the acquisition time was decreased to millisecond range in 2014 due to the increased brightness of SERS nanotags (Salehi et al., 2014). In spite of the improvement of the shortened acquisition time, it is still hard for iSERS to scan larger areas. Generally, longer acquisition time is required to image large tissue areas using the spectra resolved mapping mode. Consequently, it is demanding that iSERS needs to be combined with a fast and global analysis through the wide field IF or IHC followed by the iSERS analysis to enable iSERS a fast imaging technique.

## RESULTS AND DISCUSSION

Herein, a correlative IF and iSERS-based technique for HER2 detection is developed with Dr. Yuying Zhang on FFPE breast tissue sections, the valuable resource for pathologists in clinical diagnosis.

The experimental approach of the configuration of SERS-active substrate and the immuno-staining of FFPE breast sections with AuNS-labelled secondary antibodies is shown in **Figure 5.1 (A)**. AuNS were capped with a dual SAM of Raman reporters 4-NTB-MEG-OH and 4-NTB-TEG-COOH. Consequently, AuNS-labelled secondary antibodies were both SERS-active and fluorescent. As shown in **Figure 5.1 (B)**, FFPE breast tissue section was firstly incubated with the primary anti-HER2 antibody after the deparaffinization and enzymatic antigen retrieval. Then, the unbound free primary antibodies were removed by washing the glass slide thoroughly with PBS buffer solution. In the end, the fluorescence and Raman signal were generated by adding Alexa647/AuNS-dual labelled-antibodies to recognize primary antibodies on the tissue section for HER2 localization.

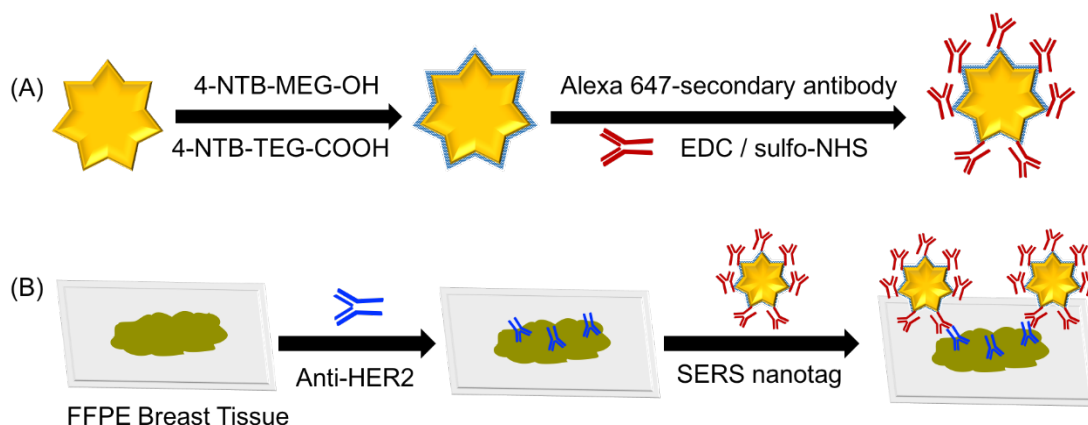


**Figure 5.1** | (A) Covalent conjugation of Alexa647-labelled secondary antibodies onto dual SAM-coated AuNS. (B) FFPE breast tissue section first incubated with primary anti-HER2 antibody and then with doubly-labelled secondary antibody. This figure originates from Wang et al., 2016 with adaptations.

## RESULTS AND DISCUSSION

---

The wide field fluorescence microscopy could generate a larger view of the field to guide the SERS mapping performed on the same area. This dual-imaging method can help to quickly distinguish the normal breast tissue and HER2 (3+) cancer tissue by monitoring the expression level of HER2 protein on the membrane of cells. Previous studies have been performed on breast cancer cells using NP-labelled antibodies, but none have done SERS imaging on FFPE breast tissue which is the invaluable resource for clinical diagnosis. Thus, this is the first study for the visualization of HER2 protein expression level on FFPE breast tissue sections via dual-imaging mode.

### 5.1.2 Characterization of SERS-active AuNS and antibody conjugates

The size distribution of synthesized AuNS was measured by TEM and shown in **Figure 5.2**. AuNS are comparatively uniform and the average size is around 76 nm. However, the number of tips on each Au nanostar varies from one to another. The branched structure of AuNS exhibits a very high enhancement of Raman signals from adsorbed molecules on the sharp tips due to the high local electric field excited by the laser light (Hrelescu et al., 2009; Yang and Jiang, 2016; Yuan et al., 2013). Besides, the dual SAM of Raman reporters-coated AuNS leads to the maximum SERS signal.

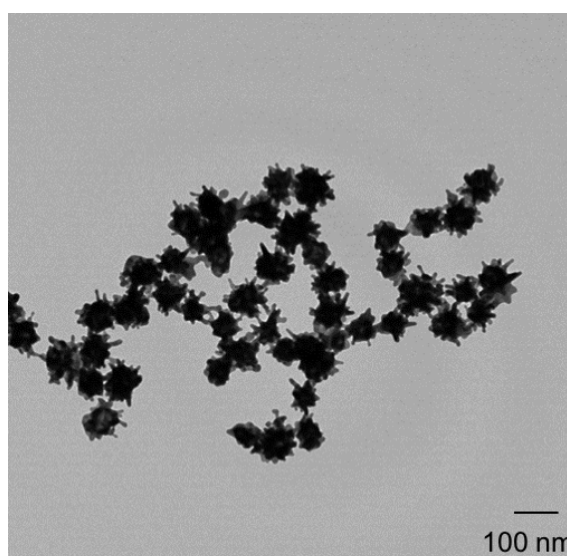


**Figure 5.2 | TEM image of AuNS.**

## RESULTS AND DISCUSSION

Raman reporter 4-NTB-MEG-OH comprises short hydrophilic ethylene glycol spacers as well as the hydroxyl group, which stabilize SERS particles and guarantee the good water solubility of AuNS. Raman reporter 4-NTB-TEG-COOH contains longer ethylene glycol spacers and a functional terminal carboxylic group, which enable the antibody to be conjugated through an amide reaction between the carboxylic group and the amine group with low steric hindrance. The chemical formulas of two Raman reporters are shown as **Figure 5.3**.

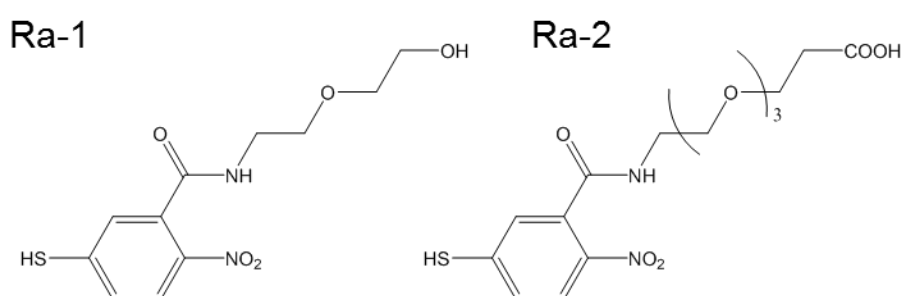


**Figure 5.3 | Chemical structure of the ethylene glycol-modified Raman reporter 4-NTB-MEG-OH (Ra-1) and 4-NTB-TEG-COOH (Ra-2).**

**Figure 5.4** presents UV-vis extinction spectra of a serial functionalization of AuNS by the dual-SAM and fluorophore-labelled secondary antibody. First, the LSPR peak of AuNS (red line) has a maximum in the red region ( $\lambda_{\max} \approx 666$  nm) in order to maximize SERS signal upon the illumination with red laser light (633 nm). Second, after adding Raman reporters of 4-NTB-MEG-OH and 4-NTB-TEG-COOH, there is a mild red shift of the LSPR peak (purple line), indicating the successful adsorption of the dual-SAM onto the surface of AuNS. Furthermore, the LSPR peak shows a further red shift after the incubation with the secondary antibody (green line).

## RESULTS AND DISCUSSION

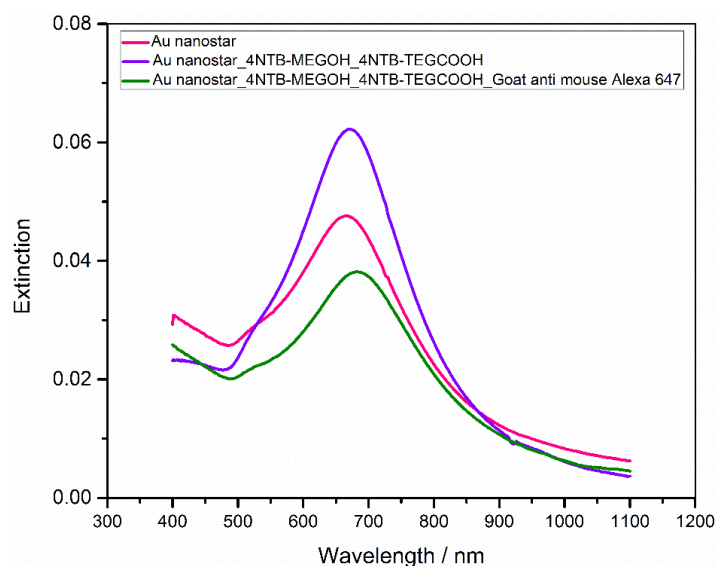


**Figure 5.4** | UV/vis extinction spectra recorded for monitoring the functionalization of AuNS with Raman reporters and antibodies, respectively. This figure originates from Wang et al., 2016 with adaptations.

After the co-adsorption of dual SAM Raman reporters, SERS intensity of the colloidal suspension in ethanol was recorded (**Figure 5.5**). The suspension medium ethanol has a strong SERS signal at  $883\text{ cm}^{-1}$ . The most dominant Raman peak at approximate  $1340\text{ cm}^{-1}$  in the SERS spectrum is assigned to the symmetric nitro stretching vibration of the Raman reporter 4-NTB.

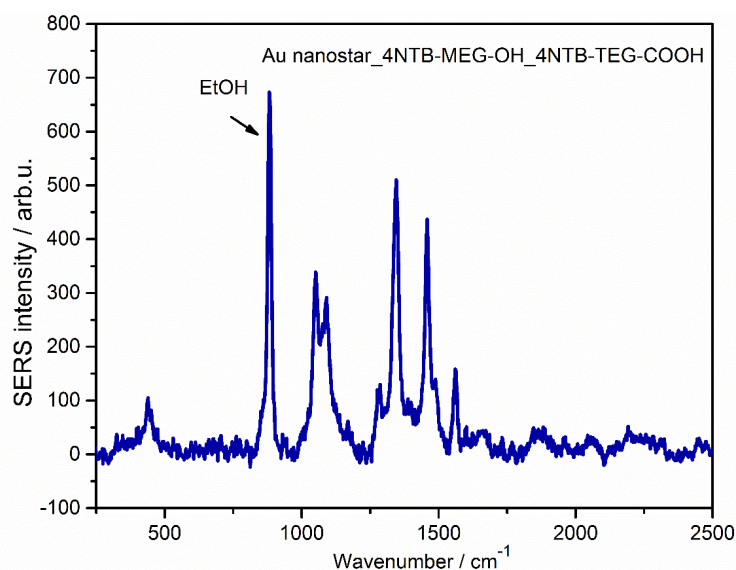


**Figure 5.5** | SERS spectrum of dual SAM-modified AuNS. This figure originates from Wang et al., 2016 with adaptations.

### 5.1.3 IHC and IF

HER2 was used as molecular biomarker for differentiation of the human normal and breast cancer tissue sections in this work. In order to check the feasibility and quality of staining processes, immuno-activity of the selected primary anti-HER2 antibody as well as tissue slides, IHC staining was firstly performed, which is the gold standard in clinics.

**Figure 5.6 (A)** shows that the membrane of nearly all breast cancer cells was stained in dark brown. In contrast, there was no staining on normal breast tissue (**Figure 5.6 (B)**). It is identified that the intact structure of HER2 antigen is well preserved even pretreated with the deparaffinization and proteolytic antigen retrieval based on above positive experiments.

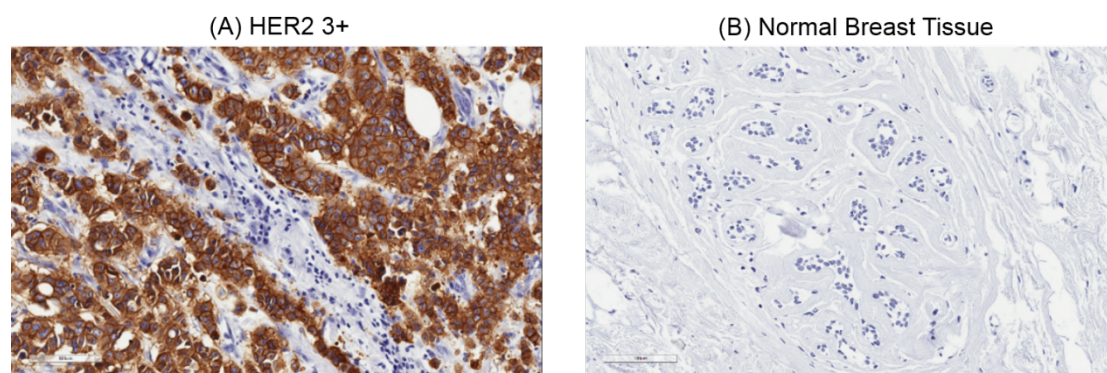


**Figure 5.6 | Localization of HER2 expression level on FFPE breast tissue sections by IHC staining of (A) HER2 (3+) breast cancer tissue and (B) normal breast tissue.** This figure originates from Wang et al., 2016 with adaptations.

After the confirmation of the antigen abundance and structure completeness by IHC, IF staining was further carried out. To investigate the HER2 expression level on the normal and breast cancer tissue specimen, both tissue specimens were treated with the same staining procedures by incubation with the primary anti-HER2 and followed by the Alexa647-labelled secondary antibody. The fluorescence signal generated from the secondary antibody allows the localization of HER2 under the fluorescence microscopy.

## RESULTS AND DISCUSSION

---

IF images of HER2 staining on HER2 3+ and normal breast tissue sections are shown in **Figure 5.7**. Bright fluorescence signal was observed in **Figure 5.7 (A)** left on HER2 3+ breast tissue section while almost no signal was in **Figure 5.7 (B)** left on normal breast tissue section. Furthermore, DAPI was used to stain the cell nuclei on both tissue sections (**Figure 5.7** middle). The fluorescent and DAPI images were merged in **Figure 5.7** right, showing the abundant expression level of HER2 on HER2 3+ tissue sections according to the completely stained cell membrane by the fluorophore-conjugated secondary antibody. On the contrary, there was almost no staining of membranes observed in the epithelial cells on the normal breast tissue section.

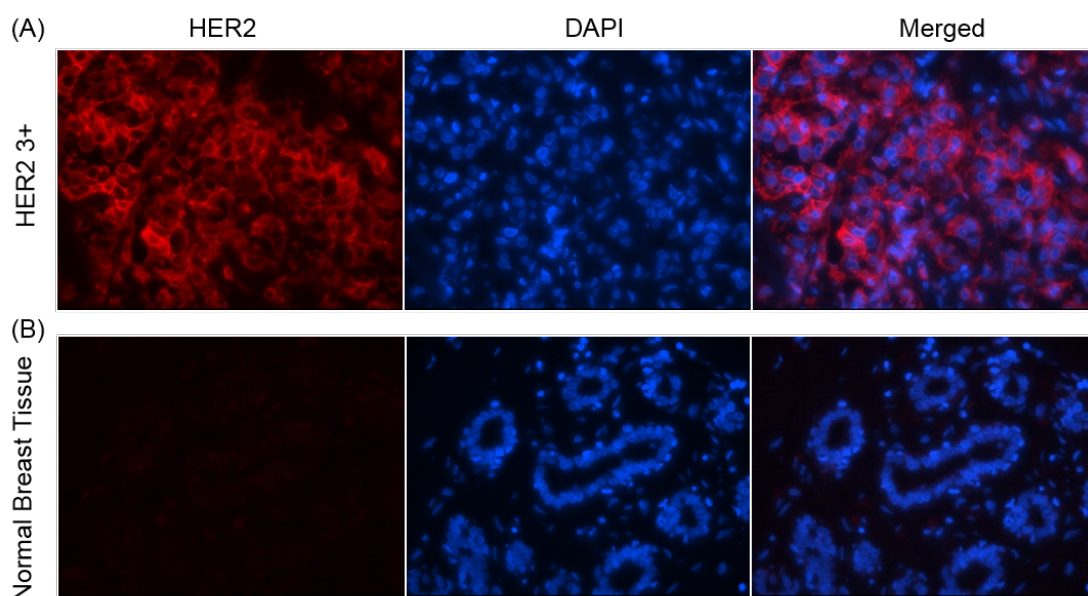


**Figure 5.7** | IF staining of HER2 on (A) HER2 (3+) and (B) normal breast tissue sections. This figure originates from Wang et al., 2016 with adaptations.

In summary, IF images were recorded as the first step to have a larger view on tissue sections, which could be used as the guidance for choosing relatively smaller areas of interest for performing subsequent iSERS microscopy.

### 5.1.4 PIER and HIER

It is essential to perform the antigen retrieval prior to IHC staining on FFPE tissue sections to expose denatured or hidden epitopes. PIER and HIER are the most commonly used antigen retrieval methods (Shi et al., 2011). Until now, the mechanism of antigen retrieval has not been resolved yet. Presumably, peptide bonds could be cleaved by PIER while formalin-induced cross-linkages are broken by HIER to expose determinants. The abundance of exposed epitopes on tissue sections is proportional to the SERS signal through the immuno reaction between the antigen and NPs-labelled antibodies. Therefore, the adsorption of NPs onto tissue sections is an important issue when using different antigen retrieval method. Thus, in this work, we initially compared HIER and PIER on the effect of NPs adsorption. After the exposure of the antigen HER2, IF and iSERS staining were conducted subsequently to check the effect of different antigen retrieval methods on the staining performance.

**Figure 5.8** shows the influence of the antigen retrieval method on the binding of SERS NPs onto breast FFPE tissue sections. The correlative IF-iSERS microscopic experiments performed on the normal and cancer breast tissue are shown in **Figure 5.8 (A)** and **(B)**, respectively. Specifically, after tissue sections pretreated with the enzymatic antigen retrieval, primary anti-HER2 was added to bind the HER2 antigen on the cell membrane and followed by the incubation with Alexa647/AuNS-dual labelled-goat anti mouse antibodies. **Figure 5.8 (A)** shows all cell membranes were stained fluorescent on the breast cancer tissue (HER2 3+) and the well-distributed SERS signal was observed from the selected cell. The IF and iSERS images show the same colour profile, implying SERS-labelled secondary antibodies were specifically bound to the cell membrane. In comparison, there was neither fluorescence nor SERS detected on the normal breast tissue presented in **Figure 5.8 (B)**.

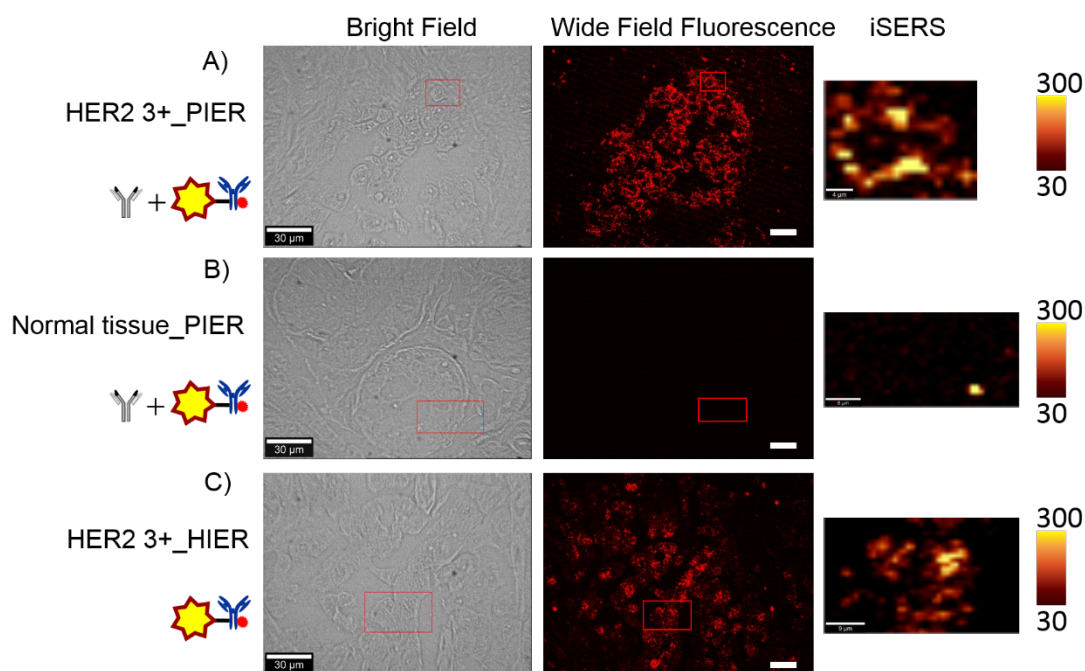


**Figure 5.8 | Correlative bright field (left) - IF (middle)-iSERS (right) microscopy for HER2 localization on FFPE breast tissue sections. (A)** iSERS staining of breast cancer tissue treated with PIER **(B)** iSERS staining of the breast normal tissue treated with PIER **(C)** breast cancer tissue (HER2 3+) treated with HIER and then incubated only with AuNS which were conjugated with Alexa647-labelled goat anti mouse secondary antibody for testing of the non-specific adsorption of SERS probes. The scale bar in the bright field and fluorescence images is 30  $\mu\text{m}$  and 4  $\mu\text{m}$ , 8  $\mu\text{m}$  and 9  $\mu\text{m}$  for (A), (B) and (C), respectively in the iSERS images. This figure originates from Zhang et al., 2018 with adaptations.

Whereas, non-specifically bound SERS probes were found on tissue sections pretreated with HIER (**Figure 5.8 C**), showing an entirely different staining quality compared to tissue sections treated with PIER. The results suggest that the antigen retrieval method could significantly affect the unspecific binding of SERS NPs onto FFPE tissue sections. To be specific, PIER treated antigen retrieval does not induce unspecific adsorption of SERS NPs onto FFPE tissue sections while HIER does for the current developed detection technique.

Thus, PIER was used to expose epitopes of the antigen on FFPE breast tissue sections during following experiments.

### 5.1.5 IF and iSERS microscopy

**Figure 5.9** displays correlative bright field-IF-iSERS imaging for HER2 localization on the normal and breast cancer tissue (HER2 3+) sections. In this work, Alexa647-labelled secondary antibody was covalently conjugated to Raman reporter-encoded AuNS to allow the correlative wide field IF and iSERS imaging on the same region. The fluorescence and SERS signal could be generated via dual labels.

The fluorescence image shown in **Figure 5.9 (B)** on HER2 (3+) tissue section reveals the specific staining of HER2 on the cell membrane by the fluorescence dye, which is consistent with results reported before. Then, a cell (marked with dark yellow box) in **Figure 5.9 (B)** was randomly selected to perform the confocal Raman mapping according to the IF image. **Figure 5.9 (C)** shows false-colour SERS images based on the integrated intensity of the characteristic Raman band at  $1340\text{ cm}^{-1}$ , attributed to the symmetric nitro stretching vibration of the Raman reporter 4-NTB.

In comparison, the same experiments were conducted on the normal breast tissue section. As shown in the lower row of **Figure 5.9 (B)** and **(C)**, neither fluorescence nor Raman signal was observed. This is in accordance with the known low/minimal HER2 expression level on FFPE normal breast tissue.

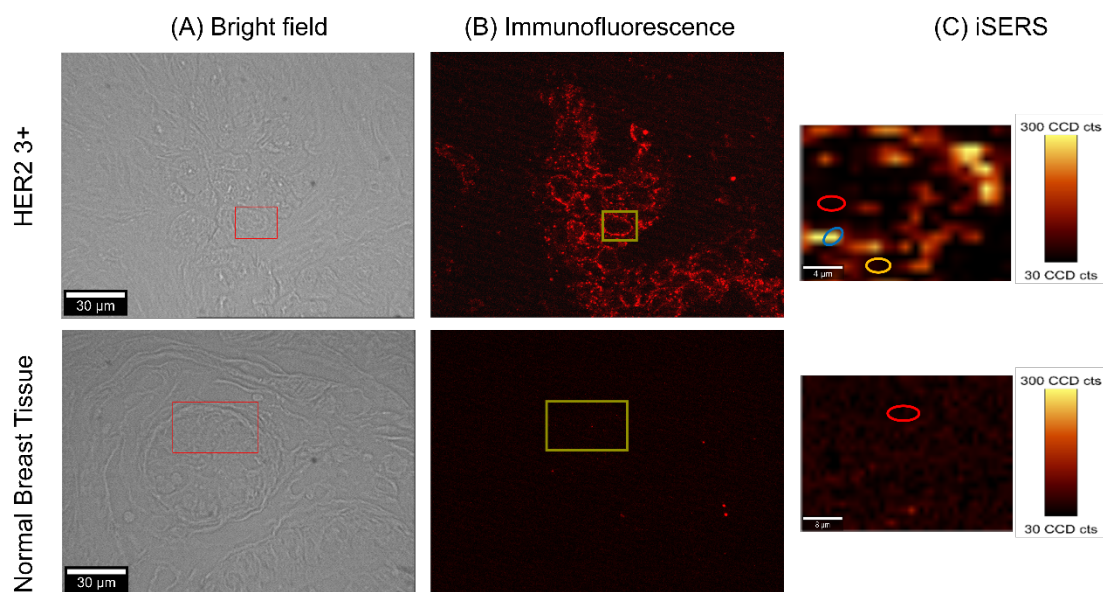


**Figure 5.9** | A Dual-mode IF and iSERS imaging microscopy for the normal and breast cancer tissue stained with AuNS and Alexa647-labelled secondary antibodies. (A) Bright Field. (B) Wide field IF. (C) iSERS false-colour image on a selected region. (colour scale: 30-300 CCD cts) This figure originates from Wang et al., 2016 with adaptations.

To further figure out whether the signal in above iSERS image is from vibrational spectra of Raman reporter 4-NTB, representative SERS spectra recorded at three distinct cellular regions: cell membrane, cytoplasm and the extracellular region indicated by circles in **Figure 5.9 (C)** in the corresponding SERS false-colour image are shown in **Figure 5.10**. The characteristic Raman signature at  $1340\text{ cm}^{-1}$  of the SERS nanotag was detected only on the cell membrane of cancer tissue as displayed in **Figure 5.10 (A)**. It indicates that iSERS microscopy has the capability to selectively localize HER2 on breast tumour cells and moreover SERS NPs will not damage the immunoreactivity of bound secondary antibodies against the primary antibody. In contrast, SERS signal was observed neither in the cytoplasm nor in the extra cellular region, which is consistent with the HER2 expression behaviour among the cellular structure. The same experiments were conducted on the normal breast tissue as a negative control. The spectrum shown in **Figure 5.10 (B)** recorded from the randomly selected region

(marked with red circle) in **Figure 5.9 (C)** (bottom row) indicates there is no obvious vibrational signal at  $1340\text{ cm}^{-1}$ . The plotted spectra in both **Figure 5.10 (A)** and **(B)** further show the very good specificity of the proposed iSERS imaging method.

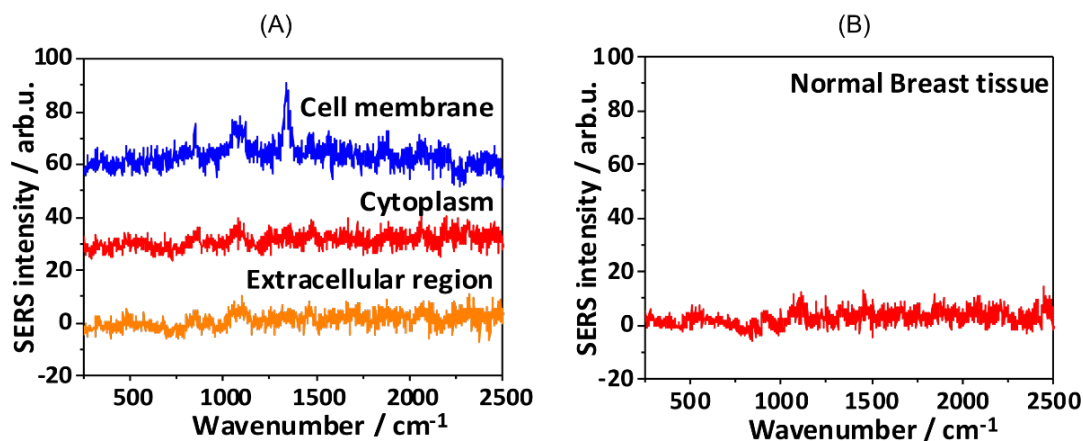


**Figure 5.10** | Representative Raman spectra recorded on (A) HER2 3+ breast tissue. (B) Normal breast tissue. This figure originates from Wang et al., 2016 with adaptations.

### 5.1.6 Negative control

Two additional negative control experiments were performed to have a better analysis for the staining of HER2 on breast tissue sections with SERS probes. The first negative control was performed without using the primary antibody. Since the secondary antibody only recognizes the primary antibody, but not directly the HER2 antigen itself, the fluorophore/SERS-labelled antibodies should ideally be completely removed from the tissue by washing. The staining result was shown in **Figure 5.11 (A)** and neither fluorescence nor Raman signal was observed as expected.

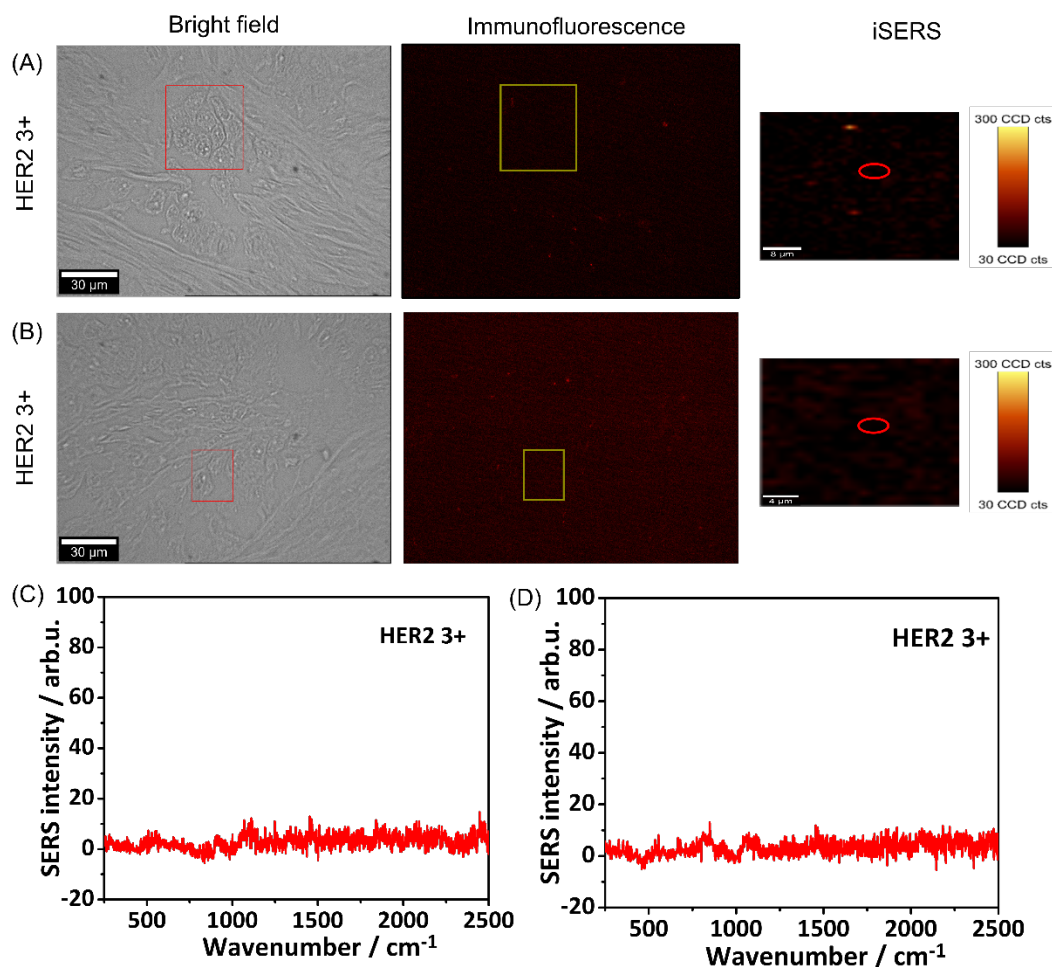


**Fig 5.11 | Two negative control experiments for HER2 imaging on FFPE breast tissue sections (HER2 3+).** (A) The tissue slide treated with Alexa647-labelled goat anti mouse secondary antibody without the incubation of the primary antibody. (B) The tissue slide treated initially with primary anti-HER2 and then with Alexa647-labelled goat anti-sheep secondary antibody. The bright field image, fluorescence image and false-colour iSERS image are presented sequentially in (A), (B). (C) and (D) are the representative SERS spectra measured on randomly selected point in (A) and (B), respectively. The colour scale in all false-colour iSERS images is 30-300 CCD counts. This figure originates from Wang et al., 2016 with adaptations.

Besides, we performed a second negative control by adding the goat-anti-sheep Alexa647-labelled secondary antibodies. Essentially, the secondary antibody bound to the primary mouse anti-HER2 should be against mouse and thus SERS probes conjugated with Alexa647-labelled goat anti sheep secondary antibodies would not

bind onto tissue sections. Therefore, neither fluorescence nor Raman signals were observed on the tissue section as shown in **Figure 5.11 (B)**.

The above negative controls further illustrate the well correlated iSERS false-colour image was acquired through the specific reaction between the primary anti-HER2 and fluorophore/SERS-labelled secondary antibodies. The represented SERS spectra shown in **Figure 5.11 (C)** and **(D)** were recorded from regions marked with a red circle in **(A)** and **(B)**, respectively. No obvious unique spectroscopic signature of Raman signal at  $1340\text{ cm}^{-1}$  was observed.

The experiments shown above demonstrate that our recorded dual-mode correlative images were solely by the specific staining of cells on tissue sections based on the binding between the primary antibody and AuNS-labelled secondary antibodies.

### 5.1.7 Long-term iSERS study

It is well known that the traditional imaging technique (IF) is limited due to the fluorescence quenching especially when the sample needs to be re-inspected. Thus, in order to investigate the capability of our proposed technique for a potential re-inspection by pathologists after certain time of storage, we performed iSERS imaging measurements on a tissue slide which was stained 51 days ago. The same experimental parameters such as laser power and integration time were used during all imaging acquisitions. The bright field image and false-colour image were displayed as **Figure 5.12 (A)** and **(B)**, respectively. For the selected rectangle-labelled region in **(A)**, similar cellular structure was observed in SERS false-colour image (**Figure 5.12 (B)**). Meanwhile, three representative Raman spectra following the former method were plotted as **Figure 5.12 (C)**, showing the apparent characteristic vibrational mode of Raman reporter 4-NTB at  $1340\text{ cm}^{-1}$ . Therefore, above results have shown our newly developed SERS imaging technique can be applied for the localization of HER2 on

## RESULTS AND DISCUSSION

breast tissue sections, providing the possibility for checking the imaging result after a certain period of time.

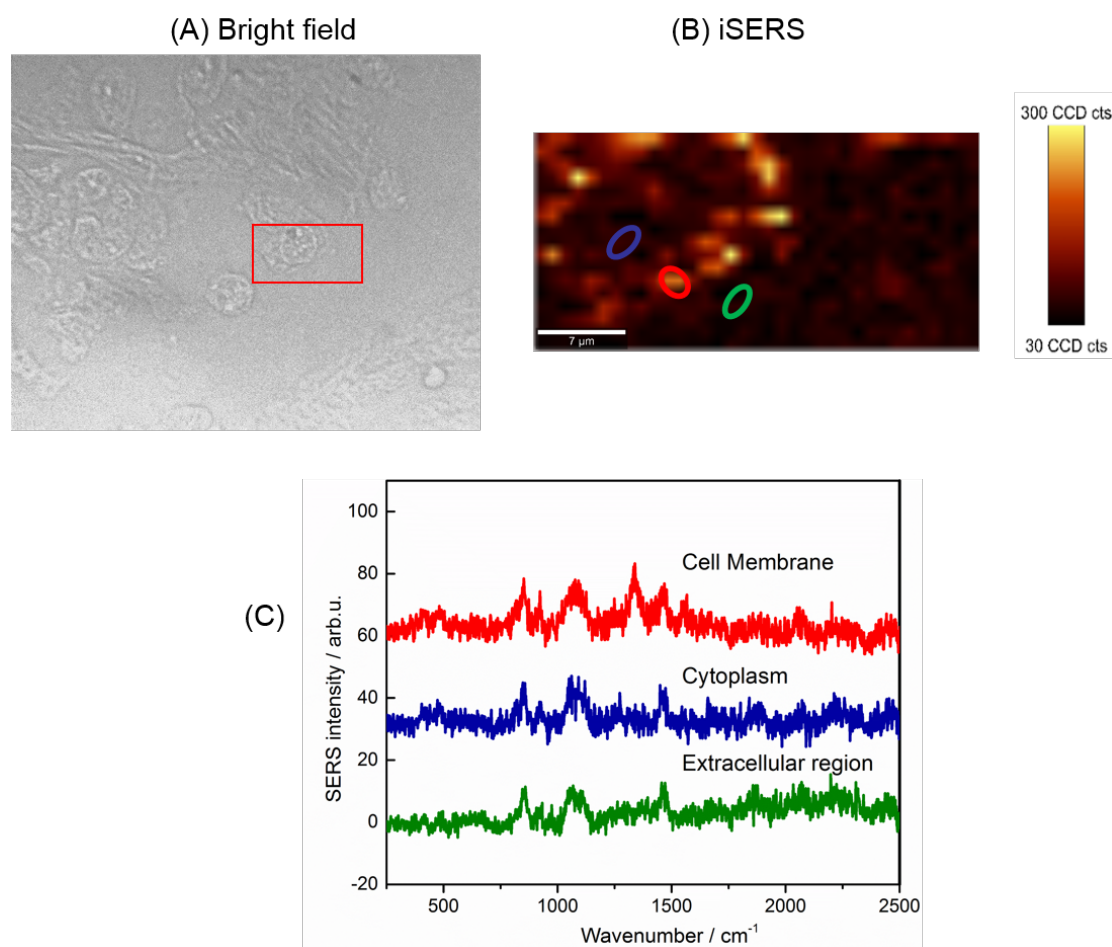


**Figure 5.12 | Confocal Raman imaging of FFPE breast cancer tissue sections stained 51 days ago. (A)** Bright field image of multiple cells on the tissue slide. **(B)** The false-colour iSERS imaging of a selected cell marked in a red rectangle in (A). **(C)** Normalized SERS spectra acquired from three various cellular locations marked with circles in (B). This figure originates from Wang et al., 2016 with adaptations.

### 5.1.8 Conclusions and outlook

A new approach of iSERS imaging combined with wide field IF for HER2 localization was demonstrated on FFPE breast tissue sections. A new rational design of SERS- and fluorescence-active probe was developed. The noble metal nanostructure of AuNS with many inherent hot spots provides significant SERS enhancement and then could be

## RESULTS AND DISCUSSION

---

applied as an efficient label for microscopic imaging. The attachment of secondary antibodies onto the metallic surface by the covalent conjugation through EDC/sulfo-NHS reaction enables the specific recognition of the corresponding primary antibody and further targets the antigen (HER2) on tissue sections. Initially, the global analysis was achieved by wide field fluorescence imaging and then guided the local imaging via iSERS microscopic experiments. Based on the regional analysis of HER2 expression, we have demonstrated the excellent imaging contrast obtained on normal breast and cancerous breast tissue sections through the proposed method. Furthermore, two negative controls illustrate the highly specific targeting of designed SERS probes. The plotted unique SERS spectra on three distinctive cellular regions give more detailed molecular information of HER2 protein distribution and demonstrate the abundant HER2 expression on the cell membrane. In addition, the re-inspection on the breast cancer tissue after a longer storage time was investigated and confirmed the good reproducibility of iSERS microscopy. The unique stability of SERS imaging provides the new insight into clinical diagnosis for breast cancer and could be applied as a potential imaging tool in clinics. Our proposed dual-mode imaging technique shows a highly selective imaging of HER2 localization to differentiate FFPE breast normal and cancer tissue sections.

Finally, given the small line width of the vibrational Raman band, iSERS shows a high multiplexing and provides the possibility of simultaneously imaging multi-biomarkers for diagnosis. This becomes more important when involved with the single tumour cell analysis disseminated into distant organs in breast cancer, especially in the bone marrow prior to the surgery. The independent prognostic significance of disseminated tumour cells (DTC) in the bone marrow as well as circulating tumour cells (CTC) has been illustrated (Hartkopf et al., 2014). They are recommended as potential cancer markers for minimal residual disease and rare members from primary tumour cells

## RESULTS AND DISCUSSION

---

involved in the late tumour progression. Therefore, the characterization of those highly heterogeneous cells is very important in order to verify their malignant origin, monitor phenotypic changes and get a better understanding of the mechanism of the metastasis. It will also be beneficial to identify related targets for diagnostic and therapeutic purpose and give the individual therapy for selected cancer patients. Moreover, HER2, ER and PR have shown their differential expression profile between the primary tumour and the corresponding metastasis and/or single cells in blood and bone marrow (Fehm et al., 2009; Simmons et al., 2009). Thus, targeting DTC and CTC will help to have a better prediction of cancer and therapeutic implications. The multiplex analysis through iSERS would enable screening the right drug for the individual patient and the unique stability of SERS imaging would provide the stable imaging tool for clinical diagnosis.

### 5.2 iSERS microscopy of single HER2-positive breast cancer cells

#### 5.2.1 Motivation and background

A key issue still in iSERS is how to acquire the Raman image in a short duration with high reproducibility. The overall acquisition time in iSERS microscopy in the confocal mapping mode critically depends on the acquisition time per pixel, which is related to the brightness of the SERS nanotag. In 2006, our group first demonstrated the proof of concept for the iSERS-based localization of prostate-specific antigen on FFPE prostate tissue using Au/Ag nanoshells with an acquisition time of 1s per pixel (Schlücker et al., 2006). Later, the acquisition time was reduced to 100 ms using AuNS and 30 ms by using silica-encapsulated dimers and trimers of AuNPs respectively (Schütz et al., 2011). In conventional Raman microscopy, higher laser power densities are typically applied for the compensation of the shorter acquisition time. However, the reproducibility of the results is usually not checked by performing repeated experiments on the same sample. Zhang et. al. recently have demonstrated the fast Raman iSERS imaging on cells and prostate tumours in mice model with great photo-stability using silica-coated gap-enhanced Raman tags (Zhang et al., 2017). However, to the best of our knowledge, this important aspect in iSERS microscopy with SERS-labelled antibodies has not been addressed so far.

It is very important for applications in molecular pathology and pharmacy to acquire the images with similar contrast in case the re-inspection of achieved clinical samples is needed. Therefore, the issue of reproducible and fast iSERS microscopy is investigated in the current study on single breast cancer cells.

Herein, we report the influence of the laser power intensity on the recording of the reproducible iSERS image on single breast cancer cells by targeting HER2 on the cell membrane with Au nanostar-labelled antibodies. The schematic approach of the iSERS

staining is shown in **Figure 5.13**. Briefly, AuNS-labelled antibodies were added onto the cell slide after fixation and blocking. After the removal of the unbound antibody-AuNS conjugates, the HER2 protein on the cell membrane was selectively stained with SERS-active AuNS. Then, the fluorophore (Alexa647)-labelled secondary antibody was incubated with the cell slides for wide-field fluorescence microscopy in order to have a broad view of the overall staining performance, guiding subsequent iSERS microscopic mapping experiments.

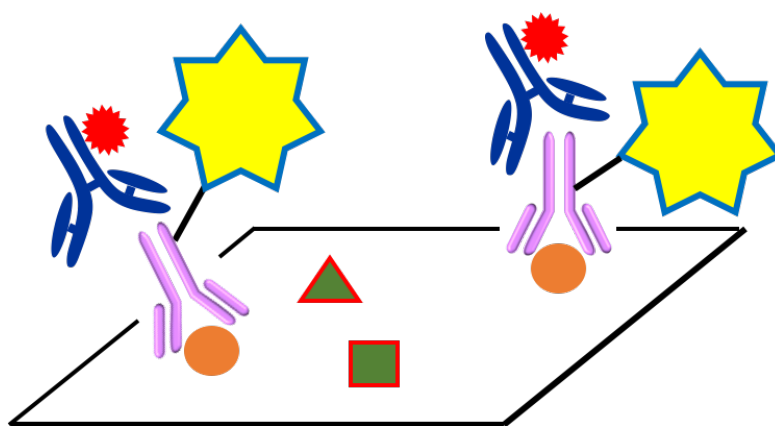


**Figure 5.13** | Schematic illustration of correlative iSERS/IF microscopy of the HER2 protein (orange circle) on a cyto-spinned breast cancer cell slide with the SERS-labelled primary antibody (purple) and the Alexa647 (red circle)-labelled secondary antibody (blue). This figure originates from Wang et al., 2017a with adaptations.

### 5.2.2 Optimization of the cell number on the slide

In order to perform single-cell imaging measurements on the glass slide, the first step is to optimize the number of breast cancer cells on the slide. Therefore, we prepared three slides with different cell numbers ranging from  $1 \times 10^6$  to  $0.1 \times 10^6$  cells per slide. Subsequently, we recorded a bright field image microscopy ( $40\times$  objective) for each cell number. **Figure 5.14** shows the images for different cell numbers. As shown in **Figure 5.14 (C)**, single breast cancer cells could be clearly differentiated among

multiple cells. In contrast, as shown in **Figure 5.14 (A) and (B)**, cells on the slides are too crowded to be differentiated from each other. Thus, a cell density of  $0.1 \times 10^6$  cells/slide was chosen for all following experiments.

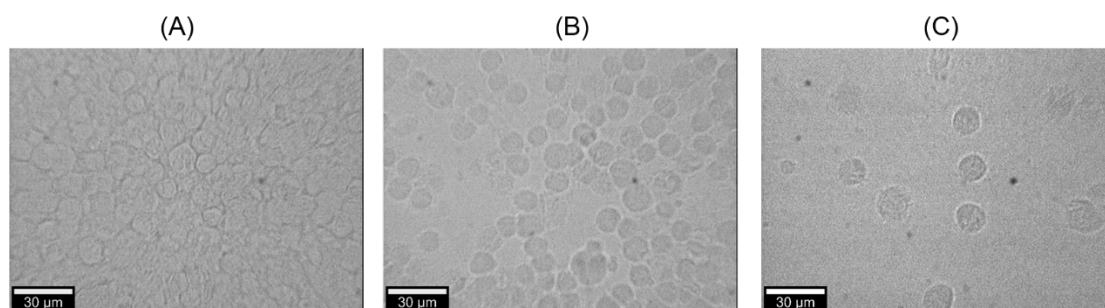


**Figure 5.14 | The optimization of the cell number on the slide. (A)**  $1 \times 10^6$  cells/slide **(B)**  $0.5 \times 10^6$  cells/slide **(C)**  $0.1 \times 10^6$  cells/slide.

### 5.2.3 IF and iSERS on single breast cancer cells

To validate the feasibility of the whole assay, we first performed SERS imaging measurements on SkBr-3 cell slides. **Figure 5.15** presents the correlative bright-field **(A)**, wide-field immuno fluorescence **(B)** and confocal iSERS mapping image **(C)** on the same SkBr3 cells with our home-built confocal Raman/wide-field fluorescence microscope. The bright field image in **Figure 5.15 (A)** was first recorded to ensure that the cell sample is in the focal plane. Then, the fluorescence image shown in **Figure 5.15 (B)** was recorded from the same area in the image **(A)** to obtain a fast overview of the staining of HER2 protein and then used as the guidance for subsequent SERS imaging measurement of a selected single cell. Specifically, herein we chose the single cell marked by the rectangular frames in **(A)** and **(B)**, respectively, for subsequent iSERS imaging. The false-colour SERS image in **Figure 5.15 (C)** exhibits the same spatial distribution of HER2 on the cell membrane as in **Figure 5.15 (B)**.

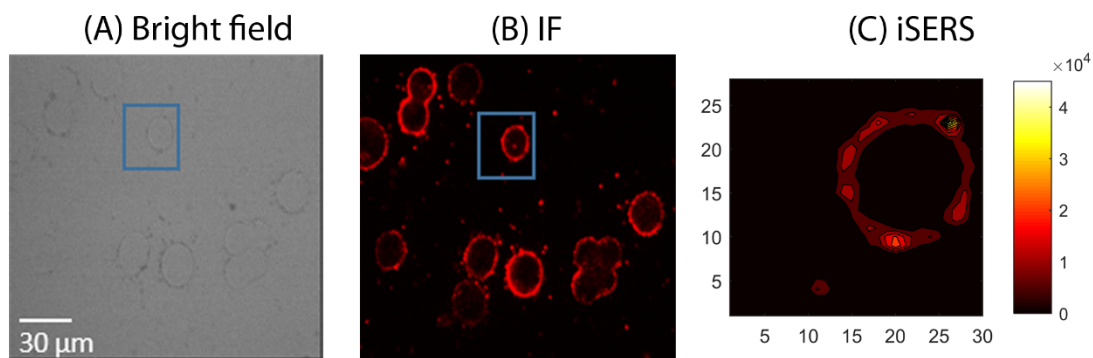


**Figure 5.15** | Correlative fluorescence and iSERS image from a single breast cancer cell. (A) Bright field, (B) Wide-field fluorescence, (C) False-colour iSERS image (laser power 2.32 mW, 40× air objective, integration time 0.05 s per pixel, and EMCCD gain switched on). This figure originates from Wang et al., 2017a with adaptations.

The SERS false-colour image in **Figure 5.15 (C)** was generated by the following method. First, Savitzky-Golay algorithm was used for smoothing of SERS spectra from the wavenumber of  $600\text{ cm}^{-1}$  to  $1800\text{ cm}^{-1}$ . Second, a baseline correction was applied according to the Whittaker-Henderson smoothing procedure (Eilers and Boelens, 2005). Third, the symmetric nitro stretching vibration of the Raman reporter 2-nitro-5-thiobenzoate, centered at  $1335\text{ cm}^{-1}$ , was used for the quantitative analysis. Each pixel in the false-colour iSERS image was determined by the maximum peak intensity centered at around  $1335\text{ cm}^{-1}$  through a Lorentzian line profile and a non-linear least square algorithm. In order to choose the pixels with relevant contributions in iSERS images, a binary mask was applied. The spectra with an intensity of more than 40 counts were kept, while other pixels were set to zero. Finally, the false-colour Raman/iSERS image was plotted based on the integrated Raman intensity of the entire fitted peak area.

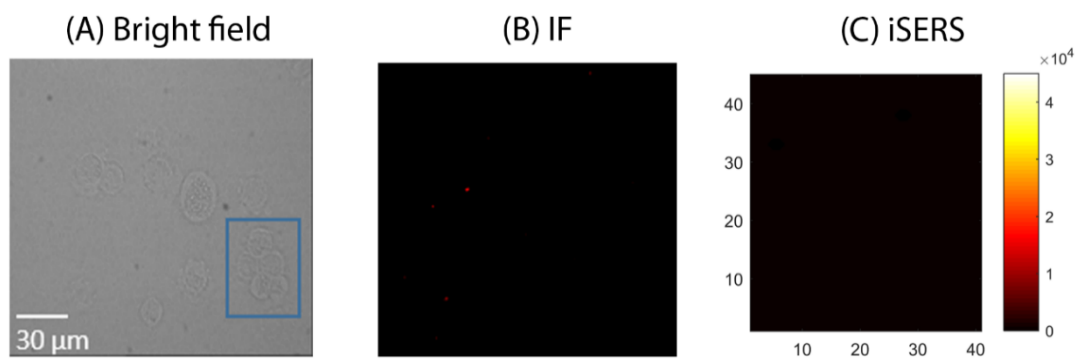


**Figure 5.16** | Correlative fluorescence and iSERS staining performed on a MCF-7 cell slide. The SERS-labelled primary anti-HER2 antibody and the Alexa-647-labelled secondary antibody were added to the slide sequentially. (A) Bright-field image, (B) Wide-field IF image, (C) False-colour iSERS image (laser power, 2.32 mW, 40× air objective, integration time 0.05 s per pixel, and EMCCD gain switched on). This figure originates from Wang et al., 2017a with adaptations.

The MCF-7 cell line, which almost has no expression of the HER2 protein, was selected as the negative control to check the specificity of SERS-labelled antibodies. Neither fluorescence in **Figure 5.16 (B)** nor SERS signal in **Figure 5.16 (C)** was detected when mapping several selected cells marked in the blue rectangle in **Figure 5.16 (A)**. The above results further confirm that the staining of HER2 using AuNS-labelled primary anti-HER2 antibodies is specific.

#### 5.2.4 Reproducibility of iSERS microscopy on single cells

The signal fluctuation in iSERS image acquisition has limited its advances towards commercial use as a routine diagnostic tool. Hence, the main concern is how to improve the photostability of the iSERS microscopic technique. Our strategy begins with the optimization of the laser power density together with the integration time, the two major contributing parameters when taking into account of experimental conditions.

As shown in **Figure 5.17**, a sequence of SERS images was taken to check the SERS imaging stability by changing the laser power and integration time firstly. To the best

## RESULTS AND DISCUSSION

of our knowledge, this is the first study for the investigation of the photostability of SERS imaging on single breast cancer cells by AuNS-labelled primary antibodies. The influence of the laser power as well as the integration time per pixel on the reproducibility of iSERS images was systematically investigated on cell slides in a series of experiments.

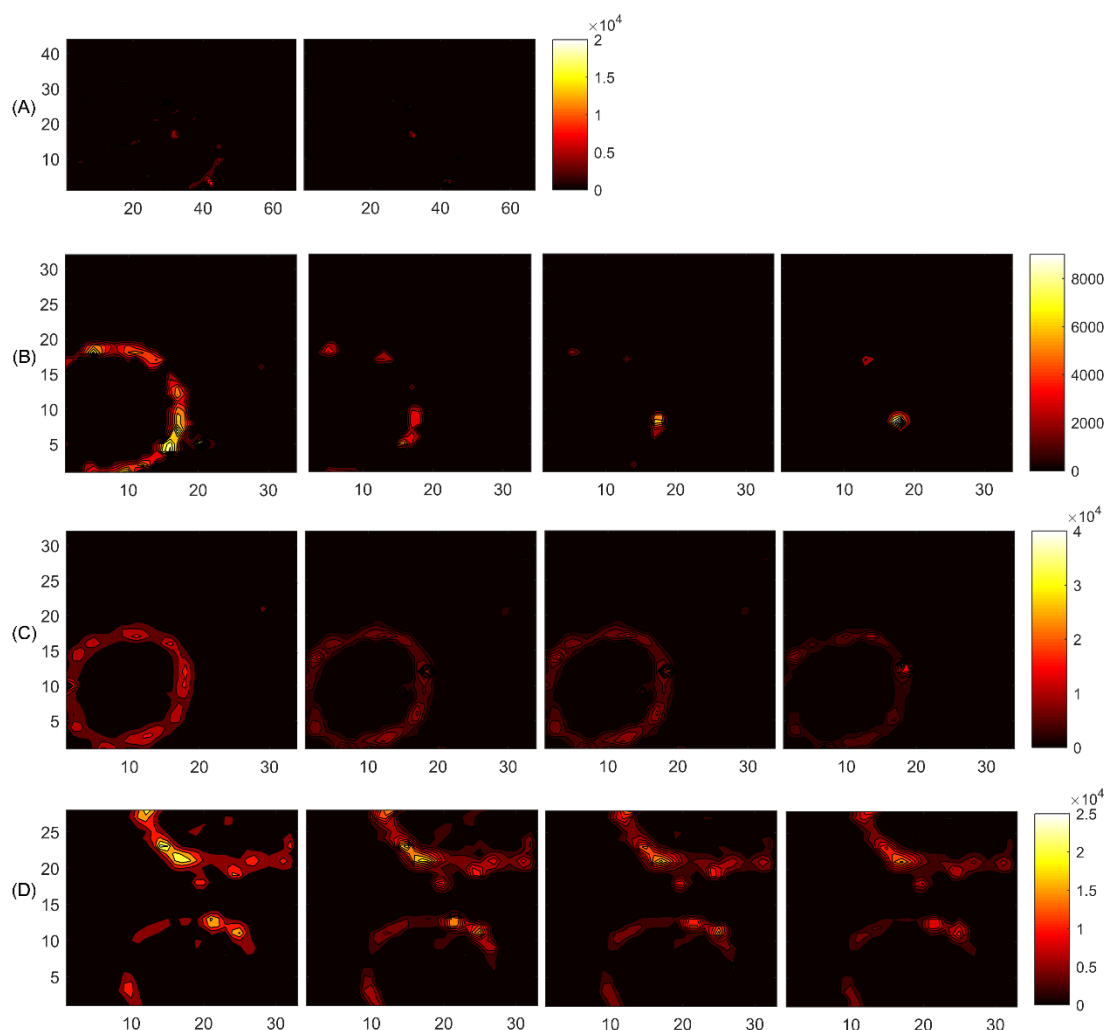


**Figure 5.17 | Non-reproducible false-colour SERS imaging measurements by decreasing the laser power and increasing the integration time for each pixel.** (A) Laser power 17.9 mW, integration time 0.1 s (B) Laser power 10.3 mW, integration time 0.2 s (C) Laser power 4.7 mW, integration time 0.4 s (D) Laser power 2.32 mW, integration time 0.8 s (conventional CCD mode without EM gain was used.). This figure originates from Wang et al., 2017a.

## RESULTS AND DISCUSSION

---

In the beginning, the laser power was tuned to be at the maximum of 17.9 mW to ensure the laser beam was enough to form the iSERS image with high contrast within a short period of acquisition time. Two repeated experiments were conducted under this condition. **Figure 5.17 (A)** clearly shows the significant loss of the SERS signal in the second run. It is proposed that the heating effect caused by the large laser power leads to the destruction of the chemical structure of the Raman reporter and therefore induced the SERS signal degradation in repeated measurements. Then, the laser power was decreased to 10.3 mW and the integration time was extended from 0.1 s in **(A)** to 0.2 s in **(B)** for signal compensation. Four imaging experiments were successively performed on the same breast cancer cell slide under the same experimental conditions. Surprisingly, the image contrast for the first measurement in **Figure 5.17 (B)** is much higher than in **Figure 5.17 (A)**. And the following three repeated measurements were shown to have a striking drop in the signal brightness compared to the first one. It is apparent that those conditions could not be used for reproducible iSERS microscopy on single cells. Therefore, the laser power is still needed to be reduced further. To guarantee the image contrast, the longer acquisition time is applied when using the lower laser power as the Raman signal is in direct proportion to the integration time as well as the laser power. Therefore, two other panels of laser intensity investigations on the iSERS imaging were performed. The images shown in **Figure 5.17 (C)** were recorded with the laser power of 4.7 mW and the integration time of 0.4 s. More reproducible iSERS images were attained by decreasing the laser power. Then, the laser power in **Figure 5.17 (D)** was reduced further to 2.32 mW compensated by doubling the integration time to 0.8 s in comparison with **Figure 5.17 (C)**. The imaging reproducibility becomes much better compared to **Figure 5.17 (A)** and an improvement compared to **Figure 5.17 (C)**. However, the long integration time in **Figure 5.17 (D)** will induce very long duration when screening lots of samples.

## RESULTS AND DISCUSSION

---

Thus, it is essential to acquire reproducible images with high contrast in a short duration of time. Since the conventional charge-coupled device (CCD) gain was used in all of above series of measurements, the gain function of EMCCD for increasing the additional signal was applied in following experiments to decrease the overall time for each imaging measurement.

Subsequently, we performed iSERS imaging on the single breast cell assisted with EMCCD sensor technology to provide the best fringe suppression and enable the delivery of high signal sensitivity with high scanning speed. The detection efficiency is greatly improved by integrating this technology into the imaging process.

**Figure 5.18** shows three groups of reproducible iSERS images obtained on the single breast cell with a laser power of 2.32 mW, 1.24 mW and 0.49 mW, respectively. By applying the function of EMCCD gain, the integration time was reduced from 0.8 s in **Figure 5.17 (D)** to 0.05 s in **Figure 5.18 (A)** while the intensity of the laser power was retained. Obviously, iSERS images with high reproducibility could be obtained with the combination of low laser power, short acquisition time and high EM gain.

## RESULTS AND DISCUSSION

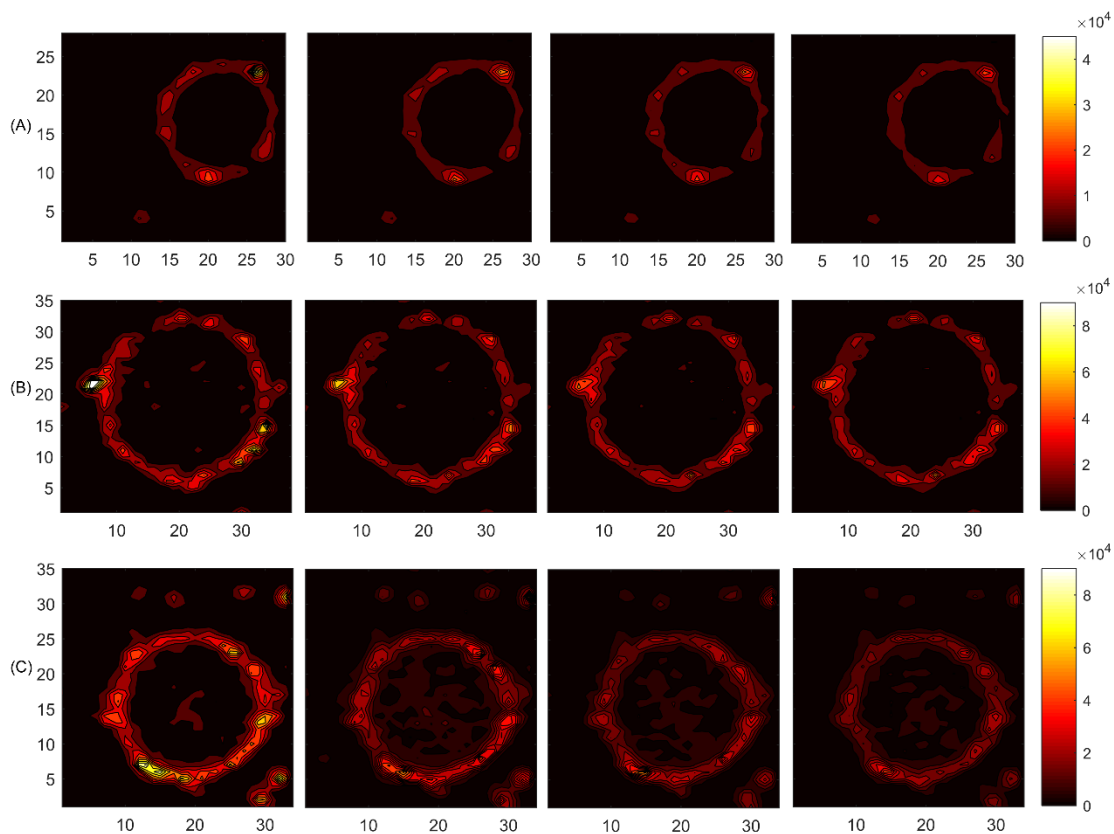


**Figure 5.18 | Reproducible iSERS imaging measurements by decreasing the laser power on cell samples with constant integration time per pixel assisted with EMCCD gain for the compensation of the signal loss: (A)** Laser power 2.32 mW, integration time 0.05 s, EMCCD gain 200; **(B)** Laser power 1.24 mW, integration time 0.05s, EMCCD gain 230; **(C)** Laser power 0.49 mW, integration time 0.05 s, EMCCD again 230. This figure originates from Wang et al., 2017a.

To check whether the integration time could be reduced further, two further sets of experiments were carried out. **Figure 5.18 (B) and (C)** show comparable imaging results by keeping the integration time constant at 50 ms and decreasing the laser power from 2.32 mW to 1.24 mW and 0.49 mW, respectively. Due to the reduction of the laser power, EMCCD gain with the maximum value of 230 was used in **Figure 5.18 (B) and (C)** to compensate the signal loss, respectively. However, **Figure 5.18 (B) and (C)** present the iSERS image with more interference of the fluorescence signal as a result of a lower signal to noise ratio when compared to **Figure 5.18 (A)**. Thus, for having an image with high reproducibility and contrast in short time, a laser power lower than ca

## RESULTS AND DISCUSSION

---

2.32 mW is not recommended for the fast analysis. In summary, a laser power of 2.32 mW, an integration time of 50 ms per pixel and a high EMCCD gain for imaging of HER2 antigen on breast cell slides could generate fast and reproducible results.

To have a better statistic understanding of the SERS intensity variation in the false-colour iSERS images, a further study of corresponding SERS spectra from each hyper-spectral data set image was performed (**Figure 5.19**), showing the mean value as well as the first standard deviation. For SERS spectra recorded under the laser power of 17.9 mW, the characteristic Raman signal of Raman reporter 4-NTB at  $1335\text{ cm}^{-1}$  almost disappeared in the second repeated run presented in **Figure 5.19 (A)**. This is consistent with the nearly complete pixel loss in **Figure 5.17 (A)**. In **Figure 5.19 (B)** and **(C)**, the intensity of the unique Raman band was recovered gradually in continual measurements on the same cell slide compared to **Figure 5.19 (A)**. Even though, the signal loss was still observed in a series of repeated iSERS experiments. In contrast, reproducible SERS spectra are yielded in **Figure 5.19 (D)** in four repeated measurements with the application of the laser power of 2.32 mW, integration time of 0.05 s and EMCCD gain of 200. This further clearly demonstrates the successful combination of the lower laser power, shorter integration time and the function of EMCCD gain to produce reproducible iSERS images. Under the current optimized condition, Raman reporters on the metallic surface will not lose their Raman activity but still exhibit the high SERS signal under the laser illumination, enabling the designed SERS probe in our study an ideal labelling agent to image HER2 expression on the single breast cell.

Since the reproducibility of iSERS imaging has been achieved, now we could answer the first question of how the heterogeneity of the SERS intensity is distributed across the single cell membrane in iSERS image. The abundance of HER2 protein located on the cell membrane could be directly calculated by this parameter via considering the relative standard deviation for the measurement on a single cell. The relative standard

## RESULTS AND DISCUSSION

---

deviation (RSD) for spectra in **Figure 5.19 (D)** is 83.4%, 72.1%, 65.3%, and 59.5% from left to right. It is concluded that these variations of the SERS intensity are reflections of HER2 protein heterogeneous expression across the cell membrane due to the biological variability.

It is worth mentioning that all iSERS imaging experiments in this study are based on confocal iSERS microscopy and the light is mainly collected from the confocal plane rather than the whole cell. It is expected that the RSD value will be decreased due to the increased sampling in case the true 3D Raman imaging on the entire cell is performed. In the current work, we have focused on fast and reproducible iSERS imaging experiments and the second question is more related in terms of the reproducibility of the iSERS microscopy for the repeated experiments on the same single breast cell. How does the average SERS intensity on the cell membrane vary across repeated experiments on the same cell? Then, we calculate the RSD value of only 3.74% for the four mean spectra in **Figure 5.19 (D)**, indicating an excellent reproducibility.

## RESULTS AND DISCUSSION

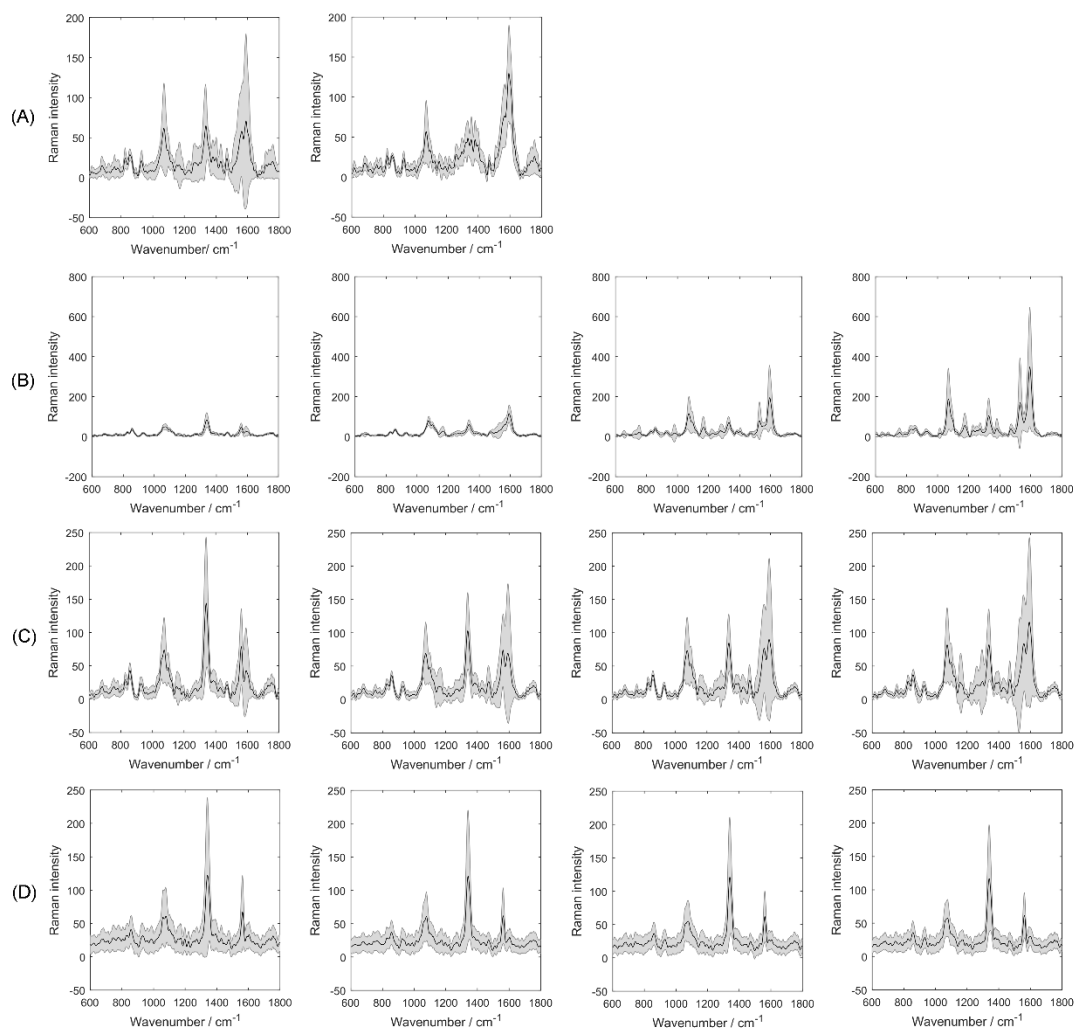


**Figure 5.19** | SERS spectra obtained with different laser powers and acquisition times per pixel in repeated iSERS imaging experiments on the same breast cell after baseline correction: (A) 17.9 mW, 0.1 s; (B) 10.3 mW, 0.2 s; (C) 4.7 mW, 0.4 s; (D) 2.32 mW, 0.05 s, EM gain 200. Reprinted from Wang et al., 2017a.

### 5.2.5 Conclusions and outlook

Herein, we present the first report on reproducible iSERS microscopy of the HER2 protein on the single breast cells in comparison with established techniques such as IHC and IF. Former iSERS studies were mainly focused on how to fabricate novel nanostructures as the SERS substrates to provide the reproducible SERS signals. In the present research, we have focused on the effect of instrumental conditions for the SERS imaging measurement, a crucial factor for achieving reproducible SERS signals.

## RESULTS AND DISCUSSION

---

The influence of the laser power intensity on the sample, integration time per pixel as well as the utilization of EMCCD gain was systematically investigated in repeated iSERS microscopic measurements on single breast cells to achieve fast and reproducible iSERS imaging. The modern EMCCD gain offers the capability of the signal amplification to reduce the overall acquisition time in Raman imaging measurements. In the current study, we have used the breast cancer cell slide at the single-cell level to analyze this aspect since it lays the fundamental basis for the quantitation for SERS analysis and is of great importance for the re-inspection of the specimen for pathologists in clinics. In the beginning, by changing the laser power intensity and the acquisition time per pixel, a series of repeated iSERS images were obtained for the same single breast cells overexpressing the breast cancer tumour marker human HER2. The combination of the overview by wide-field fluorescence microscopy with confocal Raman microscopic point mapping enables the rapid identification of areas of interest by fluorescence and then as the guide for the subsequent local analysis by iSERS microscopy. Initially, higher laser powers of 17.9 mW, 10.3 mW and 4.9 mW were used and non-reproducible iSERS imaging results were acquired as a result of the signal degradation. Then, lower laser powers of 2.32 mW, 1.24 mW and 0.49 mW with the EMCCD gain and constant acquisition time of 50 ms were applied. Highly reproducible iSERS images in four repeated experiments on the same single breast cancer cell were yielded under the laser power of 2.32 mW, integration time of 50 ms and EMCCD gain of 200.

In conclusion, based on the above optimized instrumental conditions, imaging of single breast cells could be achieved in few minutes with superior reproducibility which will open the new insights of the SERS imaging technique for future practical applications. Meanwhile, the negative control on the MCF cells further demonstrates the specificity of the AuNS-labelled primary antibodies.

### 5.3 Multi-colour iSERS microscopy on single breast cancer cells

#### 5.3.1 Motivation and background

Simultaneous differentiation of multiple target proteins on cells and tissues is challenging in biomedical diagnosis. In this work, we present results from six-colour/one-target iSERS imaging on single breast cancer cells. This method is a basic research for the realization of imaging multiple biomarkers on a single cell. Six different Raman reporter-labelled Au/Au core-satellites SERS nanotags were conjugated to anti-HER2 antibodies and used for the staining of single SkBr-3 cells on the glass slide.

**Figure 5.20** represents the schematic illustration of the synthesis of newly developed Au/Au core-satellites by Matthias König and the route of antibody conjugation. First, as shown in **Figure 5.20 (A)**, the positive charge was introduced to 50 nm super spherical AuNPs by the addition of MUTAB. Then, Raman reporters were added to exhibit the unique Raman fingerprint signal resulting in a co-adsorption of MUTAB and Raman reporters at a molar ratio of 3:1 on NPs surface. In this step, certain amount of adsorbed MUTAB molecules were replaced by Raman reporters due to the molecular competition. Then, citrate-capped 30 nm AuNPs with a negative potential were rapidly added and Au/Au core-satellites were immediately formed due to the kinetic interaction via the electrostatic adsorption. By changing the type of Raman reporters, herein six different Raman reporter-labelled Au/Au core-satellites could be facilely synthesized. Multiple hot spots could be generated which enable the substantial enhancement of Raman signal. Then, as shown in **Figure 5.20 (B)**, a layer of hetero PEG molecules was introduced onto Au/Au core-satellites for the covalent conjugation of antibodies and hydrophilic stabilization of the colloid solution via repeated ethylene glycol units. The thiol group on the one side of PEG molecules enables the strong attachment onto

## RESULTS AND DISCUSSION

AuNPs owing to the Au-S bond. The carboxylic group on the other terminus of PEG molecules allows the following conjugation of anti-HER2 antibodies onto NPs surface. This was realized by the amide reaction between amino residues of antibodies and carboxylic groups activated by EDC/sulfo-NHS coupling strategy. Meanwhile, the PEG layer could also improve the biocompatibility of Au/Au core-satellites and decrease the unspecific adsorption.

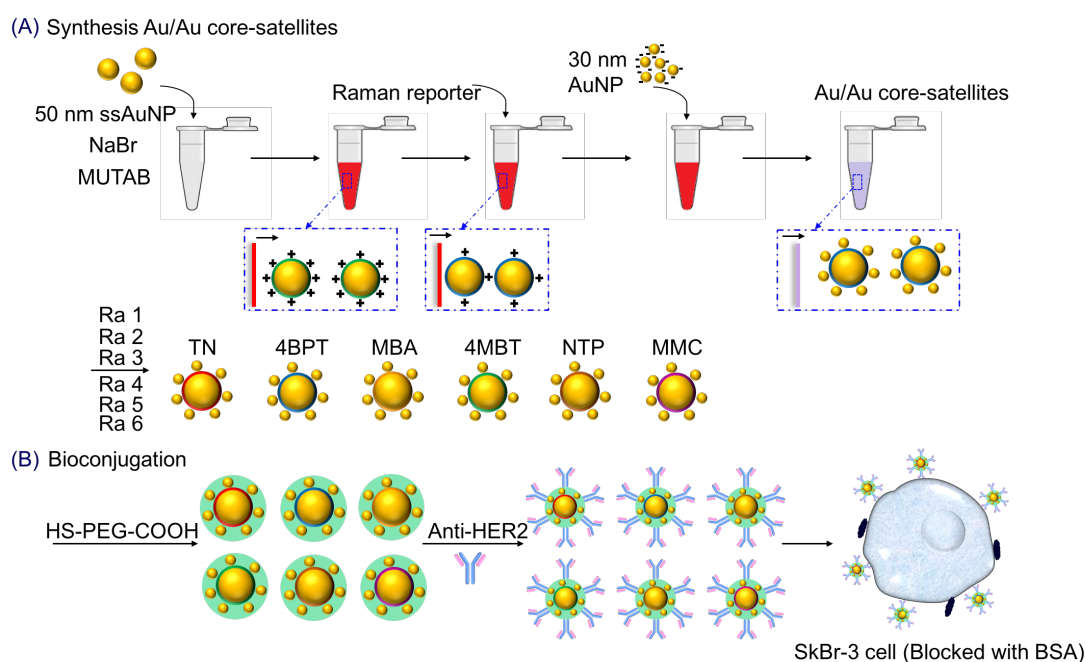


**Figure 5.20 | Schematic illustration of the multi-colour iSERS microscopy on the SkBr-3 cell slide. (A)** Synthesis of Raman reporter-labelled Au/Au core-satellites. **(B)** The covalent conjugation of anti-HER2 antibody onto six different Raman reporter-labelled and PEGylated-Au/Au core-satellites, respectively.

### 5.3.2 Characterization of SERS-labelled antibodies

After the synthesis of Au core, a transmission electronic microscope was used for the characterization of the shape and dispersity of NPs. **Figure 5.21 (A)** shows the image of Au spherical NPs with well-controlled shape and size. A mean diameter of 50 nm was obtained for Au core by a modified seed-mediated growth method. Due to the proportional relationship between Raman scattering intensity and the size of metallic

## RESULTS AND DISCUSSION

---

NPs, larger size of NPs will give rise to a higher Raman intensity. Meanwhile, core NPs with a larger size could provide more anchoring sites for the attachment of Au satellites owing to the larger surface area. On the other hand, the contrast of iSERS imaging of HER2 distribution on the single breast cell is in direct proportion to the number of bound Au/Au core-satellite conjugates. However, the increased size of Au core will lead to the overall size increase for Au/Au core-satellites assemblies and might induce a steric hindrance for the binding of more NPs onto the cell membrane. Based on above two main aspects, Au core with the average diameter of 50 nm was therefore selected for the achievement of the high Raman scattering intensity as well as the high targeting efficiency. Furthermore, we recorded the UV-vis extinction spectrum for the characterization of synthesized Au cores. As displayed in **Figure 5.21 (C)**, the plasmon peak centered at 538 nm was obtained for 50 nm AuNPs. This narrow plasmon band is an indication of no aggregation observed in the colloidal suspension. In general, monodisperse and quasi-spherical Au cores were yielded to ensure the reproducibility of SERS signal.

The next step was to synthesize Au satellites shown in **Figure 5.21 (B)**. An average size of 30 nm AuNPs were produced. The pathway for the synthesis of NPs was according to a seeded-growth method for the production of homogeneous Au/Au core-satellites. **Figure 5.21 (C)** also displays the extinction spectrum of Au satellites. The resonance plasmon peak was observed at 524 nm. For comparison, a red shift of the resonance peak was clearly detected with the increasing diameter of NPs. This matches the theory that the increasing size of particles results in a smaller plasma frequency and thereby induces a shift of the plasmon peak to a longer wavelength.

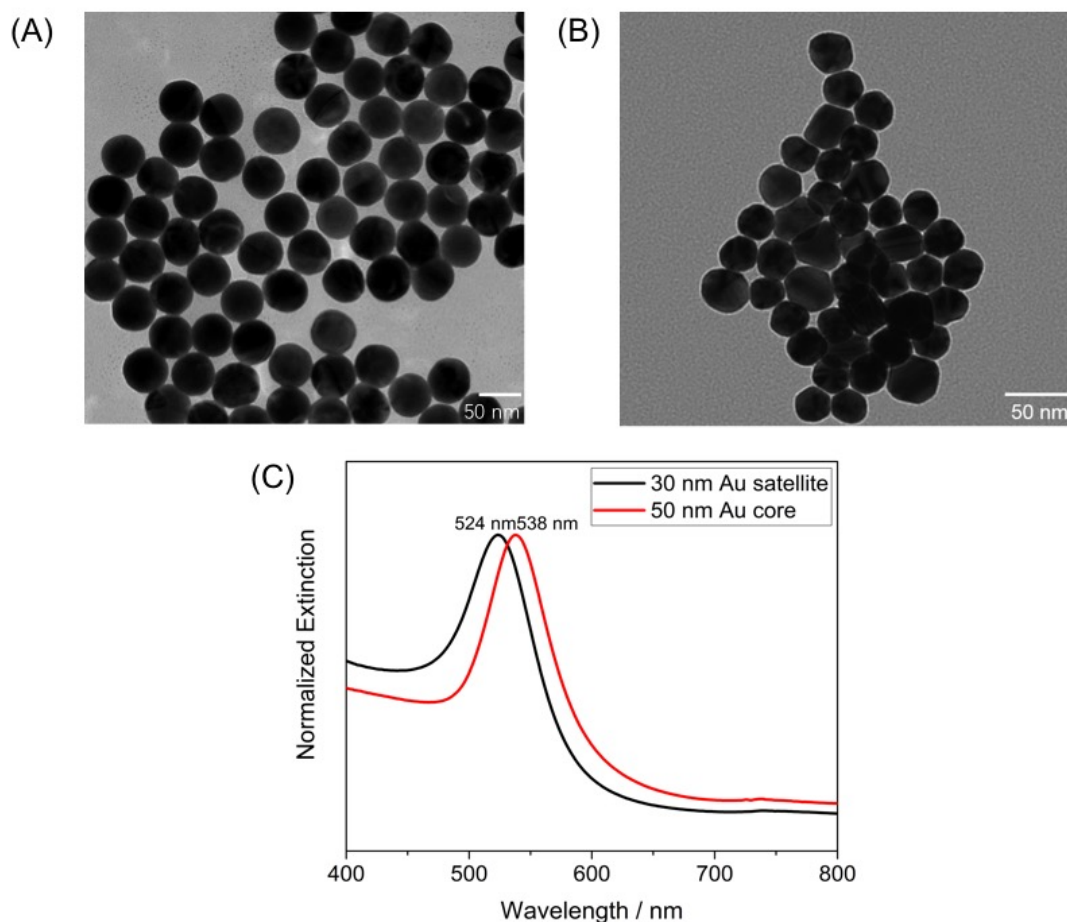


**Figure 5.21 | The characterization of the synthesized Au core and Au satellite by TEM and UV-vis absorption spectroscopy. (A)** TEM image of the super-spherical Au core. **(B)** TEM image of synthesized citrate-capped spherical AuNPs. **(C)** The normalized UV-vis extinction spectra of the super-spherical Au core and citrate-capped Au satellites in aqueous suspension.

A fabrication process of Au/Au core-satellites was then performed by the electrostatic assembly using Au core and Au satellites. As shown in **Figure 5.22**, the TEM image confirms that hetero nanocomposites were successfully fabricated. The designed assembly of Au/Au core-satellites exhibits a well-defined morphology and narrow size distribution.

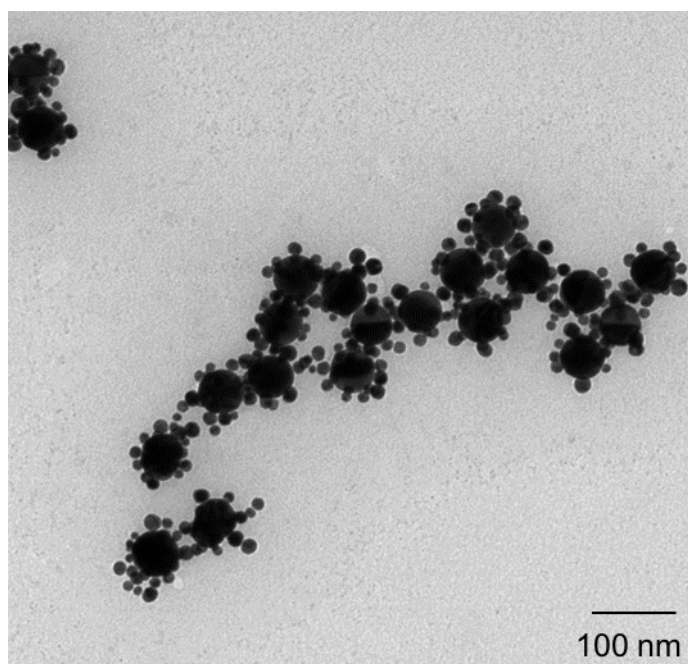


**Figure 5.22 | TEM image of synthesized Au/Au core-satellites.**

Then, UV-vis extinction spectra displayed in **Figure 5.23** were plotted for the comparison of the optical property of the synthesized Au core, Au satellite and Raman reporter-labelled Au/Au core-satellites. Herein, Raman reporter MMC was added as an example for the assembly of Au/Au core-satellites. The normalized extinction spectrum of Raman reporter-functionalized Au/Au core-satellites shows a plasmon peak at 530 nm due to the plasmonic mode of citrate-capped Au satellites. The appearance of an additional plasmon peak at ca. 660 nm is due to the plasmon coupling between the quasi spherical Au core and Au satellites. This further demonstrates the successful assembly of satellites onto the Au core in an ordered manner. Moreover, the newly presented plasmon peak at 660 nm matches the laser excitation wavelength of 633 nm to attain higher SERS enhancement. Compared with the plasmon peak of Au core and satellites, this red shift of the wavelength indicates the formation of larger-sized NPs. Furthermore, a broadening plasmon band of Au/Au core-satellites was observed owing to the aggregation of Au nanocomposites.

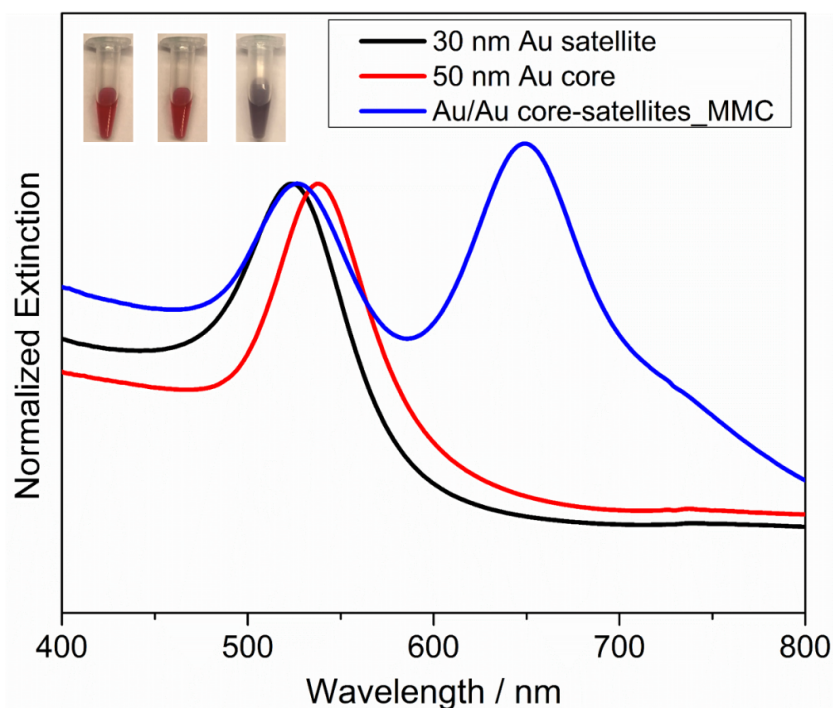


**Figure 5.23** | The UV-vis extinction spectra for the comparison of Au core, Au satellite and Raman reporter-labelled Au/Au core-satellites. The inset picture shows the colour of the suspension for each type of NP (from left to right: Au core, Au satellites, Au/Au core-satellites).

Besides, inset pictures present the colour change during the process of the assembly. The left and middle pictures show the red colour of the synthesized 50 nm Au core and 30 nm Au satellites, respectively. A homogenous suspension was obtained for both Au core and satellites. Then, after adding Au satellites onto the Au core surface, an immediate colour change was observed as shown in the inset picture (right). The purple colour of the colloid demonstrates the good dispersity of assembled Au/Au core-satellites.

To investigate the performance of SERS enhancement for fabricated Au/Au core-satellites, two further experiments were carried out. Here, we only used Raman reporter of NTP as an example to explore the signal variation. **Figure 5.24 (A)** presents the comparison of SERS intensity obtained from Raman reporter NTP-labelled Au/Au core-satellites and Raman reporter NTP-labelled super-spherical 50 nm Au core,

## RESULTS AND DISCUSSION

respectively. A remarkable signal enhancement was observed after the assembly of Au satellites onto the Au core surface. This is attributed to the strong intra-particle plasmonic coupling between satellites and the core particle. The local field is substantially amplified by the nanogap (hotspot). Therefore, Raman reporters located in hotspots could experience the tremendous SERS enhancement.

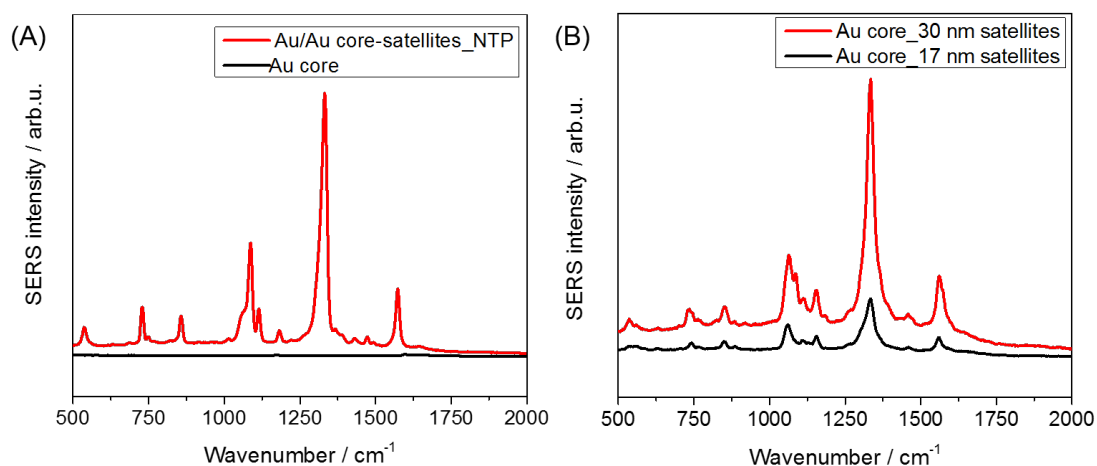


**Figure 5.24** | The comparison of SERS intensity obtained from: **(A)** NTP-labelled Au/Au core-satellites (Red) and the super-spherical 50 nm Au core (Black). **(B)** the assembly of 30 nm Au satellites (Red) and 17 nm Au satellites (Black) onto 50 nm Au core, respectively. Laser line of 633 nm, integration time of 10 s and 40× objective were applied for recording SERS spectra in three repeated measurements. The instrumental setup was calibrated before recording SERS spectra using the standard silicon wafer.

In addition, we also conducted similar experiments using other type of Raman reporters and similar SERS enhancements were obtained (data not shown here). Since we have demonstrated the monodispersity of synthesized Au/Au core-satellites, the achieved high SERS enhancement was not due to aggregated NPs. Thus, the composite of Au/Au core-satellites is a good candidate for SERS substrate when imaging of biomarkers in the biopsy.

On top of that, we notice that the size of satellites is a key factor for tuning the variation of the SERS signal. As shown in **Figure 5.24 (B)**, two SERS spectra were recorded

## RESULTS AND DISCUSSION

---

from 50 nm Au core assembled with 30 nm satellites and 17 nm satellites, respectively. The same concentration of Raman reporter NTP was added into the assemblies for two different sizes while keeping the incubation time constantly. A relative higher SERS signal was detected by assembling 30 nm satellites onto the 50 nm Au core. It is assumed that the gap distance is similar using two different sizes of satellites. However, 30 nm satellites are more favourable for plasmonic coupling to generate hotter spots. Therefore, the overall SERS signal enhancement for the assemblies using 30 nm satellites was much higher compared to 17 nm satellites. To obtain the high imaging contrast by iSERS on single breast cancer cells, larger SERS signal enhancement induced by the addition of 30 nm satellites was preferred.

The above demonstrated synthesis route developed by Matthias König provides a facile way for the high throughput of different Raman reporter-labelled Au/Au core-satellites. By simply changing the type of reporter molecules prior to the addition of satellites, a new SERS nanotag could be obtained. Organic molecules such as 4BPT, 4MBT, MBA, MMC, NTP and TN were selected in this work to exhibit the characteristic Raman spectrum for each SERS nanotag. Those molecules were used due to the comparative Raman cross section for the signal readout after a thorough SERS intensity test. Importantly, it is noticed that the incubation time for the resulting mixture was varied depending on the type of Raman reporters in order to prevent the aggregation. Meanwhile, an additional amount of 10  $\mu$ L 1.1 mM MUTAB was essential for the stabilization of NPs when adding Raman reporters.

For the attachment of Raman reporters onto Au core, each type of Raman reporters (4BPT, 4MBT, MBA, MMC) and MUTAB were added and incubated with Au core for 30 min under shaking, respectively. However, for NTP and TN, 5 min was enough to generate comparable SERS signal compared to other Raman reporters. A negative control experiment was carried out by incubating MBA with Au core without adding

## RESULTS AND DISCUSSION

MUTAB. A colorless colloid solution was obtained in 10 mins. Therefore, the further addition of MUTAB was essential for keeping the stability of colloids. Finally, a monodispersed- colloid solution of six different Raman reporter-labelled Au/Au core-satellites was yielded. TEM images are shown in **Figure 5.25**, indicating Au/Au core satellites were successfully obtained for six SERS nanotags.

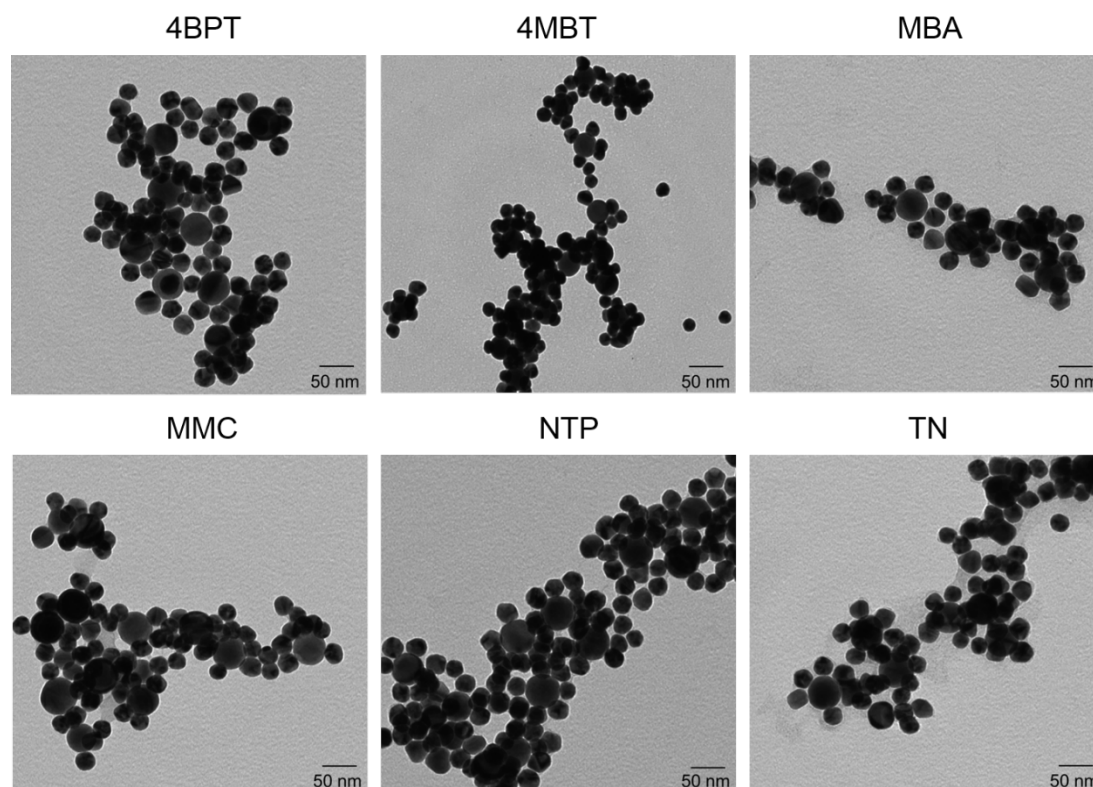


**Figure 5.25** | TEM images showing the assembly of Au/Au core-satellites comprising six different Raman reporters (4BPT, 4MBT, MBA, MMC, NTP and TN).

Then, UV-vis extinction spectra were recorded for the characterization of six Raman reporter-labelled Au/Au core-satellites. As displayed in **Figure 5.26**, MMC, NTP and MBA-labelled NPs exhibit similar extinction spectra. In contrast, the extinction spectra of 4MBT, TN and 4BPT-labelled NPs show a red shift of the plasmon resonance peak. It is speculated that Raman reporters have different affinities towards the surface of the

## RESULTS AND DISCUSSION

Au core resulting in a different refractive index of labelled-Au/Au core-satellites. Overall, the observed similar plasmonic mode of six SERS nanotags demonstrates the versatility of the developed synthesis method, which could be applied for the construction of various Raman-active labels with good dispersity.

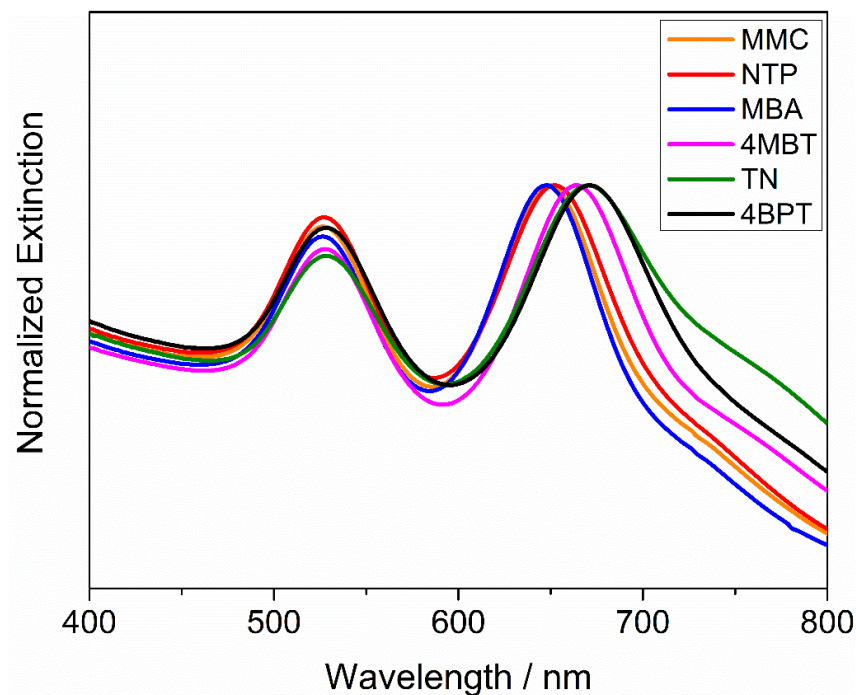


**Figure 5.26 | Normalized UV-vis extinction spectra of six different Raman reporter (MMC, NTP, MBA, 4MBT, TN, 4BPT)-labelled Au/Au core-satellites.**

Subsequently, the DLS measurement was employed for the size distribution. The given histograms in **Figure 5.27** represent the hydrodynamic size distribution of six different Raman reporter-labelled Au/Au core-satellites, respectively. A mean radius of 39.9 nm, 37.4 nm, 39.7 nm, 38.6 nm, 38.9 nm, and 37.8 nm was obtained for each SERS nanotag (NTP/4BPT/TN/4MBT/MMC/MBA), respectively. The most well-distributed particle size was attained from TN labelled-Au/Au core-satellites. The average radius size for overall SERS nanotags was around  $38.7 \pm 0.999$  nm in water suspension. This demonstrates the high monodispersity of synthesized SERS-active Au/Au core-satellites which could be further applied as superior substrates for producing the reproducible SERS signal.

## RESULTS AND DISCUSSION

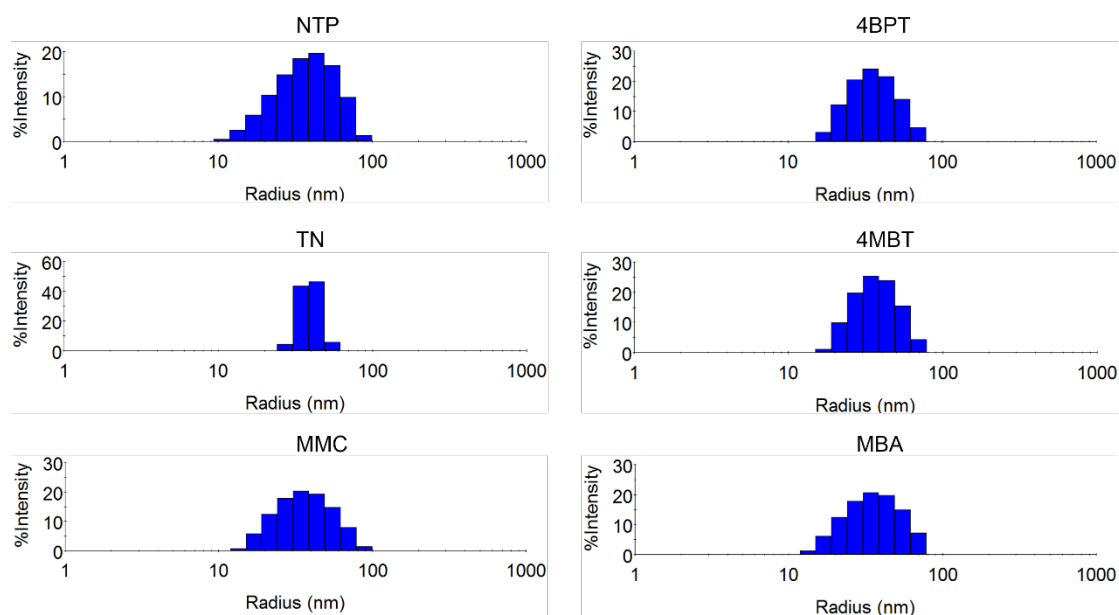


**Figure 5.27 | DLS performed for the characterization of the size distribution for six SERS nanotags.**

Then, the hetero-bifunctional PEG linker was employed to offer the bioconjugation as well as the reduction of the unspecific adsorption. However, it needs to be noticed that the addition of PEG will affect the SERS intensity of Raman reporter-labelled Au/Au core-satellites. To this end, SERS intensity of the colloid solution displayed in **Figure 5.28** was recorded before and after the encapsulation with PEG. The highlighted peak area in the spectrum of MMC was used to compare the variation of SERS intensity. It is observed that the signal intensity exhibits a slight decay after the incubation of PEG with the colloid solution. Thus, the surface density of PEG needs to be optimized before the conjugation of antibodies.

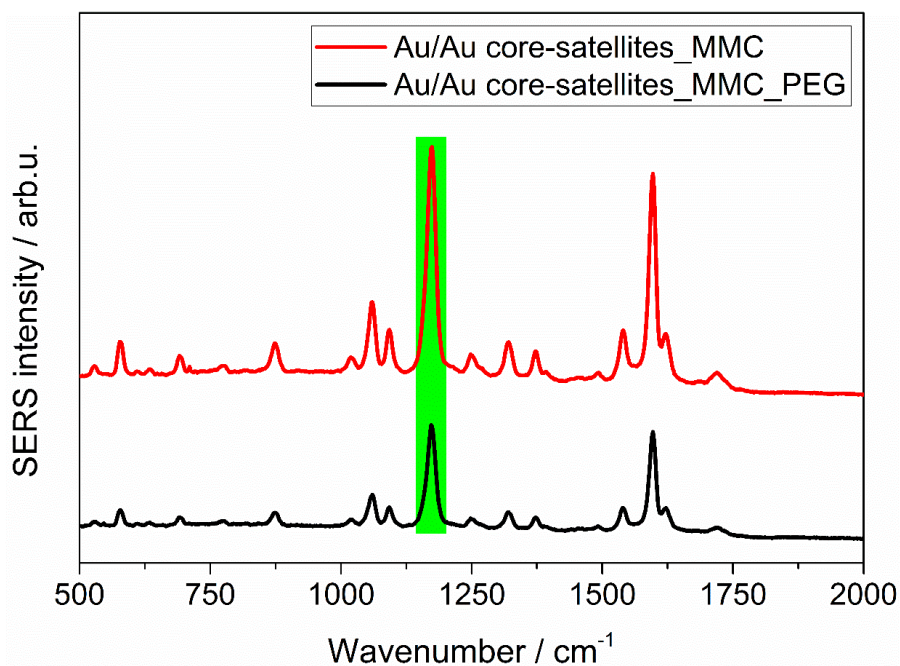


**Figure 5.28** | SERS spectra collected from the aqueous solution of MMC-labelled Au/Au core-satellites and MMC-labelled PEGylated-Au/Au core-satellites without base line correction, respectively. The characteristic vibrational band at 1170  $\text{cm}^{-1}$  was marked in the colour of fluorescent green. Laser line of 633 nm, integration time of 10 s and 40 $\times$  objective were applied for recording SERS spectra in three repeated measurements.

**Figure 5.29** displays the normalized SERS spectra after the chemisorption of six different Raman reporters of TN, MMC, 4BPT, 4MBT, MBA and NTP onto Au/Au core-satellites, respectively. The purpose of this work is to localize six SERS conjugates onto a single breast cancer cell and no quantitative distribution is required. Thus, to obtain six various SERS nanotags with comparable SERS intensity, the concentration and incubation time of Raman reporters are different. For instance, 3  $\mu\text{L}$  of 10 mM TN and NTP were added into the Au core respectively and each mixture was incubated for only 5 min at RT. To achieve similar SERS intensity, an extension of incubation time as well as an increase of concentration was applied for other reporters. Specifically, 5  $\mu\text{L}$  of 10 mM MMC, MBA, 4MBT and 4BPT were added respectively into the Au core and incubated together for 30 min at RT.

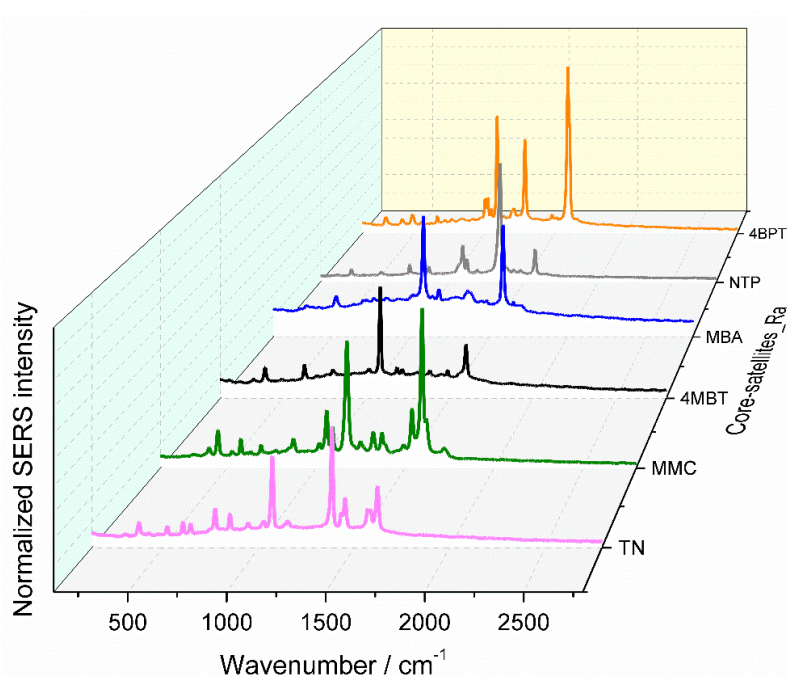


**Figure 5.29** | Normalized SERS spectra of six different Raman reporter-labelled Au/Au core-satellites ranging from TN, MMC, 4MBT, MBA, NTP to 4BPT, respectively. Each SERS nanotag is presented with a different colour. Laser line of 633 nm, integration time of 10 s and 40× objective were applied for recording SERS spectra in three repeated measurements.

As seen from the spectra, each SERS nanotag exhibits a distinctive vibrational mode. This demonstrates the designed six SERS nanotags could be used as an efficient tool for the multiplex imaging application. When above Raman reporter-labelled and anti-HER2-conjugated Au/Au core-satellites were added onto breast cell slides, the presence of a unique SERS signal could directly reveal the distribution of SERS conjugates on the whole cell membrane under the SERS mapping mode. In order to distinguish six SERS nanotags, a dominant vibrational band at 1384, 1170, 1335, 1080, 1286 and 1084  $\text{cm}^{-1}$  is assigned to TN, MMC, NTP, MBA, 4BPT and 4MBT, respectively. By detecting the corresponding signal of the assigned Raman band, a distribution of SERS nanotags on the cell membrane could be obtained.

## RESULTS AND DISCUSSION

---

Subsequently, a lateral flow strip was used to monitor the conjugation of anti-HER2 antibodies onto the surface of Au/Au core-satellites. The strip supplied from the company was pre-coated with PrG. PrG obtained from group G streptococci was initially applied for antibody purification in the field of biology (Grodzki and Berenstein, 2010). It can bind the Fc region of the antibody. The highly specific binding affinity towards IgG antibodies enables PrG a good IgG binding receptor. For the nanotechnology-based diagnosis, PrG used as a binding adaptor for non-covalent binding of antibody has already been reported (Salehi et al., 2014). Herein, the PrG-coated strip was used for the visualization of the presence of antibodies on NPs surface.

First, the positive control was performed shown in **Figure 5.30 (A)** using human IgG labelled-AuNPs which were provided together with the lateral flow strip. A remarkable red band was observed on the strip by the naked eye within 10 mins by immersing it into AuNPs-labelled IgG solution. The generated coloured band is due to the accumulation of AuNPs-labelled antibodies to the nitrocellulose membrane via the affinity against the pre-coated PrG.

Second, a negative control experiment was carried out by only adding PEGylated-Au/Au core-satellites onto the strip to check the unspecific binding. **Figure 5.30 (B)** displays no observed coloured band in the strip. This indicates PEGylated-NPs cannot adsorb onto to the strip non-specifically. Therefore, based on positive and negative control experiments, it is concluded that the PrG strip can be applied as an efficient and fast tool to monitor the conjugation of antibodies onto NPs.

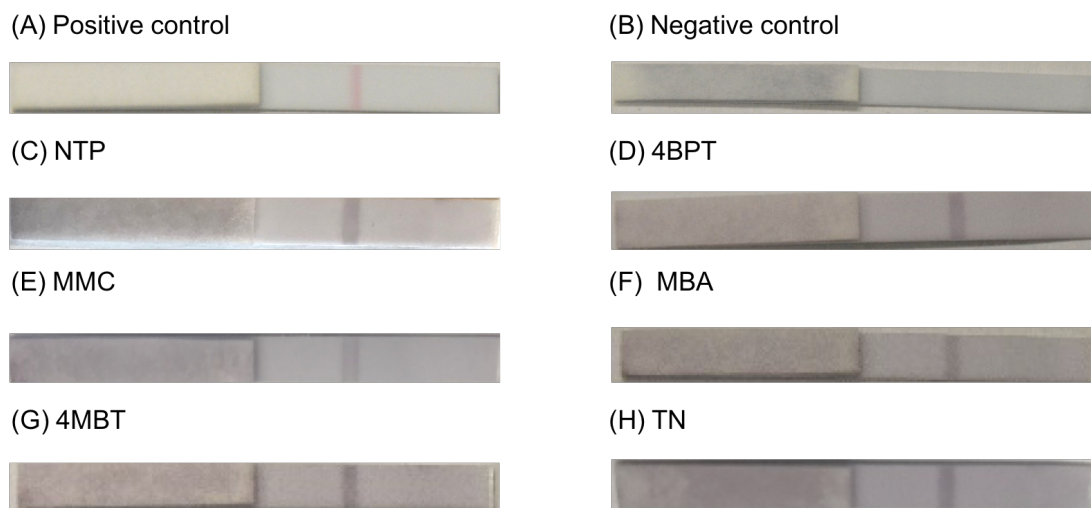


**Figure 5.30 | Lateral flow strip tests for checking the labelling process of antibody onto Au/Au core-satellites.** Photographs of PrG-coated strip after (A) the addition of AuNPs-labelled IgG antibodies as the positive control; (B) the addition of PEGylated-Au/Au core-satellites as the negative control; (C), (D), (E), (F), (G), (H) incubating with six different Raman reporter-labelled and anti-HER2-conjugated Au/Au core-satellites, respectively. All images were taken by a digital camera (Canon).

Finally, six different Raman reporter-labelled and anti-HER2-conjugated Au/Au core-satellites were added onto the PrG-coated strip, respectively and incubated for 10 min. The results are shown in **Figure 5.30** from (C) to (H). A purple band in each image was observed at a similar position as in the positive control, indicating the successful attachment of antibodies onto six different SERS conjugates.

Then, the size distribution of different Raman reporter-labelled and anti-HER2-conjugated Au/Au core-satellites was measured by DLS (**Figure 5.31**). A mean radius of 47.6 nm, 48.8 nm, 51.5 nm, 47.8 nm, 48.7 nm and 51.5 nm was obtained for NTP, 4BPT, TN, 4MBT, MMC and MBA-labelled and anti-HER2-conjugated PEGylated-Au/Au core-satellites, respectively. The overall average radius for six SERS conjugates was around  $49.3 \pm 1.76$  nm. An increase of 10.6 nm was obtained after the conjugation of antibodies onto the SERS nanotag, indicating the presence of antibodies on the NP

## RESULTS AND DISCUSSION

surface. The narrow size distribution also illustrates no occurrence of the aggregation during the multiple steps of labelling antibodies onto NPs.

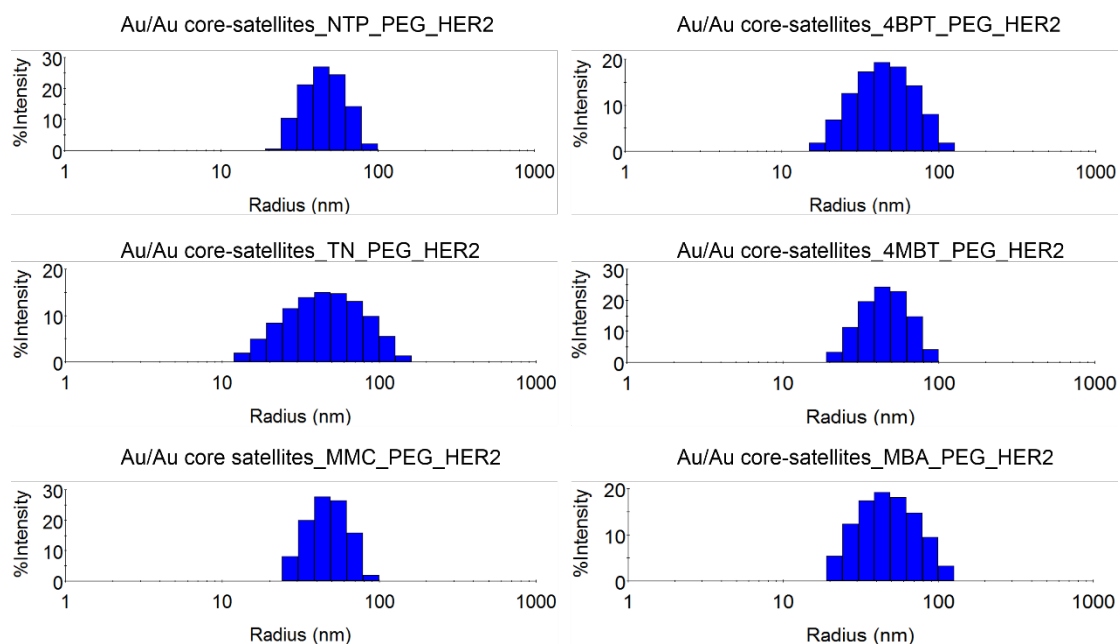


**Figure 5.31** | DLS performed for the characterization of the size distribution of NPs. The six different SERS nanotags were capped with a PEG layer and then conjugated with primary anti-HER2 antibodies.

### 5.3.3 Single-colour iSERS imaging

After confirming the presence of antibodies on the surface of six various SERS nanotags, they were incubated with the breast cancer cell slide (SkBr-3) for HER2 staining, respectively. SkBr-3, the cell line with high HER2 expression level, could be used as a model to check the staining performance of various rationally designed Au/Au core-satellite conjugates.

**Figure 5.32** shows false-colour iSERS images obtained from TN, 4BPT, MBA, 4MBT, NTP and MMC-labelled and anti-HER2-conjugated Au/Au core-satellites. As shown in **Figure 5.32 (A), (C), (E), (G), (I) and (K)**, an image of cell membrane with high spatial resolution recorded by Raman mapping was obtained for each SERS conjugate.

## RESULTS AND DISCUSSION

The short acquisition time allows the fast Raman imaging measurement could be obtained in few minutes. The false-colour iSERS image was plotted herein according to the intensity of the selected peak area in the fingerprint spectrum of each SERS nanotag centered at i.e.  $1384\text{ cm}^{-1}$  (TN),  $1286\text{ cm}^{-1}$  (4BPT),  $1080\text{ cm}^{-1}$  (MBA),  $1084\text{ cm}^{-1}$  (4MBT),  $1335\text{ cm}^{-1}$  (NTP) and  $1170\text{ cm}^{-1}$  (MMC). **Figure 5.32 (B), (D), (F), (H), (J) and (L)** display the mean spectra together with the first standard deviation calculated from the corresponding false-colour iSERS images. The inset on the top of spectra is the chemical formula of the applied Raman reporter. All selected Raman reporters comprising of the terminal thiol group have a strong attachment towards the Au surface via the thiol group.

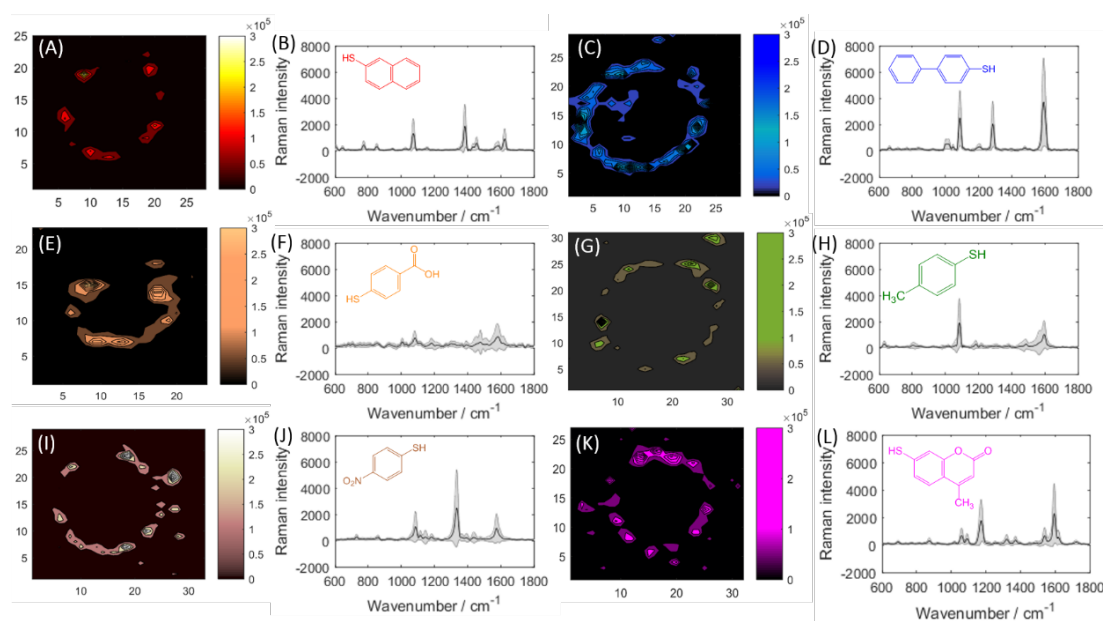


**Figure 5.32** | iSERS images acquired by the addition of six different Raman reporter-labelled and anti-HER2-conjugated Au/Au core-satellites onto the SkBr-3 cell slide. (A), (C), (E), (G), (I), and (K) are iSERS images of HER2 protein distribution on a single breast cell by TN, 4BPT, MBA, 4MBT, NTP and MMC-labelled and anti-HER2-conjugated Au/Au core-satellites, respectively. (B), (D), (F), (H), (J) and (L) are baseline-corrected SERS spectra obtained from the corresponding SERS false-colour image. (Laser line of 633 nm, 2.32 mW of the laser power, 0.05 s of

integration time and EMCCD gain of 200 were applied for the recording of the false-colour iSERS images.)

In all SERS images, only the cell membrane rather than the cytoplasm or the extracellular regions was stained with Au/Au core-satellites conjugates, demonstrating a high targeting selectivity using the current method. However, compared to the conventional IF imaging, iSERS imaging of HER2 distribution on the cell membrane by Au/Au core-satellites conjugates was not so homogenous as the image obtained in the section 5.2. This is possibly due to the heterogeneous SERS intensity of conjugates added onto cell slides. Particles are possibly aggregated at certain position of the cellular surface resulting in a higher SERS intensity. Moreover, the best quality of Raman mapping image was obtained by adding 4BPT-labelled SERS conjugates and almost the whole membrane was stained by NPs. Meanwhile, the plotted related mean spectra present the intense peak of multiple vibrational modes, implying the abundance of SERS conjugates adsorbed on the cell slide. The different staining profile in false-colour SERS images reveals the varied affinity of SERS conjugates towards the cellular surface as well as the varied expression level of HER2 protein on different cells.

Overall, imaging of HER2 distribution on the cell membrane was successfully performed by adding six different SERS conjugates onto SkBr-3 cell slides respectively, offering the possibility for the following localization of six conjugates in a single cell.

### 5.3.4 Negative control experiments

According to our previous research in section 5.1.4, NPs show the tendency of non-specific adsorption onto tissue sections. Therefore, it is essential to perform negative control experiments to evaluate the binding behaviour of NPs on cell slides.

**Figure 5.33** represents false-colour SERS images of HER2 expression on the cell slide by six different Raman reporter-labelled and anti-HER2-conjugated Au/Au core-

## RESULTS AND DISCUSSION

satellites. MCF-7 cell line was selected due to the nearly non-abundant expression of HER2. Thus, principally when the Raman reporter-labelled and anti-HER2-conjugated Au/Au core-satellites were applied onto the cell membrane, no SERS signal should be observed if unspecific binding does not occur. As shown in **Figure 5.33**, no obvious SERS signal was detected in plotted six false-colour SERS images, illustrating no or only minimal unspecific binding of NPs onto the cell slide.

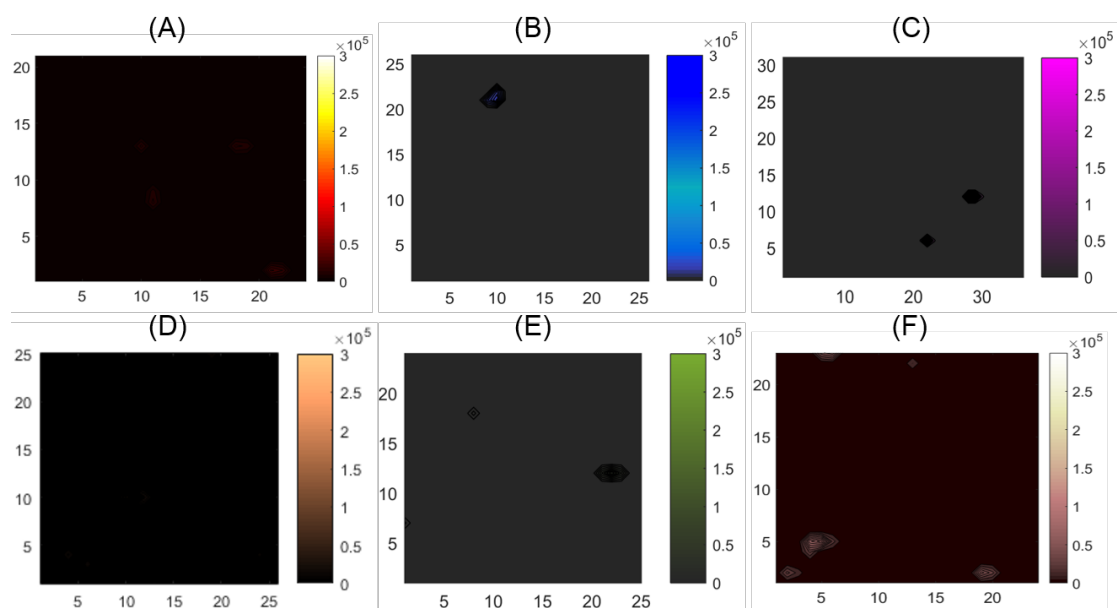


**Figure 5.33 | iSERS imaging of HER2 distribution on the single breast MCF-7 cell using six different Raman reporter-labelled and anti-HER2-conjugated Au/Au core-satellites: (A) TN; (B) 4BPT; (C) MMC; (D) 4MBA; (E) 4MBT; (F) NTP. (Laser line of 633 nm, 2.32 mW of the laser power, 0.05 s of integration time and EMCCD gain of 200 were applied for the recording of false-colour SERS images.)**

In section 5.1.4, we have noticed that HIER applied for FFPE tissue sections could lead to a significant unspecific adsorption of NPs onto tissue slides. Herein, for the cellular study, the antigen retrieval was not required while only the fixation was needed. Furthermore, the PEG layer around Au/Au core-satellites could substantially reduce the unspecific protein adsorption due to the highly hydrophilic ethylene glycol in the backbone of PEG molecules. It is reported the PEG chain could also decrease the

interactions of charged proteins and small molecules besides the formation of the interface layer between NPs and the solvent (Jokerst et al., 2011). Therefore, based on above results and analysis, we attribute the selective staining of HER2 protein on the cellular membrane of SkBr-3 cells in **Figure 5.32** to the specific binding of the designed Raman reporter-labelled and anti-HER2-conjugated Au/Au core-satellites.

### 5.3.5 Multi-colour iSERS imaging

**Figure 5.34** presents false-colour iSERS images via incubating a mixture of Raman reporter-labelled and anti-HER2-conjugated Au/Au core-satellites with SkBr-3 cell slides. All images were processed by cluster analysis and generally six clusters were used to analyze the recorded mapping image. The pixel appeared in the image was attributed to the presence of the signal from averaged spectra compared to the whole fingerprint spectrum of the corresponding Raman reporter. The eventual expectation of this work is to show the presence of six various Raman reporter-labelled conjugates on the cell membrane of a single breast cell. In order to achieve this aim, four preliminary experiments were performed by staining cell slides with a mixture of two, three, four and five Raman reporters sequentially. The combinations of Raman reporters were designed randomly.

As shown in **Figure 5.34 (A)**, a SERS image was obtained revealing the distribution of HER2 protein on the cell membrane with the applied mixture of MMC, 4BPT-labelled and anti-HER2-conjugated Au/Au core-satellites. An almost equivalent distribution of the two SERS conjugates was found on the cell membrane. This means that two different Raman reporter-labelled SERS conjugates could simultaneously bind onto the cell membrane without the significant competitiveness.

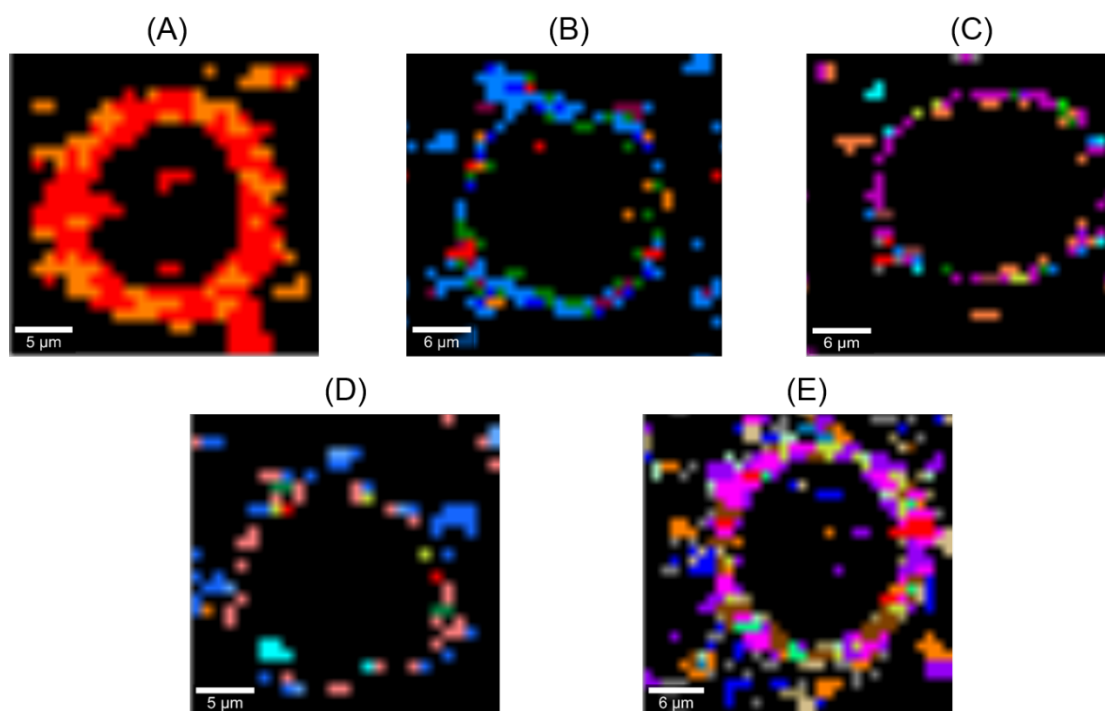


**Figure 5.34** | Localization of various combinations of Au/Au core-satellite-antibody conjugates onto a single breast cancer cell (SkBr-3) by iSERS. False-colour iSERS images acquired via the addition of Au/Au core-satellite conjugates labelled-by (A) MMC and 4BPT (B) MMC, 4BPT and TN (C) MMC, 4BPT, TN, NTP (D) MMC, 4BPT, TN, NTP, 4MBT and (E) MMC, 4BPT, TN, NTP, 4MBT, MBA, respectively. (Laser line of 633 nm, 2.32 mW of the laser power, 0.05 s of integration time and EMCCD gain of 200 were applied for the recording of the false-colour iSERS images.)

Then, MMC, 4BPT and TN labelled-Au/Au core-satellites were all conjugated with anti-HER2 antibodies and mixed prior to the incubation with the breast cell slide.

**Figure 5.34 (B)** shows the iSERS image with more coloured pixels in the cell membrane. Herein, every colour in the picture indicates one type of the presented SERS conjugate. Since three different SERS conjugates were applied onto the cell slide, SERS signal in one pixel could be attributed to various combinations of the three SERS conjugates. For instance, the acquired average SERS spectrum in one pixel is due to the signal from the three individual (MMC, 4BPT or TN) or the mixed (MMC and 4BPT, TN and 4BPT, MMC and TN or MMC, 4BPT and TN) SERS conjugates. Every

possibility of the combined mixture was shown in the false-colour image with a different coloured pixel.

Analogously, false-colour iSERS image of the single breast cell shown in **Figure 5.34 (C)** and **(D)** were recorded by the incubation with four (MMC, 4BPT, TN, NTP) and five (MMC, 4BPT, TN, NTP, 4MBT) Raman reporter-labelled and anti-HER2-conjugated Au/Au core-satellites, respectively. More coloured pixels were observed from two images which was consistent with the above illustrations for **Figure 5.34 (C)**. When more SERS conjugates were added onto the cell slides, more possibilities of the mixed SERS conjugates could be found in one pixel.

Finally, six mixed Raman reporter-labelled and anti-HER2-conjugated Au/Au core-satellites were added onto the cell slide and the mapping image obtained after cluster analysis is shown in **Figure 5.34 (E)**. It reveals that all the six SERS conjugates were bound onto the cell membrane successfully. In addition, a competitive adsorption of SERS-labelled antibodies onto the cell membrane was observed when adding a mixture of SERS conjugates comprising from two to six Raman reporter-labelled and anti-HER2-conjugated Au/Au core-satellites.

### 5.3.6 Conclusions and outlook

A new facile and versatile method for the synthesis of six spectrally distinct Raman reporter-labelled Au/Au core-satellites as SERS nanotags was devised. The new nanostructure developed by Matthias König was then employed for the six-colour/one-target iSERS imaging on single breast cancer cells.

Au/Au core-satellites were successfully fabricated via the electrostatic interaction between the positively-charged Au core and negatively-charged Au satellites. The TEM image of synthesized Au/Au core-satellites presents the homogenous morphology and

## RESULTS AND DISCUSSION

---

well-controlled size distribution. The rational design of the overall size around 80 nm in diameter provides plenty of anchoring sites for the adsorption of Raman reporters resulting in a substantial SERS signal. Meanwhile, more Au/Au core-satellites conjugates are allowed to bind onto cell slides due to the reduced steric hindrance from the suitable size dimension. On the other hand, SERS enhancement of the devised new nanocomposites was also investigated by comparing the SERS intensity of the Au core and Au/Au core-satellites. The results exhibit tremendous increase of SERS signal induced by Au/Au core-satellites owing to the multiple inter-particle gaps among the Au core and Au satellites. The gaps are hot spots which can significantly enhance the EM field and thereby additional several orders of magnitude SERS signal enhancement were observed. Furthermore, we also demonstrated that higher SERS intensity was produced by assembling larger satellites around the Au core.

The formation of PEG layer around Au/Au core-satellites offers functional groups for the antibody conjugation, the stability in physiochemical environment and the reduced unspecific adsorption. The plotted SERS spectra of six selected organic molecules indicate each SERS nanotag has a unique fingerprint SERS spectrum and can be differentiated from each other, showing a superior performance of the multiplexing capability. Subsequently, the proof of the antibody conjugation was explored through the use of PrG-coated lateral flow strips. Positive and negative control tests were preliminarily conducted to validate the accuracy of the proposed verification methods for antibody conjugation onto the surface of Au/Au core-satellites. The appearance of the band in the strip for all the six SERS conjugates confirmed the presence of anti-HER2 on the surface of nanocomposites. The imaging of HER2 distribution on the single breast cell (SkBr-3) was performed individually to check the targeting specificity. The resulting false-colour iSERS images present the extraordinary selectively staining of HER2 protein using six Au/Au core-satellites conjugates, which could be attributed

## RESULTS AND DISCUSSION

---

to the specific recognition of the antigen on the cell membrane by the labelled antibody. Then, negative staining experiments were carried out on the MCF-7 cell slide, which further demonstrated the specific binding of six SERS conjugates and revealed no existence of the non-specific binding from NPs.

The localization of six SERS conjugates on the single breast cell was realized via a step-by-step staining approach. The sequentially obtained SERS mapping images illustrate the possibility to target HER2 distribution on the single cell via different Raman reporters-labelled and spectrally differentiated-SERS conjugates. To the best of our knowledge, this is the first time to employ highly bright Au/Au core-satellites as SERS substrate which was labelled by six various Raman dyes for the localization of HER2 expression on the single cell by iSERS imaging.

In the future, detection of multiple biomarkers on cell or tissue samples would be considered. Taking advantage of the above devised assay, SERS probes of Au/Au core-satellites with the capability to recognize a variety of biomarkers either protein or DNA could be simply structured through the displacement of the superficial functional ligands with diverse antibodies or complementary DNA fragments. Overall, the established method for the construction of Au/Au core-satellite conjugates could be extended to an enormous scope of biomolecular applications.

### 5.4 Identification of single breast cancer cells among cell mixture

#### 5.4.1 Motivation and background

Recently, theranostic nanostructures (Ai et al., 2016; Choi et al., 2012; Lim et al., 2015; Shrestha et al., 2012) have attracted immense attention in the biomedical field. The multiplexing capability enables SERS imaging to become a superior tool compared with routine diagnostic methods such as IF or IHC staining. For IHC and IF, labour-intensive processing procedures and precise judgements by experienced professionals are required. In contrast, a simple and reliable imaging method for multi-biomarkers detection could be attained via the construction of different SERS-labelled antibodies.

In recent years, the metastasis cancer has increasingly attracted enormous attention in the field of cancer treatment. Many advanced techniques have been developed for the prognosis and treatment of cancer to improve the survival rate of patients. However, the recurrence of tumour cells in the near lymph nodes or distant organs could largely reduce the cure rate of patients, which are found after or even prior to the clinical therapy. Breast cancer, the leading cause for women mortality worldwide, has also been reported to transfer from the breast to other parts of the body such as bone marrow, termed as ‘stage IV’ breast cancer (Fields et al., 2007). If metastasized malignant cells are not screened out in the process of breast cancer diagnosis from the beginning, it might sleep for years and then invade the whole immune system leading to a severe incurable disease. The aforementioned cell migration from the primary tissue to other parts of the body poses a new threat for the cancer prognosis. Hence, the development of an efficient analytical method for the identification of tumour cells among cell mixture plays a crucial and decisive role in the detection of breast cancer.

Herein, a novel imaging strategy for the distinction of breast cancer cells among cell mixture is devised based on Au/Au core-satellites-labelled antibodies. In this work, to

mimic this model system, a limited number of breast cancer cells belonging to the SkBr-3 cell line were mixed with MNC cells. It is well known that SkBr-3 cell has much higher expression level of HER2 and EGFR while nearly no expression of CD45. MNC cells as critical components in the immune system generally possess a higher expression level of hematopoietic marker CD45 (leucocyte common antigen) while no expression of HER2 and EGFR. Thus, using multiple biomarkers of HER2 and EGFR for the characteristic identification of SkBr-3 cells would increase the recognition accuracy instead of only using HER2. On the basis of the phenotyping characterization of those surface markers, breast cancer cells could be discriminated among the cell mixture.

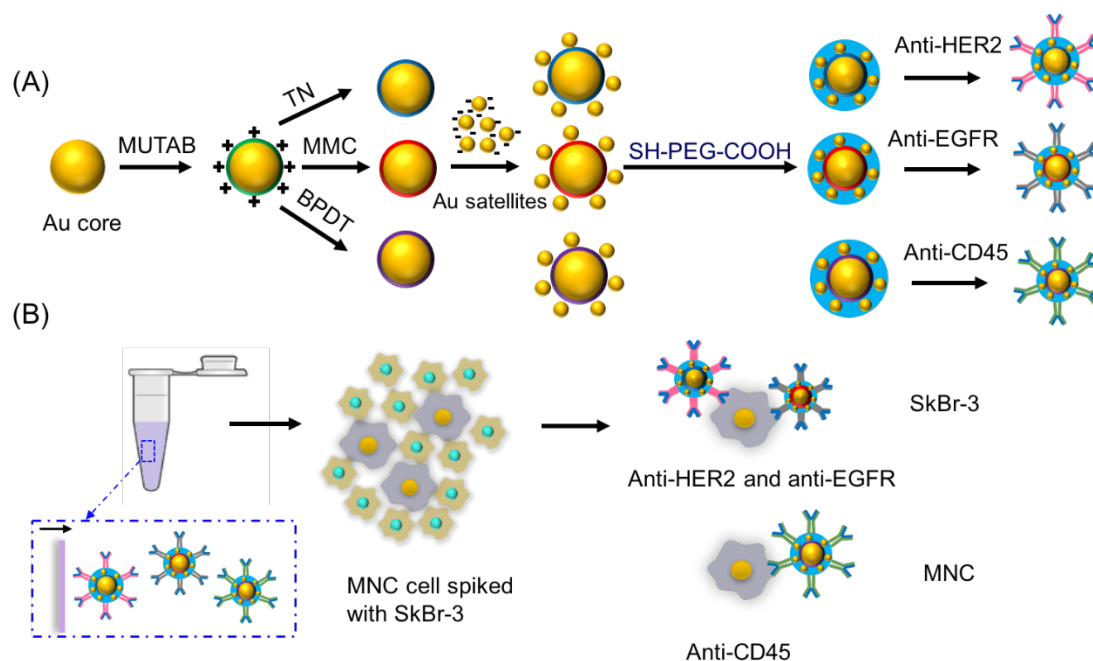


**Figure 5.35** | Schematic representation of the developed strategy for the identification of breast cancer cells in a mixture of cells. (A) The route of conjugating different antibodies (anti-HER2, anti-EGFR and anti-CD45) onto Au/Au core-satellites. (B) The addition of Au/Au core-satellites-labelled antibodies onto the mixed cell slide.

**Figure 5.35** shows the working principle of the designed method. First, a universal way for the conjugation of various antibodies onto NPs was established. The general method for the synthesis of Au/Au core-satellites is illustrated in section 4.2.2. Here, prior to

## RESULTS AND DISCUSSION

---

the assembly of Au satellites onto the Au core, three different Raman reporters of TN, MMC and BPDT were added into MUTAB-capped Au cores, respectively. Then, Au satellites were added to enhance SERS signal substantially owing to resulting hotspots. The thiolated-PEG carboxylic molecules were then incubated with three different SERS nanotags to introduce a hydrophilic interface. Subsequently, three different antibodies against HER2, EGFR and CD45, respectively, were mixed with TN, MMC and BPDT labelled-Au/Au core-satellites. After the attachment of antibodies, a mixed colloidal suspension containing three different SERS-antibody conjugates was dropped onto the cell slide which was mainly containing MNC cells and a spiked limited number of SkBr-3 cells. The stained cell slide was then examined by confocal Raman microscopy.

### 5.4.2 IF staining

Multiplex IF microscopy was firstly performed for imaging of HER2 and EGFR expression profiles on SkBr-3, MCF-7 and MNC cell slides, respectively. The significant fluorescence signal observed on the cell membrane in **Figure 5.36** exhibits the overexpression of HER2 and EGFR on SkBr-3 cells. In contrast, no fluorescence signal was found on the membrane of MCF-7 or MNC cells. Therefore, HER2 and EGFR could be used for the characterization of SkBr-3 cells.

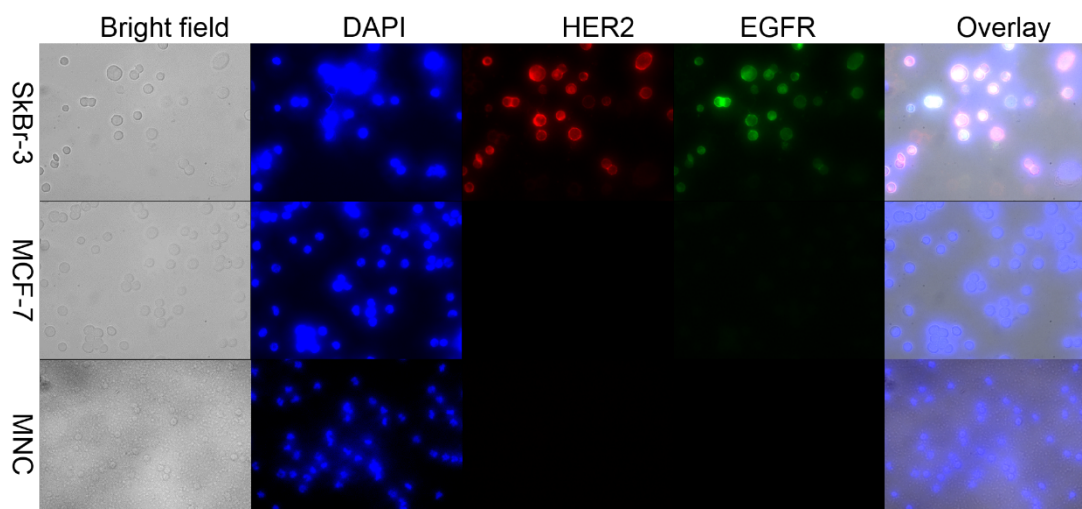


**Figure 5.36 | Images obtained by IF microscopy for HER2 and EGFR localization on SkBr-3, MCF-7 and MNC cell slides, respectively.**

Subsequently, the confirmation of CD45 expression was carried out on MNC, SkBr-3 and MCF-7 cell slides, respectively, as shown in **Figure 5.37**. Here, three slides were all stained with primary anti-CD45 antibody and then with Alexa647-labelled secondary antibody. As a result, obvious fluorescence signal was only detected on the cell membrane of MNC cell slide, indicating the abundant expression of CD45, while absent on SkBr-3 and MCF-7 cell slides. It demonstrates that the biomarker CD45 could be used as an indicator for the characterization of MNC cells.

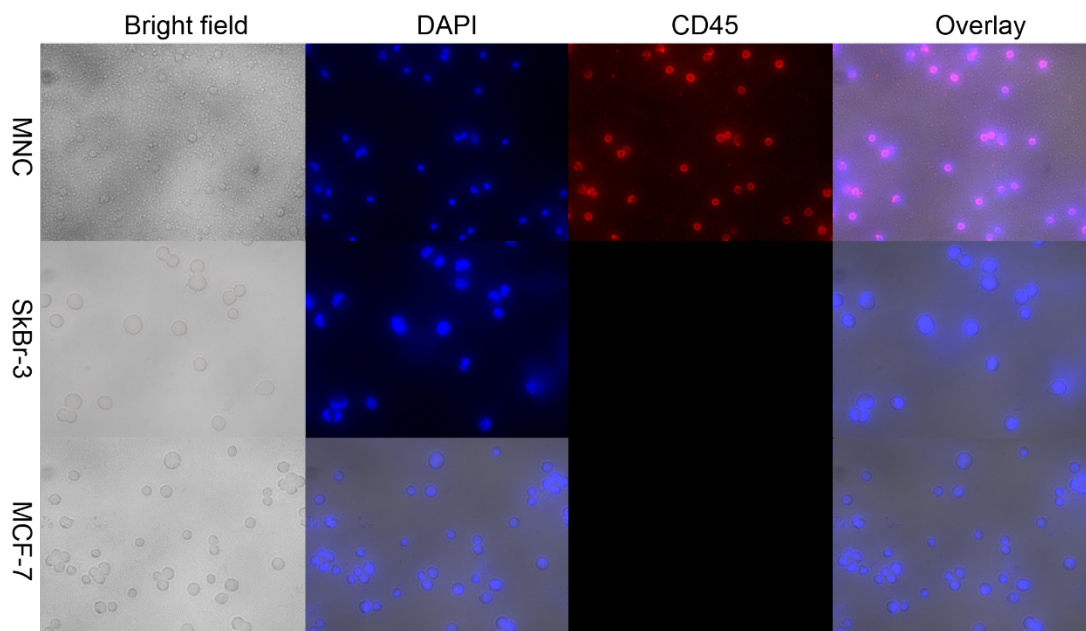


**Figure 5.37** | Images obtained by IF microscopy for the characterization of CD 45 expression on MNC, SkBr-3 and MCF-7 cell slides, respectively.

#### 5.4.3 SERS intensity characterization

To evaluate the multiplexing capability of rationally designed SERS probes, SERS spectra were recorded using Au/Au core-satellites-labelled BPDT, MMC and TN, respectively (**Figure 5.38**). Furthermore, SERS intensity was also recorded with a mixed suspension of above three SERS nanotags. The resulting SERS spectra exhibit a unique spectral fingerprint and no overlap of the three selected Raman reporters. The dominant vibrational band for each Raman dye was marked with light green ellipse, namely,  $1290\text{ cm}^{-1}$  for BPDT,  $1170\text{ cm}^{-1}$  for MMC and  $1384\text{ cm}^{-1}$  for TN.

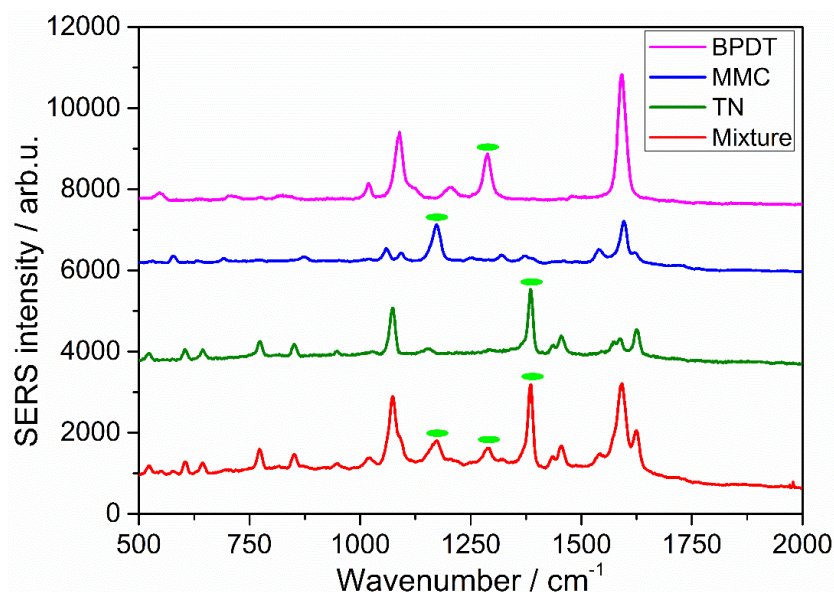


**Figure 5.38 | Average SERS spectra of Au/Au core/satellite particles with Raman reporters BPDT, MMC, TN and a mixture of the three.** Laser line of 633 nm, integration time of 10 s and 40× objective were applied for recording SERS spectra in three repeated measurements.

Moreover, the above mentioned significant vibrational bands for three Raman reporters were all present in the SERS spectrum of the mixed solution, indicating the appearance of the corresponding SERS peak which could reveal the presence of the corresponding Au/Au core-satellites labelled with Raman reporters. Consequently, the SERS intensity measurement provides persuasive results for the multiplexing performance of the applied SERS nanotags.

#### 5.4.4 Single-colour iSERS imaging of HER2, EGFR and CD45

The identification of breast cancer cells among the cell mixture is basically dependent on the successful staining of HER2/EGFR on SkBr-3 cell slide and CD45 on MNC cell slide, respectively. Therefore, in terms of the individual mapping study, SERS nanotag of Au/Au core-satellites labelled with BPDT, TN or MMC was fabricated in the first step, respectively. Then, they were conjugated with primary antibodies correspondingly

against CD45, HER2 and EGFR, respectively. iSERS imaging results are shown in **Figure 5.39**.

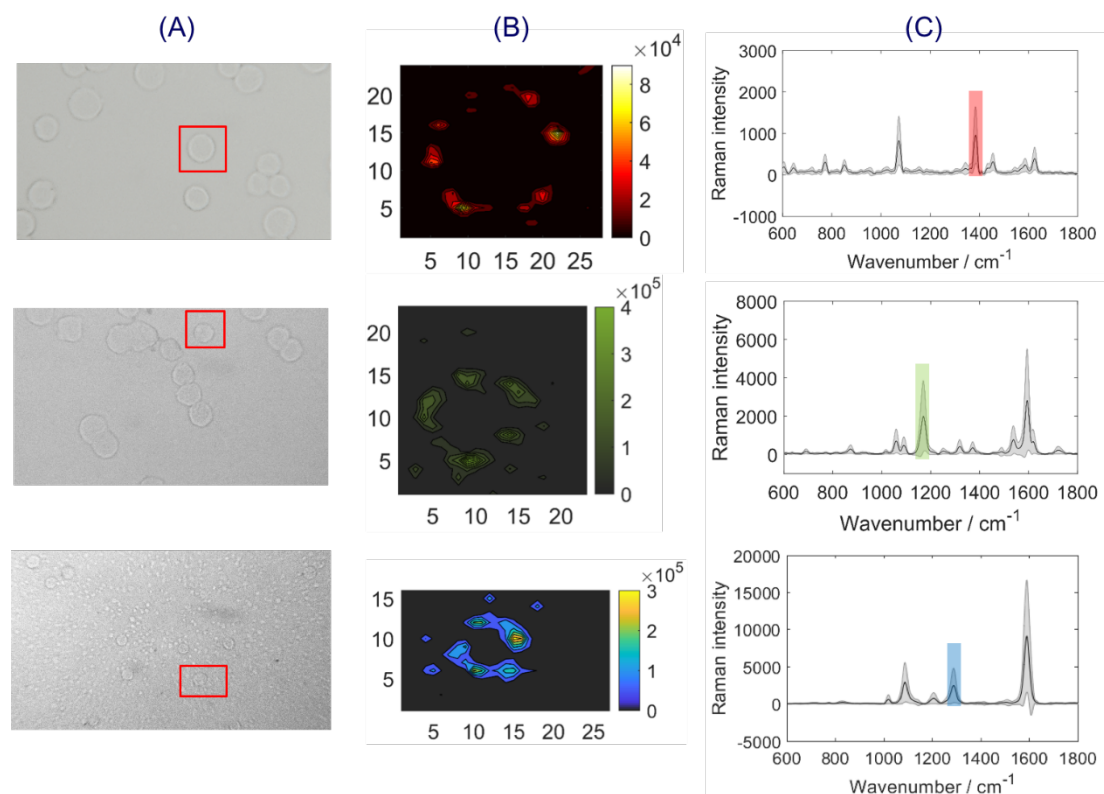


**Figure 5.39** | iSERS images of HER2, EGFR localization on SkBr-3 cell slide and CD45 localization on MNC cell slide. (A) Bright field images recorded on SkBr-3 (Top and middle) and MNC (bottom) cell slides. (B) False-colour SERS images of a single cell marked with a rectangular red box in the beside bright field image from top to bottom using Raman reporter-labelled and antibody conjugated-Au/Au core-satellites according to SERS intensity of the peak area centered at 1384  $\text{cm}^{-1}$  (anti-HER2/TN), 1170  $\text{cm}^{-1}$  (anti-EGFR/MMC) and 1290  $\text{cm}^{-1}$  (anti-CD45/BPDT), respectively. (C) Average SERS spectra with the standard deviation obtained from the corresponding false-colour SERS images. The dominant Raman peak was highlighted for each Raman reporter. Laser power of 2.3 mW, integration time of 50 ms, EMCCD gain of 200 and three repeated measurements with 40x objective were used for recording SERS mapping images.

The bright field images shown in **Figure 5.39** (A) clearly exhibit the morphology of breast cancer cells on the glass slide. A single cell in the image was chosen to perform

## RESULTS AND DISCUSSION

---

the Raman mapping measurement. The resulting false-colour SERS image of the single cell is presented in **Figure 5.39 (B)**. The obtained images were plotted according to the intensity of the characteristic Raman peak centered at  $1384\text{ cm}^{-1}$  (TN),  $1170\text{ cm}^{-1}$  (MMC) and  $1290\text{ cm}^{-1}$  (BPDT), targeting the localization of the biomarkers HER2, MMC and CD45, respectively. The results show that significant SERS signals were detected only on the cell membrane, indicating the high expression level of HER2/EGFR on SkBr-3 cells and CD45 on MNC cells. This is consistent with the reported study that HER2, EGFR and CD45 are surface receptors of the cell membrane. The imaging contrast in all false-colour SERS images is comparable to the standard IF image for the visualization of the antigen distribution within a cell. The pixels in false-colour images represent a relatively equal staining of surface biomarkers by SERS conjugates, revealing no heavy aggregation of the designed probes. Moreover, **Figure 5.39 (C)** exhibits the average spectra with the standard deviation calculated from the beside false-colour SERS image, showing a distinct characteristic vibrational Raman band with high signal to noise ratio for the three Raman dyes. This further demonstrates the high brightness of fabricated SERS conjugates.

### 5.4.5 Multi-colour iSERS imaging

Since the localization of HER2/EGFR on SkBr-3 cell slide, and CD45 on MNC cell slide via SERS conjugates has been achieved, respectively, we then applied mixture of anti-HER2/TN-, anti-EGFR/MMC- and anti-CD45/BPDT-labelled Au/Au core-satellites onto the glass slide to incubate with SkBr-3, MCF-7 and MNC cell slides successively.

**Figure 5.40** shows iSERS staining results. Three different SERS conjugates were synthesized preliminarily, then mixed together and finally added onto the glass slides. Herein, the two surface markers HER2 and EGFR were chosen for the characterization of SkBr-3 cells to improve the targeting accuracy. A SkBr-3 cell in **Figure 5.40 (A)** was randomly selected to perform Raman mapping. Images shown in **Figure 5.40 (B)**, **(C)** and **(D)** were plotted using SERS intensity of the dominant peak area at  $1384\text{ cm}^{-1}$  for TN,  $1170\text{ cm}^{-1}$  for MMC and  $1290\text{ cm}^{-1}$  for BPDT to target the expression level of HER2, EGFR and CD45 on SkBr-3 cell, respectively. The acquired mean spectra along with the standard deviation plotted from **Figure 5.40 (B)** and **(C)** are shown in **Figure 5.40 (E)** to give the detailed information of SERS intensity and presence of a certain SERS probe. **Figure 5.40 (B)** and **(C)** present a much higher brightness compared to **(D)**, indicating more anti-HER2/TN- as well as anti-MCF-7/MMC-labelled Au/Au core-satellites were bound onto SkBr-3 cells. The two ring-shaped images demonstrate a higher expression level of HER2 and EGFR on the membrane of the same cell, while for CD45 almost no expression was observed. Meanwhile, the designed SERS conjugates show high targeting affinity against antigens on the cell membrane, indicating the successful conjugation of antibodies of anti-HER2/anti-EGFR on the surface of Au/Au core-satellites.

## RESULTS AND DISCUSSION

Besides, it is worth to notice that there are some visual pixels shown in **Figure 5.40 (D)**. We presume this is due to the unspecific adsorption of the added NPs as a consequence of the cross-linking, which is inevitable for labelling antibodies onto NPs via EDC/sulfo-NHS coupling method. In addition, the unspecific binding can also be attributed to the gravity or electrostatic adsorption. The same circumstance was also observed in **Figure 5.40 (B)** and **(C)**. Therefore, unspecific pixels for CD45 staining in **Figure 5.40 (D)** could be neglected.

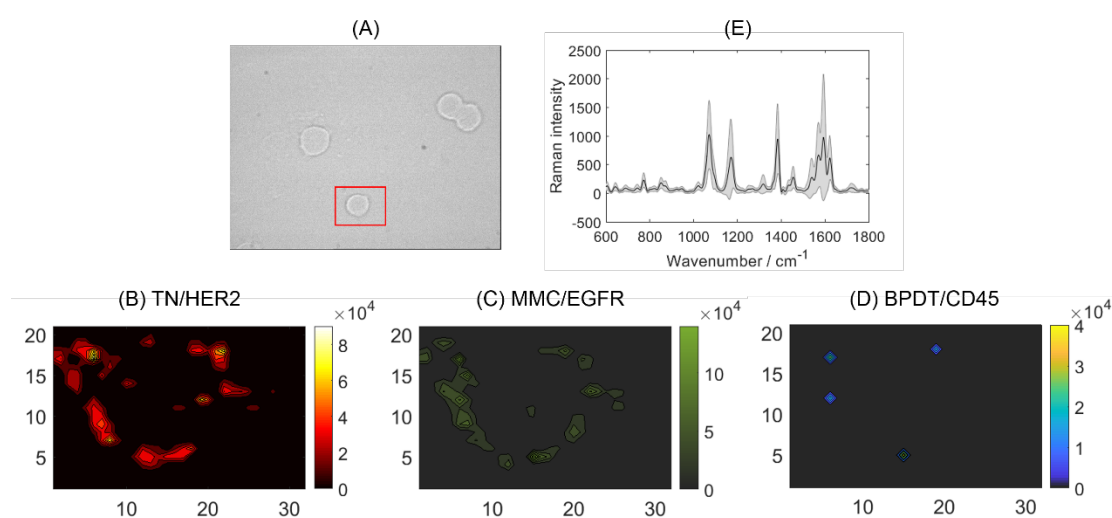


**Figure 5.40 | iSERS images of a breast cancer cell (SkBr-3) based on Raman reporter-labelled and antibody conjugated-Au/Au core-satellites. (A)** Bright field image of SkBr-3 cells on the glass slide under 40 $\times$  objective. **(B)**, **(C)** and **(D)** are false-colour SERS images obtained according to SERS intensity of the peak area centered at 1384  $\text{cm}^{-1}$  (TN), 1170  $\text{cm}^{-1}$  (MMC) and 1290  $\text{cm}^{-1}$  (BPDT) targeting HER2, EGFR and CD45, respectively. **(E)** Average SERS spectra with the standard deviation calculated from the false-colour SERS images of (B) and (C) for the selected cell in (A). Laser power of 2.3 mW, integration time of 50 ms, EMCCD gain of 200 and 40 $\times$  objective were used for SERS mapping images.

Subsequently, a mixture of SERS-antibody conjugates was incubated with the MNC cell slide. Similarly, the bright filed image was first taken to have an overview of cell distribution profile on the glass slide. Then, a single MNC cell marked with a red square

## RESULTS AND DISCUSSION

box in **Figure 5.41 (A)** was selected for performing the Raman imaging measurement. As expected, no obvious SERS signal was observed in **Figure 5.41 (B)** or **(C)** acquired on the basis of SERS intensity of the peak area for TN ( $1384\text{ cm}^{-1}$ ) and MMC ( $1170\text{ cm}^{-1}$ ) targeting HER2 and EGFR, respectively. It indicates that Au/Au core-satellites labelled with anti-HER2/TN and anti-EGFR/MMC could not attach onto the MNC cell. In comparison, **Figure 5.41 (D)** shows high SERS signal detected on the cell membrane. The presence of the SERS conjugate (anti-CD45/BPDT) was further confirmed by Raman spectra shown in **Figure 5.41 (E)**. Above imaging results illustrate that only Au/Au core-satellites labelled with anti-CD45/BPDT could be selectively bound onto the cell membrane of MNC cell through the specific immune reaction between attached antibodies and the antigen of CD45 while almost no binding was observed for the antigens EGFR and HER2.

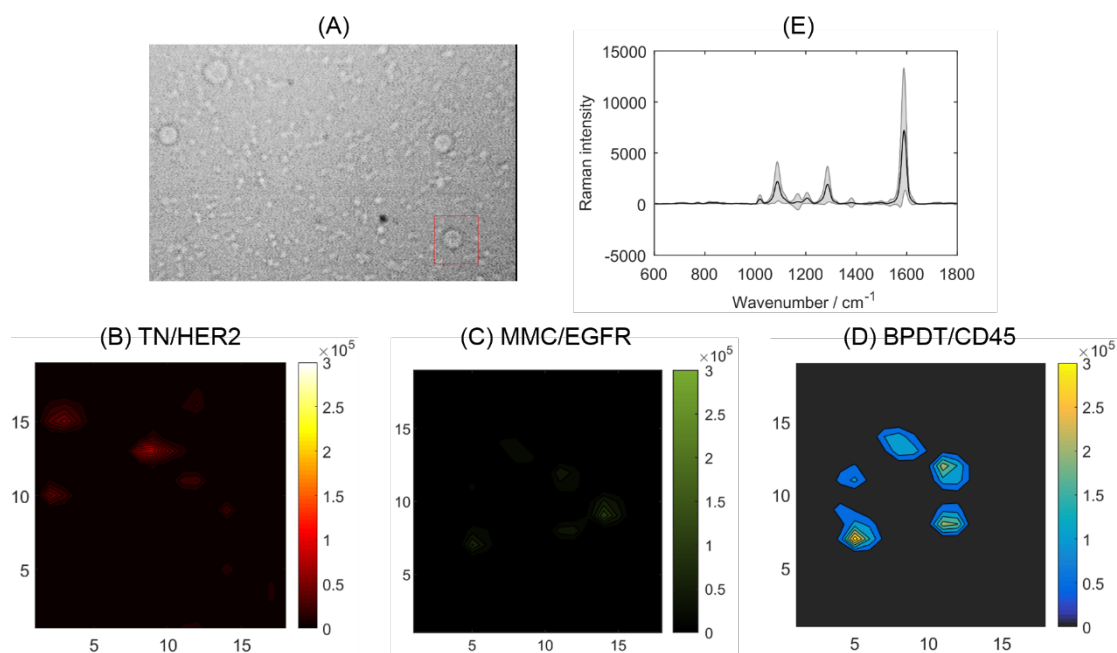


**Figure 5.41 | iSERS images of a MNC cell based on mixed Raman reporter-labelled and antibody conjugated-Au/Au core-satellites. (A)** Bright field image of MNC cells on the glass slide under  $40\times$  objective. **(B)**, **(C)** and **(D)** are the false colour SERS images obtained according to SERS intensity of the peak area centered at  $1290\text{ cm}^{-1}$  (BPDT),  $1384\text{ cm}^{-1}$  (TN),  $1170\text{ cm}^{-1}$  (MMC) targeting CD45, HER2 and EGFR,

## RESULTS AND DISCUSSION

respectively. **(E)** Average SERS spectra with the standard deviation calculated from the false-colour SERS image of **(D)** for the selected MNC cell in **(A)**. Laser power of 2.3 mW, integration time of 50 ms, EMCCD gain of 200 and 40× objective were used for SERS mapping.

The confirmation of the unique recognition on SkBr-3 and MNC cell slides has been successfully attained for targeted antigens of HER2/EGFR (**Figure 5.40**) and CD45 (**Figure 5.41**), respectively. However, it is also essential to conduct negative control experiments under the same conditions to verify the specificity of the developed assay. **Figure 5.42** shows iSERS images as well as the spectral analysis of a single MCF-7 breast cell without the expression of all three antigens, HER2, EGFR or CD45, on the cell membrane.

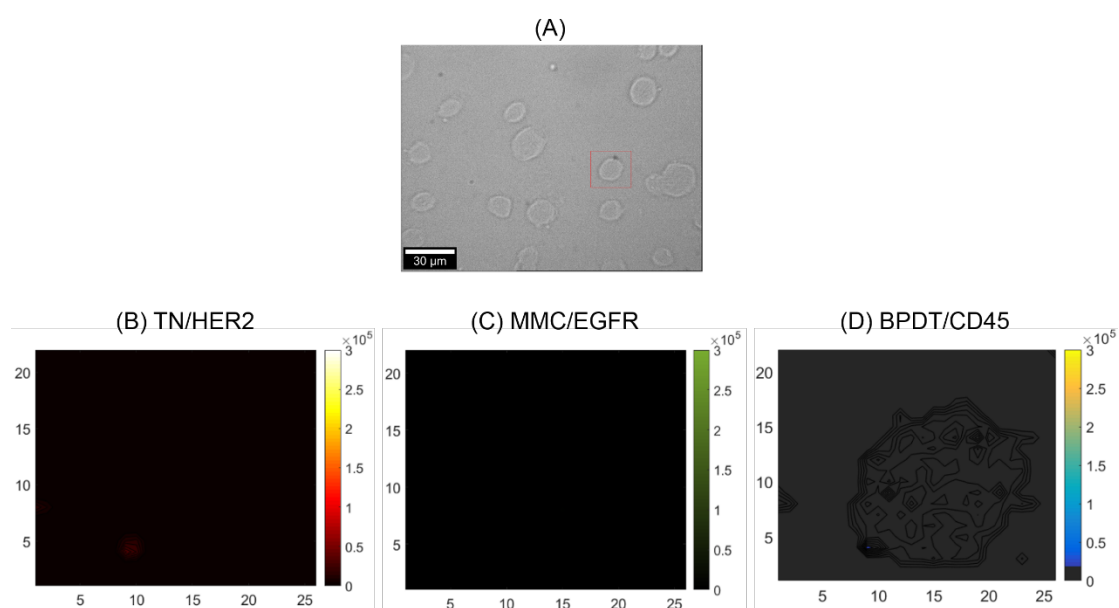


**Figure 5.42** | iSERS images of a MCF-7 cell based on mixed Raman reporter-labelled and antibody conjugated-Au/Au core-satellites. **(A)** Bright field image of MCF-7 cells on the glass slide with 40× objective. **(B)**, **(C)** and **(D)** are the false colour SERS images obtained according to SERS intensity of the peak area centered at  $1384\text{ cm}^{-1}$  (TN),  $1170\text{ cm}^{-1}$  (MMC) and  $1290\text{ cm}^{-1}$  (BPDT) targeting HER2, EGFR and CD45, respectively. Laser power of 2.3 mW, integration time of 50 ms, EMCCD gain of 200 and with 40× objective were used for SERS mapping images.

**Figure 5.42 (B), (C) and (D)** presents false-colour SERS images of a MCF-7 cell generated with the same method in **Figure 5.40** and **Figure 5.41** for the localization of HER2, EGFR and CD45, respectively. Nearly no pixel was observed on the cell membrane which matches the expression profile of the three biomarkers for MCF-7 cells, indicating the mixed SERS-antibody conjugates could not bind onto the membrane of MCF-7 cells. Overall, above negative control results demonstrate that the mixed NPs are not capable to attach onto the cells, exhibiting the high specificity of SERS conjugates.

The MNC cell slide with a mixture of  $0.1 \times 10^6$  cells and 50 spiked SkBr-3 cells was used to incubate with the mixed colloid containing Au/Au core-satellites labelled with anti-HER2/TN, anti-EGFR/MMC and anti-CD45/BPDT. Raman imaging results are displayed in **Figure 5.43**. First of all, the bright field image was obtained as shown in **Figure 5.43 (A)** and the cell marked with a blue rectangular box was selected for performing Raman mapping. The acquired false-colour SERS images in **Figure 5.43 (B)** from left to right were plotted via SERS intensity of the peak area at  $1384 \text{ cm}^{-1}$  (TN),  $1170 \text{ cm}^{-1}$  (MMC) and  $1290 \text{ cm}^{-1}$  (BPDT), respectively. In the left and middle images, bright ring-shaped patterns were observed, indicating the high abundance of NPs attached on the membrane of SkBr-3 cells, which is attributed to the high expression level of HER2 as well as EGFR. While for the right image, no evident ring-shaped image was obtained, illustrating no accumulation of Au/Au core-satellites labelled anti-CD45/BPDT on the cell membrane. We have already demonstrated the extraordinary targeting specificity towards the antigens of HER2, EGFR and CD45 with the three different SERS conjugates on individual SkBr-3, MNC and MCF-7 cell slides. As a consequence, given the presence of the antigens HER2 and EGFR on the randomly selected cell marked with a blue box, we presume this cell is one of the spiked SkBr-3 cells.

## RESULTS AND DISCUSSION

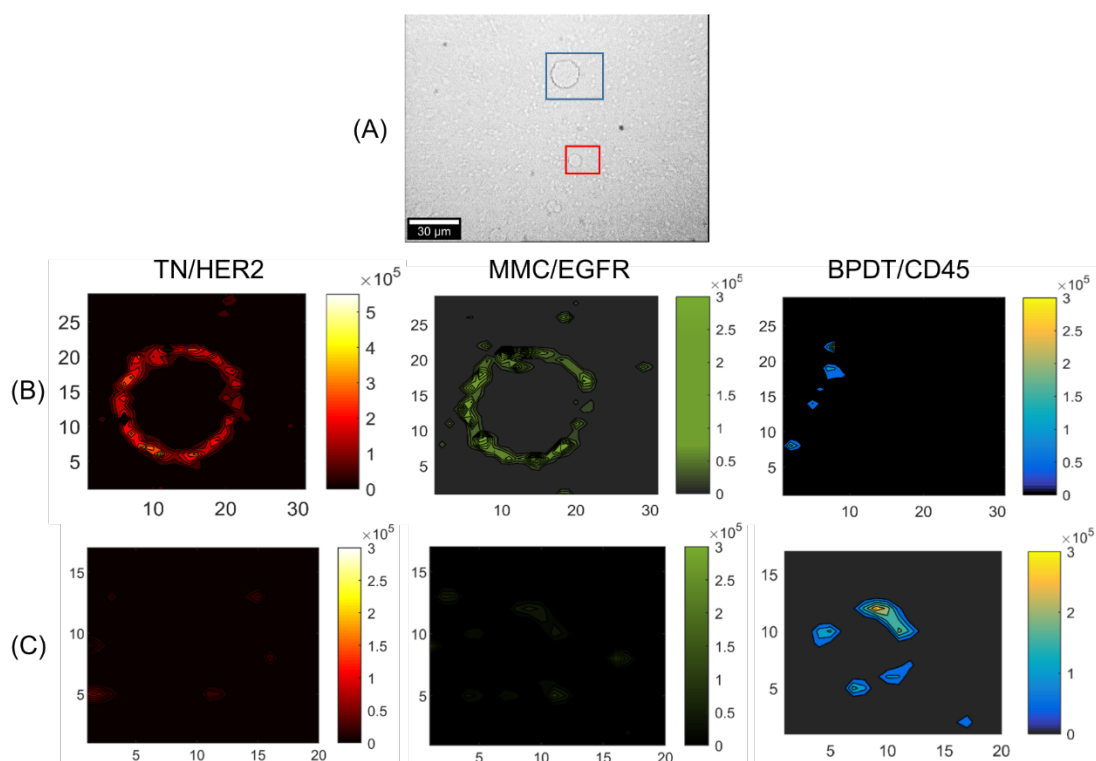


**Figure 5.43 | Identification of breast cancer cells among the cell mixture using mixed Raman reporter-labelled and antibody conjugated-Au/Au core-satellites.** (A) Bright field image recorded with 40× objective. False-colour SERS images from left to right shown in (B) and (C) were obtained according to SERS intensity of the peak area centered at  $1384\text{ cm}^{-1}$  (TN),  $1170\text{ cm}^{-1}$  (MMC) and  $1290\text{ cm}^{-1}$  (BPDT) targeting HER2, EGFR and CD45 for the cell marked with a blue rectangular box and red rectangular box, respectively. Laser power of 2.3 mW, integration time of 50 ms, EMCCD gain of 200 and 40× objective were used for SERS mapping images.

On the other hand, a red rectangular box in **Figure 5.43 (A)** was chosen for the Raman mapping measurement under same conditions as the cell marked with the blue box. **Figure 5.43 (C)** was obtained following the same plotting method for **Figure 5.43 (B)**. The right false-colour SERS image presents the signal detected only on the cell membrane showing the presence of Au/Au core-satellite-labelled anti-CD45/BPDT antibodies. In contrast, almost no signal was observed in the middle and right images indicating the absence of Au/Au core-satellite-labelled anti-HER2/TN or anti-

EGFR/MMC antibodies. Based on the above analysis, it is proposed that this selected cell is a MNC.

Bodelon et al. have demonstrated the possibility for simultaneous imaging of three markers on different cells using gold octahedral-labelled antibodies as the SERS probe (Bodelon et al., 2015). The imaging contrast in SERS images still needs to be improved and SERS imaging of mixed cells was not shown in that work. As a proof of concept study, the presented imaging results illustrate the capability of the developed assay for the precise identification of breast cancer cells among the cell mixture by simply applying mixed SERS conjugates onto the slide composed of a mixture of cells.

The imaging of a single cell via iSERS herein was obtained in several minutes due to the high SERS signal brightness of assembled Au/Au core-satellites. Under a single laser excitation, three different SERS images with high spatial resolution showing the localization of three various antigens could be simultaneously generated. This avoids the use of the fluorescence dye-labelled secondary antibodies in the conventional IF microscopy.

### **5.4.6 Conclusions and outlook**

We have investigated instrumental conditions for obtaining the optimal imaging result for a single breast cell in section 5.2 and demonstrated the superior multiplexing probability through the use of highly SERS-active Au/Au core-satellites in section 5.3. Given such fundamental research, in this section we designed a new SERS imaging technique for the identification of breast cancer cells within MNC cells via various Au/Au core-satellite-labelled antibodies for the first time.

Standard multiplexed IF was conducted as the first step for the verification of the antigen expression level on different cell slides, namely SkBr-3, MCF-7 and MNC cell

## RESULTS AND DISCUSSION

---

slide, as well as the immuno-activity of purchased antibodies. The biomarkers of HER2/EGFR and CD45 were selected for the phenotyping of the SkBr-3 and MNC cell lines, respectively. Multiple markers investigated herein for SkBr-3 cell line are aimed at increasing the discriminating efficiency. In fluorescence images, DAPI staining shows the localization of the cell nucleus and bright fluorescence signal found around indicates the high expression level of a certain protein on the cell membrane. As a result, it is distinctive that HER2 and EGFR are extensively expressed on the membrane of SkBr-3 cell line while no expression of CD45 is observed. On the contrary, bright fluorescent signal detected around the MNC cell represents the abundance of the CD45 while the absence of HER2 or EGFR. All above-mentioned results illustrate the excellent targeting specificity of selected SERS-labelled antibodies and simultaneously reveal the expression profile of three antigens on different cell lines.

Then, each SERS nanotag (TN/ MMC/BPDT) presents a unique SERS signature, which is the fundamental condition for the multiple recognition when incubating the mixed SERS labelled-antibody conjugates with cell slides. Furthermore, the high SERS signal observed in single-colour SERS images exhibits the high expression level of the three biomarkers on cell membrane of different cell lines. When the mixed three SERS conjugates were added onto cell slides of each cell line (SkBr-3/MCF-7/MNC), recorded false-colour SERS images show the same expression level of every biomarker as in the standard IF. The identification of breast cancer cells among the cell mixture was finally achieved, indicating the developed method could be employed as the potential imaging technique in the future for the diagnosis of cancer metastasis.

The superb multiplexing probability of SERS conjugates with low cost and the facile fabrication render iSERS microscopy widespread biomedical applications. For instance, in lateral flow assay, it could increase the detection sensitivity and allow the visualization of multiple analytes via SERS conjugates on the test band position (Liu et

## RESULTS AND DISCUSSION

---

al., 2017a; Zhang et al., 2018). With the combination of magnetic particles, iSERS has shown the excellent detection for CTC cells by a simple pull-down procedure (Sha et al., 2008; Shi et al., 2014; Sun et al., 2015) to separate cancer cells from the complex biological environment. Furthermore, applications of iSERS could also be expanded to single nucleotide polymorphism detection (Ngo et al., 2016), drug discovery and *in-vivo* imaging for the tumour screening.

### **6 Summary**

In this work iSERS microscopy is applied for breast cancer detection on single cells and tissues. Two different SERS substrates with high SERS enhancement, namely, Au-nanostars and Au/Au core-satellites-nanoparticles were synthesized. Bioconjugation of antibodies onto the nanoparticle surface is achieved either by direct binding to the Raman reporter molecules or to the polyethyleneglycol shell. SERS-labelled antibodies were then used for imaging of the expression level of protein biomarkers such as HER2 (human epidermal growth factor 2) on tissue sections or cell slides.

Firstly, the localization of HER2 expression on cancerous and normal formalin-fixed and paraffin-embedded (FFPE) breast tissue sections is shown using iSERS microscopy guided by wide field IF with Au-nanostar and fluorescence-labelled secondary antibody. The high contrast between the cancer and normal tissue sections in the acquired false-colour images demonstrates the very good selectivity of iSERS microscopy.

Secondly, the reproducibility of iSERS microscopic experiments was investigated on breast cell slides. A series of systematic imaging experiments on HER2 expression was carried out on a single breast cell. Through the optimization of the laser power, integration time and use of EMCCD gain, highly reproducible SERS images were obtained in repeated experiments.

Thirdly, single target/multi-colour iSERS experiments on single breast cells with up to six distinguishable SERS nanotags (six different Raman reporters), which were labelled with the same anti-HER2 antibody, were successfully performed. This demonstrates the multiplexing potential of iSERS microscopy.

Finally, a new approach of targeting multiple biomarkers to differentiate breast cancer cells in a mixture of cells was developed. The two biomarkers HER2 and epidermal

## SUMMARY

---

growth factor receptor (EGFR) were used to label SkBr-3 breast cancer cells, while the biomarker cluster of differentiation 45 (CD45) was used to label mononuclear (MNC) cells in the cell mixture.

These examples highlight the potential of iSERS microscopy for breast cancer detection. The methodology can be expanded to other diseases by simply conjugating other antibodies or ligands to the SERS nanoparticles.

### **7 Zusammenfassung**

In dieser Arbeit wurde die Immuno-SERS-Mikroskopie (iSERS) für die Brustkrebs-Detektion an einzelnen Zellen und Geweben angewendet. Dazu wurden zwei verschiedene SERS-Substrate, Gold-Nanosterne und Gold/Gold-Kern/Satelliten-Nanopartikel synthetisiert. Die benötigten Antikörper wurden im Fall der Gold-Nanosterne direkt an die selbstorganisierte Monolage aus Raman-Reportermolekülen und im Fall der Gold/Gold-Kern/Satelliten-Nanopartikel an die Polyethyenglykol-Schutzhülle konjugiert. Diese SERS-markierten Antikörper wurden dann zur Erfassung des Expressionsniveaus von Biomarkern, insbesondere dem humanen epidermalen Wachstumsfaktorrezeptor 2 (HER2), auf Gewebeschnitten und einzelnen Zellen benutzt.

Zuerst wurde die Lokalisierung von HER2 auf Formalin-fixierten und Paraffin-eingebetteten (FFPE)-Gewebeschnitten von gesunden und krebserkrankten Patientinnen mit Hilfe der iSERS-Mikroskopie sowie begleitend der Immunfluoreszenz gezeigt. In diesem Fall wurden Gold-Nanosterne als SERS-Marker und fluoreszenzmarkierte sekundäre Antikörper benutzt. Die erzeugten Raman-Falschfarbenbilder zeigen einen sehr hohen Kontrast zwischen krankem und normalem Gewebe, was die Selektivität der iSERS-Mikroskopie demonstriert.

Anschließend wurde die Reproduzierbarkeit der Lokalisierung von HER2 mittels iSERS-Mikroskopie auf einzelnen Brustkrebs-Zellen in wiederholten Experimenten gezeigt. Dazu wurde eine systematische Serie von Bildgebungs-Experimenten auf Einzelzell-Niveau durchgeführt. Durch die Optimierung der Laserleistung, Integrationszeit und der Kameraverstärkung (gain der EMCCD) konnten bei mehrfachem Abrastern der Probe reproduzierbare iSERS-Falschfarbenbilder erhalten werden.

## ZUSAMMENFASSUNG

---

In einem Mehrfarben/1-Zielmolekül-Experiment wurden sechs spektral unterscheidbare SERS-Marker (sechs verschiedene Raman-Reporter-Moleküle) synthetisiert, an anti-HER2-Antikörper konjugiert und auf einzelnen Brustkrebszellen lokalisiert.

Schließlich wurde ein 3-Farben/3-Zielmolekül-Experiment zur Identifizierung von Brustkrebszellen in einer Zellmischung konzipiert und durchgeführt. Die beiden Biomarker HER2 und EGFR (Epidermal Growth Factor Receptor) wurden zur Identifizierung von Brustkrebszellen (Zell-Linie SkBr-3) verwendet, während der Biomarker CD45 (Cluster of Differentiation 45) zur Markierung von mononukleären Zellen (MNC) in der Zellmischung verwendet wurde.

Die oben beschriebenen bildgebenden Untersuchungen mit Hilfe der iSERS-Mikroskopie, können somit für den Brustkrebs-Nachweis verwendet werden. Die Methodik kann auch auf andere Krankheiten ausgedehnt werden, indem andere Antikörper bzw. auch andere Liganden an die SERS-Nanopartikel konjugiert werden.

## 8 References

Abramczyk, H., and Brozek-Pluska, B. (2013). Raman imaging in biochemical and biomedical applications. Diagnosis and treatment of breast cancer. *Chem. Rev.* 113, 5766-5781.

Ai, X.Z., Ho, C.J.H., Aw, J., Attia, A.B.E., Mu, J., Wang, Y., Wang, X.Y., Wang, Y., Liu, X.G., Chen, H.B., et al. (2016). In vivo covalent cross-linking of photon-converted rare-earth nanostructures for tumour localization and theranostics. *Nat Commun.* 7.

Albrecht, M.G., and Creighton, J.A. (1977). Anomalously Intense Raman-Spectra of Pyridine at a Silver Electrode. *J. Am. Chem. Soc.* 99, 5215-5217.

Alvarez-Puebla, R.A., and Liz-Marzan, L.M. (2012). SERS Detection of Small Inorganic Molecules and Ions. *Angew. Chem., Int. Ed.* 51, 11214-11223.

Bang, Y.J., Van Cutsem, E., Feyereislova, A., and Investigators, T.T. (2010). Trastuzumab in combination with chemotherapy versus chemotherapy alone for treatment of HER2-positive advanced gastric or gastro-oesophageal junction cancer (TOGA): a phase 3, open-label, randomised controlled trial. *Lancet* 376, 687-97.

Barber, D.J., and Freestone, I.C. (1990). An Investigation of the Origin of the Color of the Lycurgus Cup by Analytical Transmission Electron-Microscopy. *Archaeometry* 32, 33-45.

Bastus, N.G., Comenge, J., and Puntès, V. (2011). Kinetically Controlled Seeded Growth Synthesis of Citrate-Stabilized Gold Nanoparticles of up to 200 nm: Size Focusing versus Ostwald Ripening. *Langmuir* 27, 11098-11105.

Bayer, E.A., and Wilchek, M. (1990). Application of avidin-biotin technology to affinity-based separations. *J. Chromatogr.* 510, 3-11.

Black, K.C.L., Yi, J., Rivera, J.G., Zelasko-Leon, D.C., and Messersmith, P.B. (2013). Polydopamine-enabled surface functionalization of gold nanorods for cancer cell-targeted imaging and photothermal therapy. *Nanomedicine* 8, 17-28.

Bodelon, G., Montes-Garcia, V., Fernandez-Lopez, C., Pastoriza-Santos, I., Perez-Juste, J., and Liz-Marzan, L.M. (2015). Au@pNIPAM SERRS Tags for Multiplex Immunophenotyping Cellular Receptors and Imaging Tumor Cells. *Small* 11, 4149-4157.

Campion, A., Ivanecky, J.E., Child, C.M., and Foster, M. (1995). On the Mechanism of Chemical Enhancement in Surface-Enhanced Raman-Scattering. *J. Am. Chem. Soc.* 117, 11807-11808.

## REFERENCES

---

- Chambers, A.F., Groom, A.C., and MacDonald, I.C. (2002). Dissemination and growth of cancer cells in metastatic sites. *Nat. Rev. Cancer* 2, 563-572.
- Chen, Y.C., Young, R.J., Macpherson, J.V., and Wilson, N.R. (2007). Single-walled carbon nanotube networks decorated with silver nanoparticles: A novel graded SERS substrate. *J. Phys. Chem. C* 111, 16167-16173.
- Chen, Y.W., Liu, T.Y., Chen, P.J., Chang, P.H., and Chen, S.Y. (2016). A High-Sensitivity and Low-Power Theranostic Nanosystem for Cell SERS Imaging and Selectively Photothermal Therapy Using Anti-EGFR-Conjugated Reduced Graphene Oxide/Mesoporous Silica/AuNPs Nanosheets. *Small* 12, 1458-1468.
- Cheng, Z., Choi, N., Wang, R., Lee, S., Moon, K.C., Yoon, S.Y., Chen, L., and Choo, J. (2017). Simultaneous Detection of Dual Prostate Specific Antigens Using Surface-Enhanced Raman Scattering-Based Immunoassay for Accurate Diagnosis of Prostate Cancer. *ACS Nano* 11, 4926-4933.
- Cho, I.-H., Das, M., Bhandari, P., and Irudayaraj, J. (2015). High performance immunochromatographic assay combined with surface enhanced Raman spectroscopy. *Sens. Actuators B* 213, 209-214.
- Choi, K.Y., Liu, G., Lee, S., and Chen, X.Y. (2012). Theranostic nanoplatfoms for simultaneous cancer imaging and therapy: current approaches and future perspectives. *Nanoscale* 4, 330-342.
- Chon, H., Lim, C., Ha, S.M., Ahn, Y., Lee, E.K., Chang, S.I., Seong, G.H., and Choo, J. (2010). On-Chip Immunoassay Using Surface-Enhanced Raman Scattering of Hollow Gold Nanospheres. *Anal. Chem.* 82, 5290-5295.
- Dasary, S.S.R., Singh, A.K., Senapati, D., Yu, H.T., and Ray, P.C. (2009). Gold Nanoparticle Based Label-Free SERS Probe for Ultrasensitive and Selective Detection of Trinitrotoluene. *J. Am. Chem. Soc.* 131, 13806-13812.
- de Aberasturi, D.J., Serrano-Montes, A.B., Langer, J., Henriksen-Lacey, M., Parak, W.J., and Liz-Marzan, L.M. (2016). Surface Enhanced Raman Scattering Encoded Gold Nanostars for Multiplexed Cell Discrimination. *Chem. Mater.* 28, 6779-6790.
- Dickerson, E.B., Dreaden, E.C., Huang, X.H., El-Sayed, I.H., Chu, H.H., Pushpanketh, S., McDonald, J.F., and El-Sayed, M.A. (2008). Gold nanorod assisted near-infrared plasmonic photothermal therapy (PPTT) of squamous cell carcinoma in mice. *Cancer Lett.* 269, 57-66.

## REFERENCES

---

- Dinish, U.S., Balasundaram, G., Chang, Y.T., and Olivo, M. (2014). Actively Targeted In Vivo Multiplex Detection of Intrinsic Cancer Biomarkers Using Biocompatible SERS Nanotags. *Sci. Rep.* 4, 4075.
- Doering, W.E., and Nie, S.M. (2003). Spectroscopic tags using dye-embedded nanoparticles and surface-enhanced Raman scattering. *Anal. Chem.* 75, 6171-6176.
- Eilers, P.H.C., Boelens, H.F.M. (2005). Baseline Correction with Asymmetric Least Squares Smoothing. Leiden University Medical Centre Report. Leiden: Leiden University Medical Centre.
- Fehm, T., Hoffmann, O., Aktas, B., Becker, S., Solomayer, E.F., Wallwiener, D., Kimmig, R., and Kasimir-Bauer, S. (2009). Detection and characterization of circulating tumor cells in blood of primary breast cancer patients by RT-PCR and comparison to status of bone marrow disseminated cells. *Breast Cancer Res.* 11, R59.
- Feng, L.Y., Chen, Y., Ren, J.S., and Qu, X.G. (2011). A graphene functionalized electrochemical aptasensor for selective label-free detection of cancer cells. *Biomaterials* 32, 2930-2937.
- Fields, R.C., Jeffe, D.B., Trinkaus, K., Zhang, Q., Arthur, C., Aft, R., Dietz, J.R., Eberlein, T.J., Gillanders, W.E., and Margenthaler, J.A. (2007). Surgical resection of the primary tumor is associated with increased long-term survival in patients with stage IV breast cancer after controlling for site of metastasis. *Ann. Surg. Oncol.* 14, 3345-3351.
- Fleischmann, M., Hendra, P.J., and Mcquillan, A.J. (1974). Raman-Spectra of Pyridine Adsorbed at a Silver Electrode. *Chem. Phys. Lett.* 26, 163-166.
- Frens, G. (1973). Controlled Nucleation for Regulation of Particle-Size in Monodisperse Gold Suspensions. *Nature* 241, 20-22.
- Gellner, M., Kömpe, K., and Schlücker, S. (2009). Multiplexing with SERS labels using mixed SAMs of Raman reporter molecules. *Anal. Bioanal. Chem.* 394, 1839-1844.
- Gersten, J., and Nitzan, A. (1980). Electromagnetic Theory of Enhanced Raman-Scattering by Molecules Adsorbed on Rough Surfaces. *J. Chem. Phys.* 73, 3023-3037.
- Grodzki, A.C., and Berenstein, E. (2010). Antibody purification: affinity chromatography - protein A and protein G Sepharose. *Methods Mol. Biol.* 588, 33-41.
- Gutman, S., and Kessler, L.G. (2006). The US Food and Drug Administration perspective on cancer biomarker development. *Nat. Rev. Cancer* 6, 565-571.

## REFERENCES

---

- Hao, F., Nehl, C.L., Hafner, J.H., and Nordlander, P. (2007). Plasmon resonances of a gold nanostar. *Nano Lett.* 7, 729-732.
- Hartkopf, A.D., Taran, F.A., Wallwiener, M., Hahn, M., Becker, S., Solomayer, E.F., Brucker, S.Y., Fehm, T.N., and Wallwiener, D. (2014). Prognostic relevance of disseminated tumour cells from the bone marrow of early stage breast cancer patients - results from a large single-centre analysis. *Eur. J. Cancer* 50, 2550-2559.
- Haun, J.B., Devaraj, N.K., Hilderbrand, S.A., Lee, H., and Weissleder, R. (2010). Bioorthogonal chemistry amplifies nanoparticle binding and enhances the sensitivity of cell detection. *Nat. Nanotechnol.* 5, 660-665.
- Hori, S.S., and Gambhir, S.S. (2011). Mathematical model identifies blood biomarker-based early cancer detection strategies and limitations. *Sci. Transl. Med.* 3, 109ra116.
- Hrelescu, C., Sau, T.K., Rogach, A.L., Jäckel, F., and Feldmann, J. (2009). Single gold nanostars enhance Raman scattering. *Appl. Phys. Lett.* 94, 153113.
- Huhtinen, P., Soukka, T., Lovgren, T., and Harma, H. (2004). Immunoassay of total prostate-specific antigen using europium (III) nanoparticle labels and streptavidin-biotin technology. *J. Immunol. Methods* 294, 111-122.
- Jana, D., Matti, C., He, J., and Sagle, L. (2015). Capping Agent-Free Gold Nanostars Show Greatly Increased Versatility and Sensitivity for Biosensing. *Anal. Chem.* 87, 3964-3972.
- Jeanmaire, D.L., and Vanduyne, R.P. (1977). Surface Raman Spectroelectrochemistry .1. Heterocyclic, Aromatic, and Aliphatic-Amines Adsorbed on Anodized Silver Electrode. *J. Electroanal. Chem.* 84, 1-20.
- Jehn, C., Küstner, B., Adam, P., Marx, A., Ströbel, P., Schmuck, C., and Schlücker, S. (2009). Water soluble SERS labels comprising a SAM with dual spacers for controlled bioconjugation. *Phys. Chem. Chem. Phys.* 11, 7499-7504.
- Jokerst, J.V., Lobovkina, T., Zare, R.N., and Gambhir, S.S. (2011). Nanoparticle PEGylation for imaging and therapy. *Nanomedicine* 6, 715-728.
- Jones, C.J., Mosley, S.M., Jeffrey, I.J., and Stoddart, R.W. (1987). Elimination of the non-specific binding of avidin to tissue sections. *Histochem. J.* 19, 264-268.
- Joo, S.W., Chung, T.D., Jang, W.C., Gong, M.S., Geum, N., and Kim, K. (2002). Surface-enhanced Raman scattering of 4-cyanobiphenyl on gold and silver nanoparticle surfaces. *Langmuir* 18, 8813-8816.

## REFERENCES

---

- Katayanagi, H., Hayashi, S., Hamaguchi, H.O., and Nishikawa, K. (2004). Structure of an ionic liquid, 1-n-butyl-3-methylimidazolium iodide, studied by wide-angle X-ray scattering and Raman spectroscopy. *Chem. Phys. Lett.* 392, 460-464.
- Keiner, R., Frosch, T., Massad, T., Trumbore, S., and Popp, J. (2014). Enhanced Raman multigas sensing - a novel tool for control and analysis of  $^{13}\text{CO}_2$  labeling experiments in environmental research. *Analyst* 139, 3879-3884.
- Kneipp, J., Kneipp, H., and Kneipp, K. (2008). SERS - a single-molecule and nanoscale tool for bioanalytics. *Chem. Soc. Rev.* 37, 1052-1060.
- Ko, H., Singamaneni, S., and Tsukruk, V.V. (2008). Nanostructured Surfaces and Assemblies as SERS Media. *Small* 4, 1576-1599.
- Kumar, G.V.P., Shruthi, S., Vibha, B., Reddy, B.A.A., Kundu, T.K., and Narayana, C. (2007). Hot spots in Ag core-Au shell nanoparticles potent for surface-enhanced Raman scattering studies of biomolecules. *J. Phys. Chem. C* 111, 4388-4392.
- Kumar, S., Aaron, J., and Sokolov, K. (2008). Directional conjugation of antibodies to nanoparticles for synthesis of multiplexed optical contrast agents with both delivery and targeting moieties. *Nat. Protoc.* 3, 314-320.
- Küstner, B., Gellner, M., Schütz, M., Schöppler, F., Marx, A., Ströbel, P., Adam, P., Schmuck, C., and Schlücker, S. (2009). SERS labels for red laser excitation: silica-encapsulated SAMs on tunable gold/silver nanoshells. *Angew. Chem., Int. Ed.* 48, 1950-1953.
- Lai, G.S., Wu, J., Ju, H.X., and Yan, F. (2011). Streptavidin-Functionalized Silver-Nanoparticle-Enriched Carbon Nanotube Tag for Ultrasensitive Multiplexed Detection of Tumor Markers. *Adv. Funct. Mater.* 21, 2938-2943.
- Laxman, B., Morris, D.S., Yu, J.J., Siddiqui, J., Cao, J., Mehra, R., Lonigro, R.J., Tsodikov, A., Wei, J.T., Tomlins, S.A., et al. (2008). A first-generation multiplex biomarker analysis of urine for the early detection of prostate cancer. *Cancer Res.* 68, 645-649.
- Lee, J.H., You, M.H., Kim, G.H., and Nam, J.M. (2014). Plasmonic Nanosnowmen with a Conductive Junction as Highly Tunable Nanoantenna Structures and Sensitive, Quantitative and Multiplexable Surface-Enhanced Raman Scattering Probes. *Nano Lett.* 14, 6217-6225.
- Lee, J.M., Park, H.K., Jung, Y., Kim, J.K., Jung, S.O., and Chung, B.H. (2007). Direct immobilization of protein G variants with various numbers of cysteine residues on a gold surface. *Anal. Chem.* 79, 2680-2687.

## REFERENCES

---

- Lee, P.C., and Meisel, D. (1982). Adsorption and Surface-Enhanced Raman of Dyes on Silver and Gold Sols. *J. Phys. Chem.* 86, 3391-3395.
- Lee, S., Chon, H., Lee, M., Choo, J., Shin, S.Y., Lee, Y.H., Rhyu, I.J., Son, S.W., and Oh, C.H. (2009). Surface-enhanced Raman scattering imaging of HER2 cancer markers overexpressed in single MCF7 cells using antibody conjugated hollow gold nanospheres. *Biosens. Bioelectron.* 24, 2260-2263.
- Lee, S., Chon, H., Yoon, S.Y., Lee, E.K., Chang, S.I., Lim, D.W., and Choo, J. (2012). Fabrication of SERS-fluorescence dual modal nanoprobe and application to multiplex cancer cell imaging. *Nanoscale* 4, 124-129.
- Li, J.F., Yang, Z.L., Ren, B., Liu, G.K., Fang, P.P., Jiang, Y.X., Wu, D.Y., and Tian, Z.Q. (2006). Surface-enhanced Raman spectroscopy using gold-core platinum-shell nanoparticle film electrodes: Toward a versatile vibrational strategy for electrochemical interfaces. *Langmuir* 22, 10372-10379.
- Li, J.L., Chen, L.X., Lou, T.T., and Wang, Y.Q. (2011). Highly Sensitive SERS Detection of  $As^{3+}$  Ions in Aqueous Media using Glutathione Functionalized Silver Nanoparticles. *ACS Appl. Mater. Interfaces* 3, 3936-3941.
- Li, M., Banerjee, S.R., Zheng, C., Pomper, M.G., and Barman, I. (2016). Ultrahigh affinity Raman probe for targeted live cell imaging of prostate cancer. *Chem. Sci.* 7, 6779-6785.
- Li, X.X., Lee, J.P., Blinn, K.S., Chen, D.C., Yoo, S., Kang, B., Bottomley, L.A., El-Sayed, M.A., Park, S., and Liu, M.L. (2014). High-temperature surface enhanced Raman spectroscopy for in situ study of solid oxide fuel cell materials. *Energy Environ. Sci.* 7, 306-310.
- Lim, E.K., Kim, T., Paik, S., Haam, S., Huh, Y.M., and Lee, K. (2015). Nanomaterials for Theranostics: Recent Advances and Future Challenges. *Chem. Rev.* 115, 327-394.
- Lim, I.I.S., Njoki, P.N., Park, H.Y., Wang, X., Wang, L.Y., Mott, D., and Zhong, C.J. (2008). Gold and magnetic oxide/gold core/shell nanoparticles as bio-functional nanoprobe. *Nanotechnology* 19, 305102.
- Lin, L., Tian, X.D., Hong, S.L., Dai, P., You, Q.C., Wang, R.Y., Feng, L.S., Xie, C., Tian, Z.Q., and Chen, X. (2013). A Bioorthogonal Raman Reporter Strategy for SERS Detection of Glycans on Live Cells. *Angew. Chem., Int. Ed.* 52, 7266-7271.
- Liu, B., Zhao, X., Jiang, W., Fu, D., and Gu, Z. (2016). Multiplex bioassays encoded by photonic crystal beads and SERS nanotags. *Nanoscale* 8, 17465-17471.

## REFERENCES

---

- Liu, H.B., Du, X.J., Zang, Y.X., Li, P., and Wang, S. (2017a). SERS-Based Lateral Flow Strip Biosensor for Simultaneous Detection of *Listeria monocytogenes* and *Salmonella enterica* Serotype Enteritidis. *J. Agric. Food Chem.* 65, 10290-10299.
- Liu, R., Zhao, J., Han, G., Zhao, T., Zhang, R., Liu, B., Liu, Z., Zhang, C., Yang, L., and Zhang, Z. (2017b). Click-Functionalized SERS Nanoprobes with Improved Labeling Efficiency and Capability for Cancer Cell Imaging. *ACS Appl. Mater. Interfaces* 9, 38222-38229.
- Liu, X.J., Knauer, M., Ivleva, N.P., Niessner, R., and Haisch, C. (2010). Synthesis of Core-Shell Surface-Enhanced Raman Tags for Bioimaging. *Anal. Chem.* 82, 441-446.
- Liu, X.K., Xu, H.L., Xia, H.B., and Wang, D.Y. (2012). Rapid Seeded Growth of Monodisperse, Quasi-Spherical, Citrate-Stabilized Gold Nanoparticles via H<sub>2</sub>O<sub>2</sub> Reduction. *Langmuir* 28, 13720-13726.
- Lohse, S.E., and Murphy, C.J. (2013). The Quest for Shape Control: A History of Gold Nanorod Synthesis. *Chem. Mater.* 25, 1250-1261.
- Lu, L.H., Sun, G.Y., Zhang, H.J., Wang, H.S., Xi, S.Q., Hu, J.Q., Tian, Z.Q., and Chen, R. (2004). Fabrication of core-shell Au-Pt nanoparticle film and its potential application as catalysis and SERS substrate. *J. Mater. Chem.* 14, 1005-1009.
- Lutz, B., Dentinger, C., Sun, L., Nguyen, L., Zhang, J., Chmura, A., Allen, A., Chan, S., and Knudsen, B. (2008). Raman nanoparticle probes for antibody-based protein detection in tissues. *J. Histochem. Cytochem.* 56, 371-379.
- Ma, M., Yin, H.H., Xu, L.G., Wu, X.L., Kuang, H., Wang, L.B., and Xu, C.L. (2014). Ultrasensitive aptamer-based SERS detection of PSAs by heterogeneous satellite nanoassemblies. *Chem. Commun.* 50, 9737-9740.
- MacLaughlin, C.M., Mullaithilaga, N., Yang, G., Ip, S.Y., Wang, C., and Walker, G.C. (2013). Surface-enhanced Raman scattering dye-labeled Au nanoparticles for triplexed detection of leukemia and lymphoma cells and SERS flow cytometry. *Langmuir* 29, 1908-1919.
- McMahon, J.M., Henry, A.I., Wustholz, K.L., Natan, M.J., Freeman, R.G., Van Duyne, R.P., and Schatz, G.C. (2009). Gold nanoparticle dimer plasmonics: finite element method calculations of the electromagnetic enhancement to surface-enhanced Raman spectroscopy. *Anal. Bioanal. Chem.* 394, 1819-1825.

## REFERENCES

---

- Mitchell, P.S., Parkin, R.K., Kroh, E.M., Fritz, B.R., Wyman, S.K., Pogosova-Agadjanyan, E.L., Peterson, A., Noteboom, J., O'Briant, K.C., Allen, A., et al. (2008). Circulating microRNAs as stable blood-based markers for cancer detection. *Proc. Natl Acad. Sci. USA* 105, 10513-10518.
- Mulvaney, S.P., Musick, M.D., Keating, C.D., and Natan, M.J. (2003). Glass-coated, analyte-tagged nanoparticles: A new tagging system based on detection with surface-enhanced Raman scattering. *Langmuir* 19, 4784-4790.
- Ndokoye, P., Ke, J., Liu, J., Zhao, Q.D., and Li, X.Y. (2014). L-Cysteine-Modified Gold Nanostars for SERS-Based Copper Ions Detection in Aqueous Media. *Langmuir* 30, 13491-13497.
- Nehl, C.L., Liao, H., and Hafner, J.H. (2006). Optical properties of star-shaped gold nanoparticles. *Nano Lett.* 6, 683-688.
- Ngo, H.T., Gandra, N., Fales, A.M., Taylor, S.M., and Vo-Dinh, T. (2016). Sensitive DNA detection and SNP discrimination using ultrabright SERS nanorattles and magnetic beads for malaria diagnostics. *Biosens. Bioelectron.* 81, 8-14.
- Ni, J., Lipert, R.J., Dawson, G.B., and Porter, M.D. (1999). Immunoassay readout method using extrinsic Raman labels adsorbed on immunogold colloids. *Anal. Chem.* 71, 4903-4908.
- Otto, A., Mrozek, I., Grabhorn, H., and Akemann, W. (1992). Surface-Enhanced Raman-Scattering. *J. Phys. Condens. Matter* 4, 1143-1212.
- Park, H., Lee, S., Chen, L., Lee, E.K., Shin, S.Y., Lee, Y.H., Son, S.W., Oh, C.H., Song, J.M., Kang, S.H., et al. (2009). SERS imaging of HER2-overexpressed MCF7 cells using antibody-conjugated gold nanorods. *Phys. Chem. Chem. Phys.* 11, 7444-7449.
- Peterson, V.M., Castro, C.M., Lee, H., and Weissleder, R. (2012). Orthogonal Amplification of Nanoparticles for Improved Diagnostic Sensing. *ACS Nano* 6, 3506-3513.
- Petricoin, E.F., Belluco, C., Araujo, R.P., and Liotta, L.A. (2006). The blood peptidome: a higher dimension of information content for cancer biomarker discovery. *Nat. Rev. Cancer* 6, 961-967.
- Piccart-Gebhart, M.J., Procter, M., Leyland-Jones, B., Goldhirsch, A., Untch, M., Smith, I., Gianni, L., Baselga, J., Bell, R., Jackisch, C., et al. (2005). Trastuzumab after adjuvant chemotherapy in HER2-positive breast cancer. *N. Engl. J. Med.* 353, 1659-1672.
- Pines, D., and Bohm, D. (1952). A Collective Description of Electron Interactions .2. Collective Vs Individual Particle Aspects of the Interactions. *Phys. Rev.* 85, 338-353.

## REFERENCES

---

- Qian, X., Peng, X.H., Ansari, D.O., Yin-Goen, Q., Chen, G.Z., Shin, D.M., Yang, L., Young, A.N., Wang, M.D., and Nie, S. (2008a). In vivo tumor targeting and spectroscopic detection with surface-enhanced Raman nanoparticle tags. *Nat. Biotechnol.* 26, 83-90.
- Qian, X.M., and Nie, S.M. (2008b). Single-molecule and single-nanoparticle SERS: from fundamental mechanisms to biomedical applications. *Chem. Soc. Rev.* 37, 912-920.
- Rakha, E.A., El-Sayed, M.E., Green, A.R., Lee, A.H.S., Robertson, J.F., and Ellis, I.O. (2007). Prognostic markers in triple-negative breast cancer. *Cancer* 109, 25-32.
- Raman, C.V., and Krishnan, K.S. (1928). A new type of secondary radiation. *Nature* 121, 501-502.
- Rayleigh, J. W. S. (1907). On the dynamical theory of gratings. *Proc. R. Soc. London, Ser. A* 79, 399-416.
- Ritchie, R.H. (1957). Plasma Losses by Fast Electrons in Thin Films. *Phys. Rev.* 106, 874-881.
- Rong, Z., Xiao, R., Wang, C.W., Wang, D.G., and Wang, S.Q. (2015). Plasmonic Ag Core-Satellite Nanostructures with a Tunable Silica-Spaced Nanogap for Surface-Enhanced Raman Scattering. *Langmuir* 31, 8129-8137.
- Ruan, Q.F., Shao, L., Shu, Y.W., Wang, J.F., and Wu, H.K. (2014). Growth of Monodisperse Gold Nanospheres with Diameters from 20 nm to 220 nm and Their Core/Satellite Nanostructures. *Adv. Opt. Mater.* 2, 65-73.
- Rubin, I., and Yarden, Y. (2001). The basic biology of HER2. *Ann. Oncol.* 12, 3-8.
- Salehi, M., Schneider, L., Strobel, P., Marx, A., Packeisen, J., and Schlücker, S. (2014). Two-color SERS microscopy for protein co-localization in prostate tissue with primary antibody-protein A/G-gold nanocluster conjugates. *Nanoscale* 6, 2361-2367.
- Samal, A.K., Polavarapu, L., Rodal-Cedeira, S., Liz-Marzan, L.M., Perez-Juste, J., and Pastoriza-Santos, I. (2013). Size Tunable Au@Ag Core Shell Nanoparticles: Synthesis and Surface-Enhanced Raman Scattering Properties. *Langmuir* 29, 15076-15082.
- Samanta, A., Maiti, K.K., Soh, K.S., Liao, X.J., Vendrell, M., Dinish, U.S., Yun, S.W., Bhuvaneshwari, R., Kim, H., Rautela, S., et al. (2011). Ultrasensitive Near-Infrared Raman Reporters for SERS-Based In Vivo Cancer Detection. *Angew. Chem., Int. Ed.* 50, 6089-6092.
- Schatz, G. C, Van Duyne, R. P. (2002). In *Handbook of Vibrational Spectroscopy*. Chalmers, J. M., Griffiths, P. R., Eds.; Wiley: New York 1, 759-774.

## REFERENCES

---

- Schlücker, S. (2009). SERS microscopy: nanoparticle probes and biomedical applications. *ChemPhysChem* 10, 1344-1354.
- Schlücker, S., Küstner, B., Punge, A., Bonfig, R., Marx, A., and Ströbel, P. (2006). Immuno-Raman microspectroscopy: In situ detection of antigens in tissue specimens by surface-enhanced Raman scattering. *J. Raman Spectrosc.* 37, 719-721.
- Schütz, M., Steinigeweg, D., Salehi, M., Kömpe, K., and Schlücker, S. (2011). Hydrophilically stabilized gold nanostars as SERS labels for tissue imaging of the tumor suppressor p63 by immuno-SERS microscopy. *Chem. Commun.* 47, 4216-4218.
- Schwartzberg, A.M., Grant, C.D., Wolcott, A., Talley, C.E., Huser, T.R., Bogomolni, R., and Zhang, J.Z. (2004). Unique gold nanoparticle aggregates as a highly active surface-enhanced Raman scattering substrate. *J. Phys. Chem. B* 108, 19191-19197.
- Schwartzberg, A.M., Olson, T.Y., Talley, C.E., and Zhang, J.Z. (2006). Synthesis, characterization, and tunable optical properties of hollow gold nanospheres. *J. Phys. Chem. B* 110, 19935-19944.
- Sha, M.Y., Xu, H., Natan, M.J., and Cromer, R. (2008). Surface-enhanced Raman scattering tags for rapid and homogeneous detection of circulating tumor cells in the presence of human whole blood. *J. Am. Chem. Soc.* 130, 17214-17215.
- Shanmukh, S., Jones, L., Driskell, J., Zhao, Y.P., Dluhy, R., and Tripp, R.A. (2006). Rapid and sensitive detection of respiratory virus molecular signatures using a silver nanorod array SERS substrate. *Nano Lett.* 6, 2630-2636.
- Sharma, H., and Mutharasan, R. (2013). Half Antibody Fragments Improve Biosensor Sensitivity without Loss of Selectivity. *Anal. Chem.* 85, 2472-2477.
- Shi, S., Wang, L.B., Su, R.X., Liu, B.S., Huang, R.L., Qi, W., and He, Z.M. (2015). A polydopamine-modified optical fiber SPR biosensor using electroless-plated gold films for immunoassays. *Biosens. Bioelectron.* 74, 454-460.
- Shi, S.R., Shi, Y., and Taylor, C.R. (2011). Antigen Retrieval Immunohistochemistry: Review and Future Prospects in Research and Diagnosis over Two Decades. *J. Histochem. Cytochem.* 59, 13-32.
- Shi, W., Paproski, R.J., Moore, R., and Zemp, R. (2014). Detection of circulating tumor cells using targeted surface-enhanced Raman scattering nanoparticles and magnetic enrichment. *J. Biomed. Opt.* 19, 056014.

## REFERENCES

---

- Shrestha, R., Elsabahy, M., Luehmann, H., Samarajeewa, S., Florez-Malaver, S., Lee, N.S., Welch, M.J., Liu, Y.J., and Wooley, K.L. (2012). Hierarchically Assembled Theranostic Nanostructures for siRNA Delivery and Imaging Applications. *J. Am. Chem. Soc.* 134, 17362-17365.
- Siegel, R.L., Miller, K.D., and Jemal, A. (2016). Cancer statistics, 2016. *Ca-Cancer J. Clin.* 66, 7-30.
- Simmons, C., Miller, N., Geddie, W., Gianfelice, D., Oldfield, M., Dranitsaris, G., and Clemons, M.J. (2009). Does confirmatory tumor biopsy alter the management of breast cancer patients with distant metastases? *Ann. Oncol.* 20, 1499-1504.
- Slamon, D.J., Clark, G.M., Wong, S.G., Levin, W.J., Ullrich, A., and Mcguire, W.L. (1987). Human-Breast Cancer - Correlation of Relapse and Survival with Amplification of the HER-2/Neu Oncogene. *Science* 235, 177-182.
- Slamon, D.J., Godolphin, W., Jones, L.A., Holt, J.A., Wong, S.G., Keith, D.E., Levin, W.J., Stuart, S.G., Udove, J., Ullrich, A., et al. (1989). Studies of the HER-2/neu proto-oncogene in human breast and ovarian cancer. *Science* 244, 707-712.
- Sokolov, K., Follen, M., Aaron, J., Pavlova, I., Malpica, A., Lotan, R., and Richards-Kortum, R. (2003). Real-time vital optical imaging of precancer using anti-epidermal growth factor receptor antibodies conjugated to gold nanoparticles. *Cancer Res.* 63, 1999-2004.
- Sun, C.L., Zhang, R., Gao, M.X., and Zhang, X.M. (2015). A rapid and simple method for efficient capture and accurate discrimination of circulating tumor cells using aptamer conjugated magnetic beads and surface-enhanced Raman scattering imaging. *Anal. Bioanal. Chem.* 407, 8883-8892.
- Talley, C.E., Jackson, J.B., Oubre, C., Grady, N.K., Hollars, C.W., Lane, S.M., Huser, T.R., Nordlander, P., and Halas, N.J. (2005). Surface-enhanced Raman scattering from individual Au nanoparticles and nanoparticle dimer substrates. *Nano Lett.* 5, 1569-1574.
- Tarin, D. (2006). New insights into the pathogenesis of breast cancer metastasis. *Breast Dis.* 26, 13-25.
- Thacker, V.V., Herrmann, L.O., Sigle, D.O., Zhang, T., Liedl, T., Baumberg, J.J., and Keyser, U.F. (2014). DNA origami based assembly of gold nanoparticle dimers for surface-enhanced Raman scattering. *Nat. Commun.* 5, 3448.
- Thakur, B.K., Zhang, H., Becker, A., Matei, I., Huang, Y., Costa-Silva, B., Zheng, Y., Hoshino, A., Brazier, H., Xiang, J., et al. (2014). Double-stranded DNA in exosomes: a novel biomarker in cancer detection. *Cell Res.* 24, 766-769.

## REFERENCES

---

- Turkevich, J., Stevenson, P.C., and Hillier, J. (1951). A Study of the Nucleation and Growth Processes in the Synthesis of Colloidal Gold. *Discuss. Faraday Soc.* 11, 55-75.
- von Maltzahn, G., Centrone, A., Park, J.H., Ramanathan, R., Sailor, M.J., Hatton, T.A., and Bhatia, S.N. (2009). SERS-Coded Gold Nanorods as a Multifunctional Platform for Densely Multiplexed Near-infrared Imaging and Photothermal Heating. *Adv. Mater.* 21, 3175.
- Wang, X., Xing, X., Zhang, B., Liu, F., Cheng, Y., and Shi, D. (2014a). Surface engineered antifouling optomagnetic SPIONs for bimodal targeted imaging of pancreatic cancer cells. *Int. J. Nanomed.* 9, 1601-1615.
- Wang, X.P., Walkenfort, B., König, M., König, L., Kasimir-Bauer, S., and Schlücker, S. (2017a). Fast and reproducible iSERS microscopy of single HER2-positive breast cancer cells using gold nanostars as SERS nanotags. *Faraday Discuss.* 205, 377-386.
- Wang, X.P., Zhang, Y.Y., König, M., Papadopoulou, E., Walkenfort, B., Kasimir-Bauer, S., Bankfalvi, A., and Schlücker, S. (2016). iSERS microscopy guided by wide field immunofluorescence: analysis of HER2 expression on normal and breast cancer FFPE tissue sections. *Analyst* 141, 5113-5119.
- Wang, Y.Q., Yan, B., and Chen, L.X. (2013). SERS Tags: Novel Optical Nanoprobes for Bioanalysis. *Chem. Rev.* 113, 1391-1428.
- Wang, Y.S., Polavarapu, L., and Liz-Marzan, L.M. (2014b). Reduced Graphene Oxide-Supported Gold Nanostars for Improved SERS Sensing and Drug Delivery. *ACS Appl. Mater. Interfaces* 6, 21798-21805.
- Wang, Z., Zong, S., Wu, L., Zhu, D., and Cui, Y. (2017b). SERS-Activated Platforms for Immunoassay: Probes, Encoding Methods, and Applications. *Chem. Rev.* 117, 7910-7963.
- Webb, J.A., Ou, Y.C., Faley, S., Paul, E.P., Hittinger, J.P., Cutright, C.C., Lin, E.C., Bellan, L.M., and Bardhan, R. (2017). Theranostic Gold Nanoantennas for Simultaneous Multiplexed Raman Imaging of Immunomarkers and Photothermal Therapy. *ACS Omega* 2, 3583-3594.
- Weitz, D.A., Garoff, S., and Gramila, T.J. (1982). Excitation-Spectra of Surface-Enhanced Raman-Scattering on Silver-Island Films. *Opt. Lett.* 7, 168-170.
- Wen, C.Y., Liao, F., Liu, S.S., Zhao, Y., Kang, Z.H., Zhang, X.L., and Shao, M.W. (2013). Bi-functional ZnO-RGO-Au substrate: photocatalysts for degrading pollutants and SERS substrates for real-time monitoring. *Chem. Commun.* 49, 3049-3051.

## REFERENCES

---

- Willets, K.A., and Van Duyne, R.P. (2007). Localized surface plasmon resonance spectroscopy and sensing. *Annu. Rev. Phys. Chem.* 58, 267-297.
- Wood, R.W. (1902). On a remarkable case of uneven distribution of light in a diffraction grating spectrum. *Philos. Mag.* 4, 396-402.
- Wu, C.H., Khanikaev, A.B., Adato, R., Arju, N., Yanik, A.A., Altug, H., and Shvets, G. (2012). Fano-resonant asymmetric metamaterials for ultrasensitive spectroscopy and identification of molecular monolayers. *Nat. Mater.* 11, 69-75.
- Wu, X.Y., Liu, H.J., Liu, J.Q., Haley, K.N., Treadway, J.A., Larson, J.P., Ge, N.F., Peale, F., and Bruchez, M.P. (2003). Immunofluorescent labeling of cancer marker Her2 and other cellular targets with semiconductor quantum dots. *Nat. Biotechnol.* 21, 41-46.
- Wu, Y.J., West, A.P., Kim, H.J., Thornton, M.E., Ward, A.B., and Bjorkman, P.J. (2013). Structural Basis for Enhanced HIV-1 Neutralization by a Dimeric Immunoglobulin G Form of the Glycan-Recognizing Antibody 2G12. *Cell Rep.* 5, 1443-1455.
- Xiong, K., Wei, W., Jin, Y., Wang, S., Zhao, D., Wang, S., Gao, X., Qiao, C., Yue, H., Ma, G., et al. (2016). Biomimetic Immuno-Magnetosomes for High-Performance Enrichment of Circulating Tumor Cells. *Adv. Mater.* 28, 7929-7935.
- Yang, J., Wang, Z., Zong, S., Song, C., Zhang, R., and Cui, Y. (2012). Distinguishing breast cancer cells using surface-enhanced Raman scattering. *Anal. Bioanal. Chem.* 402, 1093-1100.
- Yang, T., and Jiang, J. (2016). Embedding Raman Tags between Au Nanostar@Nanoshell for Multiplex Immunosensing. *Small* 12, 4980-4985.
- Yang, Y., Shi, J.L., Kawamura, G., and Nogami, M. (2008). Preparation of Au-Ag, Ag-Au core-shell bimetallic nanoparticles for surface-enhanced Raman scattering. *Scr. Mater.* 58, 862-865.
- Yarden, Y., and Sliwkowski, M.X. (2001). Untangling the ErbB signalling network. *Nat. Rev. Mol. Cell Biol.* 2, 127-137.
- Yazgan, N.N., Boyaci, I.H., Topcu, A., and Tamer, U. (2012). Detection of melamine in milk by surface-enhanced Raman spectroscopy coupled with magnetic and Raman-labeled nanoparticles. *Anal. Bioanal. Chem.* 403, 2009-2017.
- Yuan, H., Liu, Y., Fales, A.M., Li, Y.L., Liu, J., and Vo-Dinh, T. (2013). Quantitative surface-enhanced resonant Raman scattering multiplexing of biocompatible gold nanostars for in vitro and ex vivo detection. *Anal. Chem.* 85, 208-212.

## REFERENCES

---

- Zhai, Y.M., Zhai, J.F., Wang, Y.L., Guo, S.J., Ren, W., and Dong, S.J. (2009). Fabrication of Iron Oxide Core/Gold Shell Submicrometer Spheres with Nanoscale Surface Roughness for Efficient Surface-Enhanced Raman Scattering. *J. Phys. Chem. C* 113, 7009-7014.
- Zhang, B.B., Yu, J.N., Liu, C., Wang, J., Han, H.X., Zhang, P.F., and Shi, D.L. (2016). Improving detection sensitivity by oriented bioconjugation of antibodies to quantum dots with a flexible spacer arm for immunoassay. *RSC Adv.* 6, 50119-50127.
- Zhang, D., Huang, L., Liu, B., Ni, H., Sun, L., Su, E., Chen, H., Gu, Z., and Zhao, X. (2018). Quantitative and ultrasensitive detection of multiplex cardiac biomarkers in lateral flow assay with core-shell SERS nanotags. *Biosens. Bioelectron.* 106, 204-211.
- Zhang, J.Z. (2010). Biomedical Applications of Shape-Controlled Plasmonic Nanostructures: A Case Study of Hollow Gold Nanospheres for Photothermal Ablation Therapy of Cancer. *J. Phys. Chem. Lett.* 1, 686-695.
- Zhang, L., Huang, Y.J., Wang, J.Y., Rong, Y., Lai, W.H., Zhang, J.W., and Chen, T. (2015). Hierarchical Flowerlike Gold Nanoparticles Labeled Immunochromatography Test Strip for Highly Sensitive Detection of Escherichia coli O157:H7. *Langmuir* 31, 5537-5544.
- Zhang, Y., Qiu, Y., Lin, L., Gu, H., Xiao, Z., and Ye, J. (2017). Ultraphotostable Mesoporous Silica-Coated Gap-Enhanced Raman Tags (GERTs) for High-Speed Bioimaging. *ACS Appl. Mater. Interfaces* 9, 3995-4005.
- Zhang, Y.Y., Wang, X.P., Perner, S., Bankfalvi, A., and Schlücker, S. (2018). Effect of Antigen Retrieval Methods on Nonspecific Binding of Antibody-Metal Nanoparticle Conjugates on Formalin-Fixed Paraffin-Embedded Tissue. *Anal. Chem.* 90, 760-768.
- Zhang, Z., Bast, R.C., Yu, Y.H., Li, J.N., Sokoll, L.J., Rai, A.J., Rosenzweig, J.M., Cameron, B., Wang, Y.Y., Meng, X.Y., et al. (2004). Three biomarkers identified from serum proteomic analysis for the detection of early stage ovarian cancer. *Cancer Res.* 64, 5882-5890.
- Zhao, J., Long, L., Weng, G.J., Li, J.J., Zhu, J., and Zhao, J.W. (2017). Multi-branch Au/Ag bimetallic core-shell-satellite nanoparticles as a versatile SERS substrate: the effect of Au branches in a mesoporous silica interlayer. *J. Mater. Chem. C* 5, 12678-12687.
- Zheng, X., Chen, Y.H., Chen, Y., Bi, N., Qi, H.B., Qin, M.H., Song, D., Zhang, H.Q., and Tian, Y. (2012). High performance Au/Ag core/shell bipyramids for determination of thiram based on surface-enhanced Raman scattering. *J. Raman Spectrosc.* 43, 1374-1380.

## REFERENCES

---

- Zheng, X.S., Hu, P., Cui, Y., Zong, C., Feng, J.M., Wang, X., and Ren, B. (2014). BSA-Coated Nanoparticles for Improved SERS-Based Intracellular pH Sensing. *Anal. Chem.* 86, 12250-12257.
- Zheng, Y.H., Thai, T., Reineck, P., Qiu, L., Guo, Y.M., and Bach, U. (2013). DNA-Directed Self-Assembly of Core-Satellite Plasmonic Nanostructures: A Highly Sensitive and Reproducible Near-IR SERS Sensor. *Adv. Funct. Mater.* 23, 1519-1526.
- Zhou, H.B., Yang, D.T., Ivleva, N.P., Mircescu, N.E., Niessner, R., and Haisch, C. (2014). SERS Detection of Bacteria in Water by in Situ Coating with Ag Nanoparticles. *Anal. Chem.* 86, 1525-1533.
- Zhou, J.J., Xiong, Q.R., Ma, J.L., Ren, J.H., Messersmith, P.B., Chen, P., and Duan, H.W. (2016). Polydopamine-Enabled Approach toward Tailored Plasmonic Nanogapped Nanoparticles: From Nanogap Engineering to Multifunctionality. *ACS Nano* 10, 11066-11075.
- Zong, S., Chen, C., Wang, Z., Zhang, Y., and Cui, Y. (2016). Surface Enhanced Raman Scattering Based in Situ Hybridization Strategy for Telomere Length Assessment. *ACS Nano* 10, 2950-2959.

## 9 Appendix

### Acknowledgements

First and foremost, I would like to express my sincere thanks to my PhD supervisor Prof. Dr. Sebastian Schlücker to guide me into the new field of imaging-based diagnostics for clinical applications using fantastic nanoparticles-labelled antibodies. The endless support for me in the research as well as the discussion helps me get such great progress in the field of nano-diagnostics. Thank you for providing fundamental instruments and collaboration with professors in the university hospital. Great thanks to you also for the correction of my PhD thesis.

I greatly appreciate Prof. Sabine Kasimir-Bauer for being the second reviewer for my PhD thesis and Prof. Oliver Schmitz for being the chairman of my PhD defense.

Herein, thanks to Prof. Dr. Wei Xie who introduced me to the whole group and helped me when I have questions in either research or life.

I would like to give my special and earnest thanks to Dr. Yuying Zhang. Thank you so much for introducing me to the topic of iSERS microscopy on tissue sections and teaching me lots of experimental skills in this field. You are always so patient and willing to answer my questions when I get confused. The nice and interesting discussion we had before gave me deeper insight into this field.

Then, I would like to thank Jun and Banafshe. The frequent talks and chats on the daily life and scientific work in the lab cheer me besides the experimental work. I am also grateful to Bernd who teaches me carefully about how to use the major instruments. Thank you for Jörg who is always having fun with me in the lab. Thank Ela for the collaboration to finish the multi-colour iSERS microscopy of HER2 distribution on cell slides. Special thanks should also be given to our secretary Katrina for helping me about

## APPENDIX

---

all the documental work as well as German translation. I greatly appreciate about all the group activities held by all of the group members and the seminar time.

In addition, I feel lucky to have the chance to work short time in the hospital of Essen. I express my heartfelt thanks to my collaboration partners Prof. Dr. Bankfalvi Agnes and Prof. Sabine Kasimir-Bauer.

Thank Prof. Dr. Bankfalvi for giving me the permission to have the access of the chemical reagents and instruments at the pathology department in the hospital. I would like to thank Ms. Andrea Kutriz for teaching me all related pathological experiments.

I am thankful to Lisa König to prepare all the cytopinned cell slides as well as the useful discussion we had before.

I am also grateful to Prof. Matthias Gunzer and his group members for permitting me to use the Leica fluorescence microscope and other instruments.

I would like to express my thanks to my Chinese friends here to make the life more wonderful.

Special thanks to CSC (China Scholarship Council) for the financial support to let me have the valuable opportunity to study as a full PhD student in Germany.

Last, my sincere great thanks should definitely go to my beloved family in China. Without their endless support and understanding, I could not have all the progress achieved so far. I am pretty thankful to my husband Dr. Jifu Duan who is always accompanying me and giving me the tremendous support for the scientific work and daily life. You are always believing me and standing on my side to figure out the problems we met since the bachelor study. The mutual help we give to each other will also last for the rest of the scientific work.

**List of abbreviations**

$A$	absorbance
$A(\nu_s)$	enhancement factor of the Raman scattering
$A(\nu_L)$	enhancement factor of the local excited laser field
$\text{AgNO}_3$	silver nitrate
$\text{AgNP}$	silver nanoparticle
$\text{AuNP}$	gold nanoparticle
$\text{AuNPs}$	gold nanoparticles
$\text{AuNS}$	gold nanostars
BPDT	biphenyl-4,4'-dithiol
BSA	bovine serum albumin
$c$	concentration
CCD	charge-coupled device
CD45	cluster of differentiation 45
CE	chemical enhancement
CTAB	cetyl-trimethylammonium bromide
CTAC	cetyl-trimethylammonium chloride
CTC	circulating tumour cell
$d/R$	radius of the scattering sphere
$D$	translational diffusion coefficient

## APPENDIX

---

DAPI	4',6-diamidino-2-phenylindole
DBCO	dibenzocyclooctin
DNA	deoxyribonucleic acid
DLS	dynamic light scattering
DTC	disseminated tumour cell
DTNB	5,5'-dithiobis(2-nitrobenzoic acid)
$E_0$	incident field
$E_0(\omega_0)$	incoming electromagnetic field
EDC	1-ethyl-3-(3-dimethylaminopropyl) carbodiimide
EDTA	ethylenediaminetetraacetic acid
EGFR	epidermal growth factor receptor
$E_{loc}$	local electric field
EM	electromagnetic
EMCCD	electron multiplying charge-coupled device
ER	estrogen receptor
FFPE	formalin-fixed paraffin-embedded
HAuCl <sub>4</sub>	tetrachloroauric acid
HCl	hydrochloric acid
HEPES	4-(2-hydroxyethyl)-1-piperazineethanesulfonic acid
HER2	human epidermal growth factor receptor 2

## APPENDIX

---

HIER	heat-induced epitope retrieval
HRP	horseradish peroxidase
HS-PEG-COOH	poly(ethylene glycol) 2-mercaptoethyl ether acetic acid
<i>I</i>	intensity
$I(v_L)$	intensity of the excitation laser
IgG	immunoglobulin G
IHC	immunohistochemistry
IF	immunofluorescence
iSERS	immuno-SERS
<i>L</i>	light path length
LSPR	localized surface plasmon resonance
mL	milliliter
mM	millimolar
MUTAB	(11-mercaptopundecyl)-N,N,N-trimethylammonium bromide
MBA	4-mercaptobenzoic acid
MEM	minimal essential medium
min	minute
MMC	7-mercapto-4-methylcoumarin
MNC	mononuclear
MPTMS	(3-mercaptopropyl) trimethoxysilane

## APPENDIX

---

N	number
NaBH <sub>4</sub>	sodium borohydride
NaBr	sodium bromide
NaCl	sodium chloride
NP	nanoparticle
NPs	nanoparticles
NTP	4-nitrothiophenol
OD	optical density
PAH	poly (allylamine hydrochloride)
PBS	phosphate buffer saline
PDA	polydopamine
PDB	protein data bank
PEG	polyethylene glycol
PFA	paraformaldehyde
PIER	protease-induced epitope retrieval
PR	progesterone receptor
PrA	protein A
PrG	protein G
PSS	poly (sodium 4-styrenesulfonate)
PVP	polyvinylpyrrolidone
R	distance between the detecting point and the scattered sphere

## APPENDIX

---

RSD	relative standard deviation
RT	room temperature
SAM	self-assembled monolayer
SDS	sodium dodecyl sulfate
SERS	surface-enhanced Raman scattering
SPR	surface plasmon resonance
sulfo-NHS	N-hydroxysulfosuccin-imide sodium salt
$T$	absolute temperature
TCO	trans-cyclooctene
TEM	transmission electron microscopy
TEOS	tetraethyl orthosilicate
TN	thio-2-naphthol
UV-vis	ultraviolet-visble
4BPT	biphenyl-4-thiol
4MBT	4-methylbenzene thiol
4-NTB	2-nitro-5-thiobenzoate
4-NTB-MEG-OH	2-nitro-5-thiobenzoate-monoethylene glycol-hydroxy
4-NTB-TEG-COOH	2-nitro-5-thiobenzoate-triethylene glycol-carboxy
$n$	refractive index of the particle
$k$	Boltzman constant

## APPENDIX

---

$\mu\text{M}$	micromolar
$\mu\text{L}$	microliter
$\mu_{\text{ind}}$	induced dipole moment
$\nu_s$	frequency of the scattered light
$\lambda$	wavelength of the incident light
$\theta$	scattering angle
$\alpha$	polarizability
$\varepsilon$	molar extinction coefficient
$\varepsilon_m$	dielectric constant of NPs
$\varepsilon_s$	dielectric constant of the external medium
$\sigma_{\text{ads}}^R$	cross section of the adsorbed molecules
$\eta$	dynamic viscosity

**Publication list**

1. **Xin-Ping Wang**, B. Walkenfort, Matthias König, König Lisa, S. Kasimir-Bauer and S. Schlücker. Fast and Reproducible iSERS Microscopy of Single HER2-positive Breast Cancer Cells using Gold Nanostars as SERS Nanotags. *Faraday Discussion*, 2017, **205**, 377-386.
2. **Xin-Ping Wang**, Y. Y. Zhang, M. König, E. Papadopoulou, B. Walkenfort, S. Kasimir-Bauer, A. Bankfalvi and S. Schlücker, iSERS microscopy guided by wide field immunofluorescence: analysis of HER2 expression on normal and breast cancer FFPE tissue sections. *Analyst*, 2016, **141**, 5113-5119.
3. Yuying Zhang, **Xin-Ping Wang**, Sven Perner, Bankfalvi Agnes, Sebastian Schlücker, Effect of Antigen Retrieval Methods on Nonspecific Binding of Antibody–Metal Nanoparticle Conjugates on Formalin-Fixed Paraffin-Embedded Tissue. *Analytical Chemistry*, 2017, **90**, 760-768.

**Conference contribution**

- 03.2015 SERS round table, Duisburg, Germany (Participant)
- 03.2015 CENIDE, nanobiophotonics workshop, Essen, Germany (Participant)
- 10.2016 SERS round table, Poltersdorf, Germany (Participant)
- 04.2017 **iSERS microscopy guided by wide field immunofluorescence: analysis of HER2 expression on normal and breast cancer FFPR tissue sections**, JCF-Frühjahrssymposium, Mainz, Germany (Poster presentation)
- 08.2017 **Colocalization of the tumor markers HER2 and EGFR on the surface of breast cancer cells using rapid and reproducible two-colour iSERS microscopy**, Surface Enhanced Raman Scattering-SERS: Faraday Discussions, Glasgow, Scotland (Poster presentation)
- 12.2017 **Multi-colour iSERS microscopy of the HER2 distribution on single breast cancer cells by core-satellite SERS nanotags**, International conference on SERS, Xiamen, China (Best poster award)

## APPENDIX

---

The biography is not included in the online version for reasons of data protection.